STUDY OF THE NONLINEAR PROPAGATION OF FEMTOSECOND LASER PULSES

Thesis by

Martin Centurion

In Partial Fulfillment of the Requirements for the

Degree of

Doctor of Philosophy

CALIFORNIA INSTITUTE OF TECHNOLOGY

Pasadena, California

2005

(Defended May 11, 2005)

ACKNOWLEDGEMENTS

In my five years as a student at Caltech I have learned a great deal about both science and life. The journey has been as rewarding as challenging. I am very grateful to my advisor Demetri Psaltis for the many lessons he taught me about optics, research and life as a scientist. I will always be indebted to him for accepting me in his group (even though I did not know the first thing about optics), where I have greatly benefited from his creativity and vision. His trust and support have been instrumental in my accomplishments.

I would like to thank my mentor in the lab and good friend, Zhiwen Liu. It was a pleasure and a great opportunity to work with such a brilliant mind, who also had the patience to teach me. I am indebted to George Panotopoulos and Jose Mumbru for their guidance during my first years. George was and endless source of judicious advice and a dear friend. Jose was a reference on experimental skills and also provided a touch of humor when it was most needed. Hung-te Hsieh was my companion in the bumpy road to graduation, it was refreshing to share and office with him as he always brought plenty of excitement. Very special thanks to Lucinda Acosta for the administrative support, but more importantly for her moral support and friendship. She provided comfort in the times of frustration and helped me maintain a positive attitude.

I greatly benefited from collaborating with Ye Pu, a very good experimentalist and electronics wizard with whom I shared countless hours in the lab, Mankei Tsang, who helped me with the theoretical work, and Karsten Buse, who gave me excellent comments and advice during his visits from Germany. For their help and support, I would also like to thank Yayun Liu, David Erickson, Chris Moser, Greg Steckman, Greg Billock, Wenhai Liu, Manos Fitrakis, Todd Meyrath, Zhenyu Li, Hua Long, Jim Adleman, Eric Ostby, David McKeen and Bayiang Li. My friends, both here and at home have allowed me to keep a healthy balance between work and play.

Caltech was also the place where I met my beautiful wife Lucia, who became my muse and endless source of happiness. Her love is truly a blessing. My older brother has been a positive influence in my life, and I know he will always be there for me. All of my family has supported me in this adventure and surrounded me with their affection. Finally, I would like to dedicate this work to my father and my mother. Every success is a direct consequence of their influence in my life and their love.

ABSTRACT

This work presents a comprehensive study of the propagation of femtosecond pulses and the formation and evolution of spatial solitons. The first half (Chapters 2-3) is devoted to the implementation of a novel ultrafast holographic system to capture the nonlinear propagation of laser pulses with femtosecond resolution. Femtosecond pulses are used to record holograms of the ultrafast changes in the material properties. Amplitude and phase changes of the laser beam inside the medium are reconstructed numerically. The strength of the nonlinear material response and the density of free electrons can be recovered from the phase information in the hologram. A single hologram can be captured with fine spatial resolution, or a time-sequence of holograms can be captured in a single shot with reduced spatial resolution. We have observed dramatic differences in the light propagation depending on the material properties.

The second part of the thesis (Chapters 4-5) covers the formation and evolution of spatial solitons in a Kerr medium. We have measured the evolution of the beam profile as a function of pulse energy and propagation length. The optical beam breaks up into a pattern of connected lines (constellation) and self-focused spots (solitons). The solitons self-focus to a minimum diameter and release their excess energy through conical emission, which in turn overlaps with the background constellation and seeds the formation of new solitons. The solitons also show a collective self-organizing behavior caused by their mutual interactions. The evolution of 1-D arrays of solitons was captured using Femtosecond Time-resolved Optical Polarigraphy, a technique that measures the transient birefringence

induced by the pulses in the medium. When the array was generated in an unstable configuration, the solitons re-arranged themselves into an array with a (larger) more stable period. A transition to a chaotic state is observed when the input power is increased above a threshold level. A time-averaged pulse propagation equation was used to numerically solve for evolution of the beam. There was good agreement between the experimental results and the computer simulation.

TABLE OF CONTENTS

LIST OF FIGURES

LIST OF VIDEO CLIPS

Chapter 1

INTRODUCTION

1.1. MOTIVATION AND BACKGROUND

1.1.1. Research with femtosecond laser pulses

Understanding the propagation of femtosecond light pulses is of great value for both scientific and technological applications. The short pulse duration provides scientists with the possibility to explore physical phenomena with unprecedented time resolution; chemical reactions can be studied at the atomic level, and ultrafast changes in material properties can be measured. The high intensity levels achieved with ultrashort laser pulses create strong nonlinear light-matter interactions, which have led to new optical phenomena, such as the formation of spatio-temporal solitons [1,2] and the generation of coherent white light (white light laser [3]). Solitons are “solitary waves” that can propagate for a long distance with a constant shape and can interact with other solitons. The formation and propagation of solitons is of great interest for applications in optical communications and optical computing.

The advent of commercially available femtosecond lasers has triggered a wealth of new technologies, such as micromachining with femtosecond pulses, multiphoton imaging techniques and femtosecond LIDAR (Light detection and ranging). There have also been improvements to existing technologies, such as the use of femtosecond lasers in corrective eye surgery and Optical Coherence Tomography. There have also been many advances in the characterization and manipulation of pulses. Single-shot autocorrelators and spectrum analyzers can be replaced by frequency resolved optical gating (FROG [4]) devices that

capture a more complete description of the pulse properties. The pulses can be manipulated and transformed for specific applications using either grating based pulse-shapers, photonic crystal fibers, optical amplifiers, crystals for harmonic generation, etc. The widespread use of femtosecond lasers by researchers across different fields suggests even more applications are on the way. In many cases the interaction of the pulses with matter is very complex due to the strong nonlinear effects and is still not fully understood. I hope that the work presented here will shed some light on this very interesting problem.

1.1.2. Ultrafast cameras

The need to image fast phenomena has lead to many novel technologies and ever-faster imaging systems. Film-based cameras capture events in microseconds by using mechanical motion to direct the light to different parts of the film. Digital cameras with electro-optic switches can reach nanosecond frame rates. The speed of the electronics limits these cameras from achieving speeds much below a nanosecond [5]. Streak cameras can operate at picosecond or even sub-picosecond resolution, but provide only 1-dimensional information [6]. Holographic methods have also been implemented to observe fast events. The most common holographic technique for fast recording is double exposure interferometry, but is limited to only two frames. Light in flight recording [7] can capture the propagation of picosecond pulses through optical elements. However, this technique captures the scattering of the beam from a rough surface and cannot capture the beam profile inside the medium. More recently, a holographic camera was developed to capture events with nanosecond frame rates [8,9]. Nanosecond resolution can be used to observe fast phenomena like plasma formation and the evolution of shock waves. In order to observe the propagation of light pulses, however, we need to push the temporal resolution to sub-picosecond.

We have developed a holographic imaging system that captures nonlinear pulse propagation with 150-femtosecond time resolution and recovers amplitude and phase information. The propagation is captured using digital on-axis holography [10] and spatial multiplexing. The holograms are recorded on a CCD camera and reconstructed

numerically. On-axis holograms do not require separate signal and reference pulses; both the signal and reference are generated by a single probe pulse. The use of self-referenced holograms allowed us to capture a time-sequence of the event by spatially separating four holograms on a single frame of the CCD camera. The holographic system records either a single hologram with high spatial resolution (4 μm) or a time-sequence of four holograms (holographic movie) with reduced spatial resolution. Holography allows us to recover amplitude and phase information and to record a time-sequence of holograms in a single shot experiment. Nonlinear index changes in the material can be recovered from the phase information. Positive index changes are in general due to the Kerr nonlinearity, while negative index changes can appear if the intensity of the laser pulses reaches the ionization threshold. Plasma generation induces a negative index change that is proportional to the density of free electrons.

1.1.3. Visualization of the propagation of femtosecond pulses

Several methods have been implemented to visualize the propagation of femtosecond pulses. If temporal resolution is not required, one can measure a trace left in a material after a pulse has gone through and reconstruct the time-integrated spatial profile of the beam. For example, for pulse propagation through solids, if there is permanent damage in the material the beam profile can be inferred from the damage tracks. In the case of fluids, the trace can be visualized by dissolving a fluorescent dye in the material and capturing a side view of the fluorescence [11] or by imaging the light emission from plasma generated by the pulse.

Pump-probe experiments can capture the time evolution if the event is repeatable. Care must be taken to ensure the experimental conditions do not change during the experiment. A pump pulse is used to generate the ultrafast event, and a probe with a variable time delay is used to observe it as a function of time. The time evolution of the event can be recovered by combining multiple experiments with different time delays. A probe pulse can monitor the reflectivity or transmission of a sample directly. An alternative to holography for measuring the nonlinear index change due to the Kerr effect is Femtosecond Time-resolved

Optical Polarigrahpy (FTOP) [12]. This technique monitors changes in the polarization of the probe that result from birefringence induced in medium. We have used this technique to study the behavior of spatial solitons in 1-D arrays (Chapter 5, [13]). The advantage of FTOP is that it has a high sensitivity, while the drawback is that it can only capture birefringence and not isotropic index changes such as the plasma index change.

The pulse propagation can also be studied by directly measuring the beam profile as a function of energy and propagation length. Increasing the pulse energy causes the beam to self-focus and break up in a shorter distance. Varying the energy and propagation distance allowed us to do a comprehensive study of pulse propagation through a nonlinear liquid (Chapter 4, [14]). The propagation distance was adjusted by changing the height of the liquid in-situ. Combining the results obtained with the holographic system, the propagation as a function of energy and length, and the results with FTOP, we were able to investigate the process of beam breakup, the formation of spatial solitons and their interactions, and the collective behavior of the solitons that results from interactions.

1.2. LASER SYSTEM AND DIAGNOSTICS

In our experiments we have used femtosecond pulses from a Titanium:Sapphire laser amplifier system (Fig. 1.1). The amplifier requires a seed laser, which provides low energy femtosecond pulses, and a pump laser. The seed laser is a Ti:Sapphire femtosecond laser (Coherent Mira 900), which provides 100-200 femtosecond pulses at a wavelength of 800 nm (tunable from 700-900 nm) with a repetition rate of 76 MHz and average power up to 1 W. The laser uses a passive Kerr-lens modelocking system and intra-cavity dispersion compensation prisms. The Mira is pumped by a CW multi-line argon laser (Coherent Innova 300C) with a power of 8 W. The seed pulses are fed into a Spectra Physics TSA regenerative amplifier. The TSA is pumped by a frequency doubled Nd:Yag laser (Spectra Physics Quanta Ray Lab 150), which generates 6-nanosecond pulses with a repetition rate of 10 Hz, and maximum energy of 300 mJ at a wavelength of 532 nm. The seed pulses are stretched in the TSA using a grating pair and inserted into a cavity with a Ti:Sapphire

crystal. Pump pulses with 50-mJ energy are synchronized with the seed pulses and inserted in the cavity. After multiple passes through the Ti:Sapphire crystal the femtosecond pulses are switched out of the cavity and recompressed with the grating pair. The pulses are switched in and out of the cavity using Pockels cells. The output pulses have a maximum energy of 2 mJ, 150-femtosecond pulse duration, wavelength of 800 nm and repetition rate of 10 Hz.

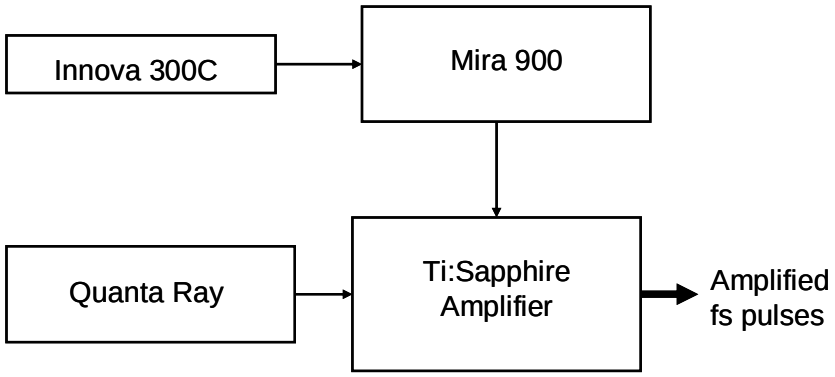

Figure 1.1. Schematic diagram of the laser system. A seed femtosecond laser (Mira 900) and a pump nanosecond laser (Quanta Ray) are used to feed the amplifier (TSA). The Mira is pumped by a CW argon ion laser (Innova 300C).

A frequency-resolved optical gating (FROG) device is used to characterize the output pulses from the Mira and the TSA. The technique can measure the intensity and phase of the pulses as a function of time. The device is a Grenouille from Swamp Optics, which can measure pulses from 30-300 femtoseconds. The FROG traces are processed in real time using the VideoFrog software package from Southwest Science. Figure 1.2 shows a screen capture of the trace and the reconstruction of typical output pulses from the Mira (seed laser). After the amplification there is some distortion of the pulses. Figure 1.3 shows a screen capture of the output pulses from the TSA. The amplified pulses are measured in a single-shot, while the measurement of the seed pulses is averaged over many pulses.

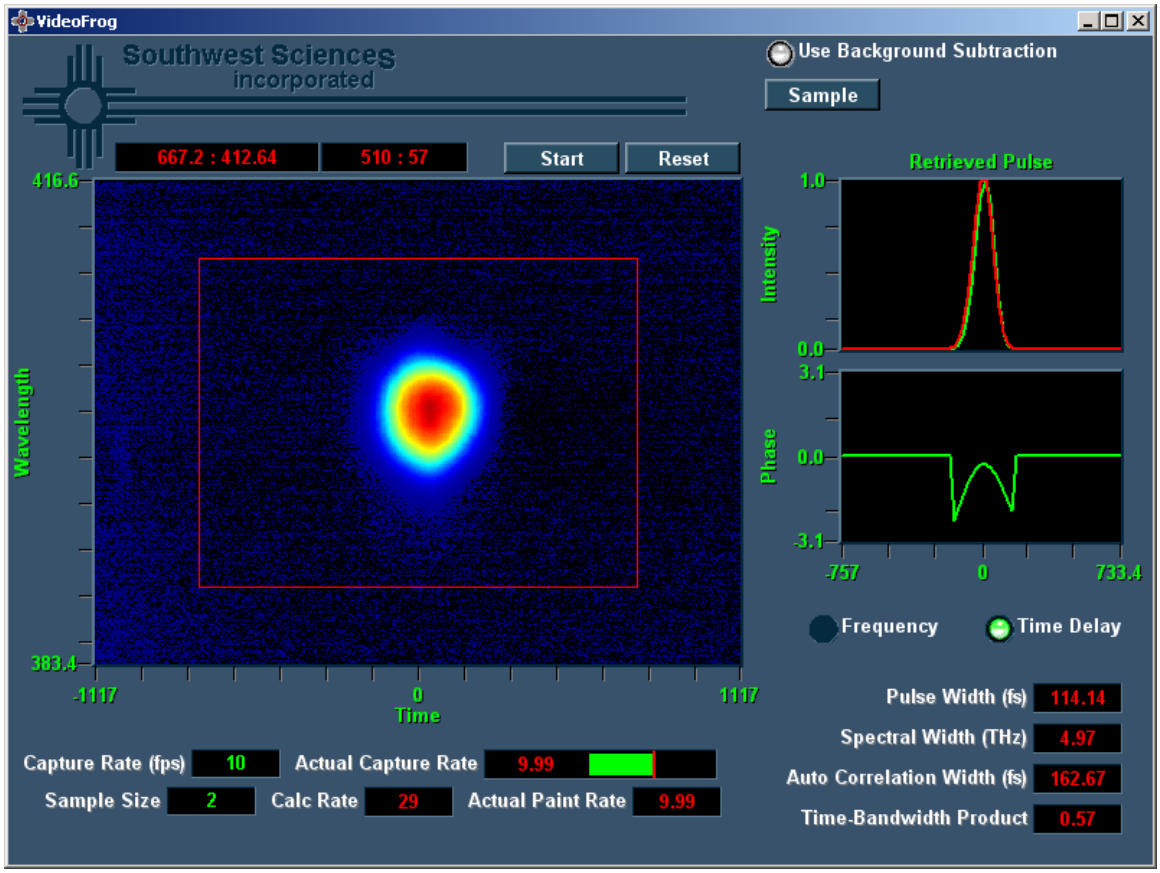

Figure 1.2. Screen capture of the FROG trace and reconstruction of pulses from the seed laser (Mira).

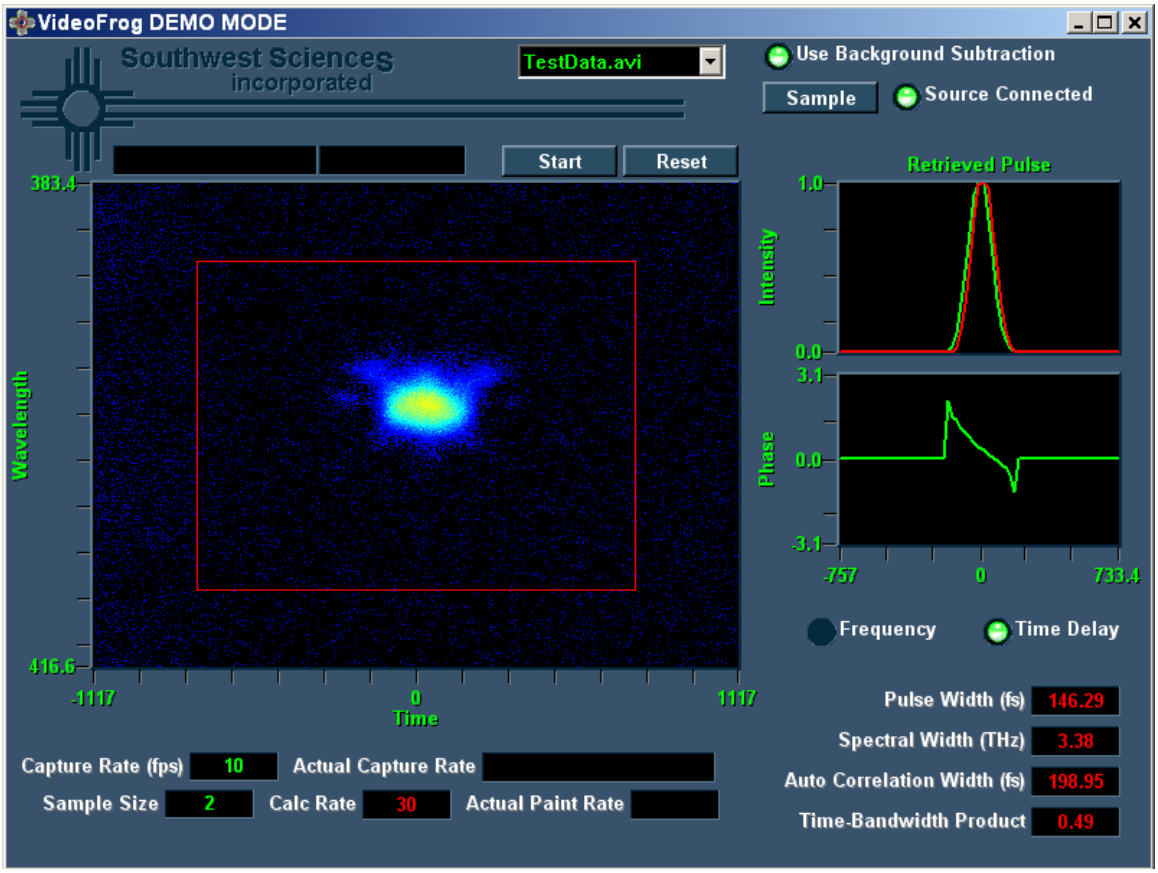

Figure 1.3. Screen capture of the FROG trace and reconstruction of pulses from the laser amplifier (TSA).

1.3. NUMERICAL SIMULATIONS

We have used computer simulations to calculate the pulse propagation in a self-focusing material. The numerical results complement the experimental results and provide insight into the mechanisms responsible for the measured effects. The propagation of ultrashort pulses is modeled using the nonlinear Schrodinger equation (NLSE). The equation is derived from Maxwell's equations by including the nonlinear polarization terms and applying some approximations (see Appendix A for the derivation). The NLSE describes the propagation of the complex envelope of the electric field. For a pulse propagating in the *z*-direction:

$$\frac{\partial A}{\partial z} = -i\frac{k_2}{2}\frac{\partial^2 A}{\partial u^2} + \frac{i}{2k_0}\nabla_T^2 A + i\frac{k_0}{n_0}\left(n_2|A|^2 + n_4|A|^4\right)A \tag{1.1}$$

where $\nabla_T^2 = \frac{\partial^2}{\partial x^2} + \frac{\partial^2}{\partial y^2}$ is the diffraction operator and $u = t - \frac{z}{v_g}$ is the time in a reference frame moving along with the pulse at the group velocity v_g. A is the complex envelope of the electric field, $k_0 = n_0\frac{\omega_0}{c}$, n_0 is the linear part of the refractive index of the medium, ω_0 is the carrier frequency of the pulse, c is the speed of light, k_2 is the coefficient for group velocity dispersion and n_2 and n_4 are the coefficients for third and fifth order nonlinearities, respectively. The intensity of the light is proportional to $|A|^2$.

The equation above describes how the field evolves with propagation distance. The first term on the right hand side accounts for group velocity dispersion, the second accounts for diffraction and the last term accounts for third and fifth order optical nonlinearities. It is computationally very expensive to numerically solve the equation in three spatial dimensions and time, so we have also used a time-averaged NLSE, where A_s is a time averaged field that depends only on the spatial coordinates:

$$\frac{\partial A_s}{\partial z} = \frac{i}{2k_0}\nabla_T^2 A_s + ik_0\left(n_2|A_s|^2 + n_4|A_s|^4\right)A_s \tag{1.2}$$

The NLSE is solved numerically using the Split-step Fourier method [15]. The propagation is solved in steps by splitting each step into the linear and nonlinear parts of the propagation. The linear part (diffraction) is solved by Fourier-transforming the equation to the frequency domain. The equation is then Fourier-transformed back to the time domain where the nonlinear step is calculated. The step size and number of pixels required for the simulation depends on the strength of the nonlinearity and the intensity of the light. The effect of the nonlinearities is that the beam will see index changes proportional to the intensity (n_2) and to the square of the intensity (n_4). If n_2 is positive, and n_4 negative, the interplay between diffraction and nonlinearities induces the formation of spatial solitons, or light filaments. The filaments can propagate for a distance much greater than the diffraction

length with a constant diameter. In the simulations we have observed the beam to break up into multiple filaments, which then interact with their neighbors. The experimental results were compared with the numerical results and found to be in good agreement.

1.4. THESIS OUTLINE

The first half of this thesis describes the implementation of a novel holographic system to capture the propagation of femtosecond pulses. The holographic camera can reconstruct index and absorption changes inside the material with very fine spatial and temporal resolution. Chapter 2 is a theoretical analysis of recording and reconstructing holograms with femtosecond pulses. The chapter describes the origin of the nonlinear index changes, i.e., the Kerr effect and plasma formation. The use of on-axis holograms results in the appearance of a twin image, which introduces artifacts in the reconstructed field. We developed an algorithm to numerically remove the distortion due to the twin image. There are also issues that are unique to holography with ultrashort pulses, such as the geometry of the overlap of pump and probe pulses and the coupling between temporal and spatial resolution. In Chapter 3 we present results on pulse propagation through different materials captured with the holographic system. Dramatic differences were observed in the propagation of pulses in air, water, carbon disulfide and lithium niobate.

The second half focuses on the formation and interaction of spatial solitons in a self-focusing medium. In Chapter 4 we have investigated the mechanisms involved in the formation of solitons by observing the beam profile as a function of energy and propagation distance. We have discovered that the emission of conical waves plays a fundamental role in the formation of spatial solitons. Chapter 5 presents a study of the collective behavior of spatial solitons. We have observed the emergence of order as solitons appear on the beam profile followed by a transition to a chaotic state when the density of solitons becomes too high. When the solitons are generated in an unstable configuration they self-organize into an array with a larger period. The results in Chapters 4 and 5 are complemented by numerical simulations of the pulse propagation.

REFERENCES

[1] J. P. Gordon, Optics Letters **8**, 596 (1983).

[2] G. I. Stegeman and M. Segev, Science **286**, 1518 (1999).

[3] R. L. Fork, C. V. Shank, C. Hirlimann, et al., Optics Letters **8**, 1 (1983).

[4] D. J. Kane and R. Trebino, IEEE Journal of Quantum Electronics **29**, 571 (1993).

[5] Cordin Scientific Imaging, [http://www.cordin.com].

[6] Hamamatsu, [http://www.hamamatsu.com].

[7] N. Abramson, Applied Optics **22**, 215 (1983).

[8] Z. W. Liu, M. Centurion, G. Panotopoulos, et al., Optics Letters **27**, 22 (2002).

[9] Z. W. Liu, G. J. Steckman, and D. Psaltis, Applied Physics Letters **80**, 731 (2002).

[10] D. Gabor, Nature **161**, 777 (1948).

[11] H. Schroeder and S. L. Chin, Optics Communications **234**, 399 (2004).

[12] M. Fujimoto, S. Aoshima, M. Hosoda, et al., Optics Letters **24**, 850 (1999).

[13] M. Centurion, Y. Pu, and D. Psaltis, Physical Review Letters (2005).

[14] M. Centurion, Y. Pu, M. Tsang, et al., Physical Review A (2005).

[15] G. P. Agrawal, *Nonlinear fiber optics* (Academic Press, San Diego, 1995).

Chapter 2

ANALYSIS OF ON-AXIS HOLOGRAPHY WITH FEMTOSECOND PULSES

2.1 CAPTURE OF NONLINEAR PULSE PROPAGATION WITH PULSED-HOLOGRAPHY

Very high intensity levels can be achieved with femtosecond pulses due to their short time duration. Ultrashort pulses can significantly change the properties of the medium through which they propagate, which in turn alters the pulse itself. Much can be learned about the propagation of pulses from the changes in the material properties. The time scale of the changes ranges from instantaneous to permanent. Ultrafast nonlinear index changes can be as fast as a femtosecond or last for several picoseconds. Plasma generated through ionization of the material has a lifetime on the order of nanoseconds, while index changes due to heating can last for milliseconds. There can also be a permanent effect on the material, such as in the case of laser ablation or permanent index changes due to melting. Pulsed holography provides an ideal way to observe these index changes. The index changes can be reconstructed from the phase information in the hologram, while the duration of the pulse provides time resolution to focus on the time window of interest. We have used an on-axis [1] holographic setup, in which a femtosecond probe pulse captures the changes in the material properties. The holographic camera records either a single hologram with high spatial resolution (4μm) or a time-sequence of four holograms (holographic movie) with reduced spatial resolution. The main advantage of using on-axis holography is that there is no need for reference pulses, as both the signal and reference are generated from a single probe pulse. The holograms are recorded on a CCD camera and reconstructed numerically [2-4]. Multiple holograms can be captured on a single frame of

the CCD camera by spatially separating them (spatial multiplexing). With the multiple frame capture, the time evolution of the pulse propagation is captured in a single-shot experiment.

In this chapter we briefly discuss the sources of nonlinear index changes that can be observed with femtosecond pulses. The Kerr effect (third order optical nonlinearity) generates a positive index change with a femtosecond to picosecond duration. Ionization of the medium (plasma formation) results in a negative index change with a lifetime on the order of nanoseconds. The changes in the material properties are captured by a weak probe pulse, which temporally and spatially overlaps with a strong pump pulse. The short duration of the pulses plays a major role in the overlap and interaction of the pulses. The interaction can be analyzed using some simple geometrical arguments. The main limitation of on-axis holography is the appearance of twin images when the hologram is reconstructed. The reconstruction is distorted by the appearance of a defocused virtual image along with the real image. We will discuss how this affects the accuracy of our measurements and present an iterative algorithm to remove the effect of the twin image. Finally we discuss the coupling between spatial and temporal resolution limits of on-axis holograms. The following chapter describes the holographic camera in detail and the results for pulse propagation through different materials.

2.2 INDUCED NONLINEAR INDEX CHANGES

2.2.1. Kerr effect

The advantage of the holographic recording is that it captures the index changes due to both the Kerr nonlinearty (in general positive) and plasma generation (negative index change), along with changes in the amount of light transmitted by the material. When the intensity of the incident light is very high, the nonlinear contributions to the polarization of the medium must be taken into account. If the electric due to the incident light is small compared to the atomic electric field, the polarization can be expanded in a power series:

$$P_i = \chi_{ij}^{(1)} E_j + \chi_{ijk}^{(2)} E_j E_k + \chi_{ijkm}^{(3)} E_j E_k E_m + \ldots, \tag{2.1}$$

where $\chi^{(n)}$ is a tensor of order $(n+1)$ that represents the n^{th} order response of the material and P_i and E_i are the i^{th} vector components of the polarization and the electric field, respectively. The three terms on the right hand side are the linear response of the material, the second order nonlinear response and the third order nonlinearity, respectively. The nonlinear terms can generate a polarization at frequencies different from that of the incident light, for example, the second order term is responsible for second harmonic generation. It is known that for isotropic materials the second order response vanishes [5]. The term responsible for a self-induced nonlinear index change in the material is the third order response:

$$P^{NL} = \chi^{(3)} |E|^2 E\,. \tag{2.2}$$

This is commonly referred to as the Kerr effect. The response of the material is proportional to the square of the electric field. This can also be written as an index of refraction with a linear contribution, which is constant, and a nonlinear contribution that depends on the intensity of the light [6]:

$$n = n_0 + n_2 I\,, \tag{2.3}$$

where n_0 is the refractive index of the material, n_2 is the Kerr coefficient of the material and I is the light intensity. The Kerr coefficient can be positive or negative, and depends on the duration of the incident light and the frequency. For CW light or long laser pulses (microseconds) the thermal response of the material dominates resulting in a negative n_2. The heating of the material causes a density change and a negative index change. If the material is studied with ultra-short pulses, on the order of tens of picoseconds or shorter, the excitation is too short for thermal effects to play a role. In this case the main contributions are the instantaneous electronic response of the material (with a time constant of the order of a femtosecond) and the molecular response (with time constants on the order of picoseconds). The instantaneous response corresponds to the electronic response in the atom or molecule to the incident electric field, while the molecular response corresponds to

excitation of the molecules (vibration, rotation, etc.). The ultra-fast Kerr effect is positive for most material, although some exceptions have been found in some special polymers [7]. For any given material, then, the strength and sign of the Kerr effect that is observed will depend on the duration of the incident laser pulses. For excitation with 150-femtosecond pulses, it is possible to observe both electronic and molecular responses, although the electronic response dominates in general.

A positive Kerr response means that a non-uniform laser beam will experience self-focusing. For example, a beam with a Gaussian spatial profile will have a higher intensity at the center of the beam. There will be an index change in the material that is higher near the center of the beam and vanishes at the edge of the beam. This index change will act as a lens and focus the beam. A laser pulse will experience self-focusing if its power is higher than a critical value, defined as [5]:

$$P_{cr} = \frac{\pi(0.61)^2 \lambda^2}{8 n_0 n_2}, \tag{2.4}$$

where λ is the laser wavelength. At the critical power, the nonlinearity exactly cancels the effect of diffraction; the beam becomes self-trapped and propagates with a constant diameter. This is, however, an unstable equilibrium. If the power is initially below the critical value the beam will diffract, and if the power is above the critical value the beam will continue to self-focus until another mechanism acts to balance the self focusing. This balancing can lead to the formation of optical spatial solitons and will be discussed in detail in the following chapters. When the power of the pulses is much greater than the critical power ($P > 100\ P_{cr}$) the beam will break up into multiple filaments, each one carrying approximately the critical power. Any initial modulation (noise) in the input beam will be amplified by the self focusing process, eventually resulting in the beam breaking up into smaller beams, or filaments (Fig. 2.1).

2.2.2. Index change due to plasma generation

If the intensity of the filaments exceeds the breakdown threshold of the material, free electrons are generated. For excitation with ultrashort (femtosecond) pulses, the dominant mechanism for plasma formation is multi-photon absorption. A single electron will absorb multiple photons at the same time, and the medium becomes ionized. The plasma generated induces a negative index change, which can balance the positive index change of the Kerr effect. The plasma index change is given by:

$$\Delta n = \sqrt{1 - \frac{\omega_p^2}{\omega}} - 1 \approx \frac{-\omega_p^2}{2\omega^2}, \tag{2.5}$$

where ω = 2.36 x 10^{15} s^{-1} is the angular frequency of the laser and ω_p is the plasma frequency:

$$\omega_p^2 = \frac{Ne^2}{\varepsilon_0 m}, \tag{2.6}$$

where N is the electron density, e = 1.6 x 10^{-19} C is the charge of the electron, m = 9.1 x 10^{-31} kg is the mass of the electron and ε_0 = 8.85 x 10^{-12} $C^2s^2m^{-3}kg^{-1}$ is the permittivity of free space. The plasma density can thus be calculated if the index change is measured. The plasma index change can stabilize the self-focusing due to the Kerr effect [8, 9]. As the filaments continue to focus and the intensity increases, the plasma density and negative index change also increase. Eventually the negative index change becomes strong enough so as to defocus the light, at which point the intensity and plasma density decrease, leading to a new cycle of self focusing. Some energy is lost through the ionization process, so eventually the cycle stops when the power in the beam is no longer above the critical power. In the absence of plasma, a higher nonlinearity (fifth order nonlinearity) can act to balance the self-focusing through a saturation of the index change [10]. Which effect becomes dominant depends on the material properties and the intensity and duration of the pulses.

2.3 INTERACTION AND OVERLAP OF FEMTOSECOND PULSES

The holographic recording technique uses a strong pump pulse that interacts with the material and a weak probe pulse that captures the changes in the material. Any instantaneous changes in the material properties will be captured only when the pump and probe overlap temporally and spatially. Long-lasting changes in the material, lasting longer than a few hundred femtoseconds, can also be observed after the pump pulse has traversed the material. The instantaneous changes will reveal a snapshot of the pump pulse traversing the material, while the long lasting changes will appear as a trail behind the moving pulse. The trail can be due to the delayed Kerr response, with a time constant of picoseconds, or a plasma trail that lasts for a longer time (nanoseconds). The probe pulses, which propagate at an angle relative to the pump, are captured using a CCD camera (Fig. 2.1).

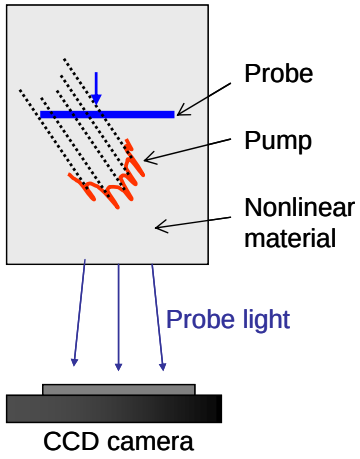

Figure 2.1. Sketch of holographic capture. There are an instantaneous component of the index change and a trail behind the pulse that contribute to the signal on the probe pulse. The probe light is captured on a CCD camera.

The angle difference between pump and probe is in the horizontal direction, as observed on the camera. Smaller angles lead to longer interaction lengths and increased signal strength as the phase changes in the probe accumulate over a longer distance. If the pump pulse

leaves a trail in the material that lasts longer than the time window of the experiment (a few picoseconds), then a probe arriving after the pump will capture the entire trail. An instantaneous effect, however, can only be captured when the pulses overlap temporally and spatially. For two ultrashort pulses propagating at an angle, the overlap region will be a thin strip at the midline between the two pulses (Fig. 2.2). The width of the overlap strip depends on the duration of the pulses and the angle between them:

$$w_o = \frac{c\tau}{n\sin(\theta/2)} A_t = \frac{w_t}{\sin(\theta/2)} A_t , \tag{2.7}$$

where τ is the duration of the pulses, θ is the angle between the two beams inside the medium, c is the speed of light, n is the index of refraction, A_t is a numerical factor that depends on the shape of the temporal envelope of the pulses and w_t is the length of the pulses in space. The temporal profile of the pulses is approximately Gaussian, in which case $A_t = 0.707$.

The total length of the overlap region is

$$L_o = \frac{D}{\sin(\theta/2)} A_s , \tag{2.8}$$

where D is the diameter of the smaller (pump) beam, and A_s is a numerical factor that depends on the shape of the spatial beam profile. As observed on the CCD camera, the signal width in the horizontal direction will be a projection of both the width and the length of the overlap region. The size of the overlap region projected on the CCD camera can be approximated as:

$$L_{CCD} \approx DA_s + \frac{w_t}{\tan(\theta/2)} A_t . \tag{2.9}$$

The first term dominates for large beam diameter, while the second term becomes important for small beam diameters and small angles. The signal width on the CCD along the vertical direction will be equal to the pump beam diameter D.

If the time delay of the probe is changed the pulses will overlap at a different position, resulting in the motion of the pump pulse on the camera. The velocity of the pulse inside the medium can be calculated from the apparent velocity of the pulse on the camera:

$$v = \frac{\Delta x}{\Delta t}\tan(\theta/2), \tag{2.10}$$

where Δx is the change in position of the pump in the camera, and Δt is the time delay. For a 90-degree setup there is a one-to-one correspondence between the apparent and real speeds.

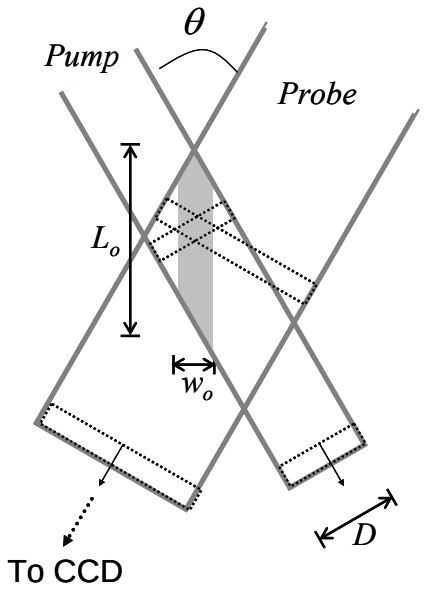

Figure 2.2. Overlap region for two ultrashort pulses. The overlap region is a thin strip along the center line between the two pulses. The width of the strip is determined by the duration of the pulses, while the length of the strip is determined by the beam size.

2.4. DIGITAL RECORDING AND RECONSTRUCTION OF ON-AXIS HOLOGRAMS

2.4.1. On-axis holograms and the twin image problem

The use of on-axis (self-referenced) holograms allows us to record holograms without having to separately generate a sequence of signal and reference pulses. The object is illuminated by a plane wave and the light scattered by the object interferes with the transmitted light (Fig. 2.3a). The intensity of the light field at the recording plane is captured with a CCD camera, which allows us to reconstruct the hologram numerically on the computer. Accurate holographic reconstructions can be obtained provided the amount of light scattered by the object is small compared to the transmitted light.

The object is illuminated by a plane wave, which we normalize to be of unit amplitude. The complex light field at the object plane is:

$$F_O(x,y) = 1 + O(x,y)\,. \tag{2.11}$$

O(x,y) is the complex disturbance of the light field induced by the object. We assume that the area covered by the object is small compared to the area of the illuminating beam (or the area of the camera, whichever is smallest). This ensures that at the detector the transmitted light field will be much stronger than the object field.

The field at the hologram plane, a distance *z* from the object plane, is obtained by convolving the object field with the Fresnel convolution kernel [11]:

$$F_H(x,y) = \left[1 + O(x,y)\right] \otimes h_z(x,y)\,, \tag{2.12}$$

where $h_z(x,y)$ is the Fresnel convolution kernel:

$$h_z(x,y) = \frac{Exp(jkz)}{j\lambda z} Exp\left[\frac{jk}{2z}\left(x^2 + y^2\right)\right]. \tag{2.13}$$

The convolution can be calculated on the computer using Fast Fourier Transforms. If $F_H(x,y)$ is known, the object field can be reconstructed exactly applying the Fresnel convolution kernel in the opposite direction (-z). However, the hologram captures only the intensity of the light at the hologram plane:

$$H(x,y) = \left|F_H(x,y)\right|^2 = \left|\left[1 + O(x,y)\right] \otimes h_z(x,y)\right|^2 . \tag{2.14}$$

If we now try to reconstruct the object field from the intensity measurement using the Fresnel convolution kernel, the reconstructed field contains the desired object field plus an extra term:

$$F_R(x,y) = H(x,y) \otimes h_{-z}(x,y) = 1 + O(x,y) + O^*(x,y) \otimes h_{-2z}(x,y) . \tag{2.15}$$

The first term on the right-hand side represents the transmitted light (plane wave). The second term is the object field and the third term is a twin image, which is the conjugate of the object field diffracted by a distance of -2z. A term of order square of the object field was neglected. The holographic reconstruction contains the desired amplitude and phase information, but is distorted by the presence of the twin image (Fig. 2.3b) [1, 12]. For small objects, the distortion will in most cases appear in the form of fringes around the object. The twin image problem is caused by the loss of the phase information when the hologram is recorded (the camera captures only the intensity of the light field). The twin image is present in both optically and digitally reconstructed on-axis holograms. The problem is less severe for small objects and large recording distance z, in which case the twin image will appear as background noise around the true object.

The digital holograms also contain 3-D information about the object. The hologram can be numerically re-focused at different planes by changing the distance z in the Fresnel kernel (equation 2.13), bringing different object features to focus and revealing three-dimensional structure. We will show an example of this in the next chapter.

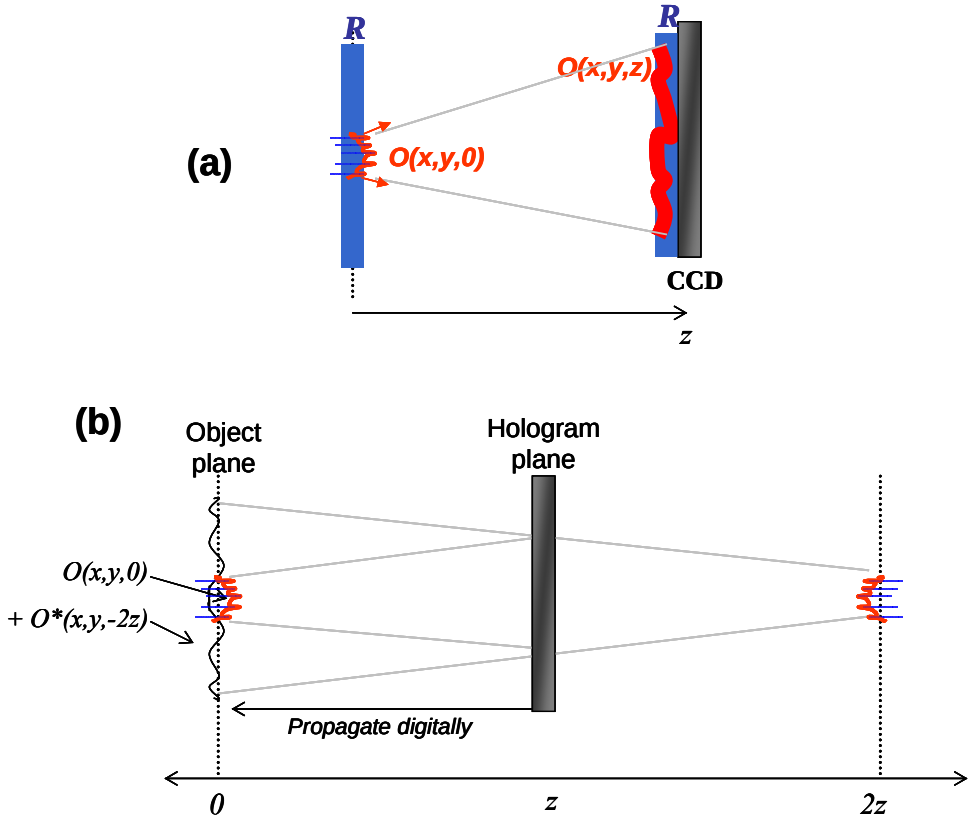

Figure 2.3. Recording and reconstruction of on-axis holograms. (a) Recording geometry. (b) Both a real and a virtual image appear in the reconstruction.

2.4.2. Numerical reconstruction for small objects

In our experimental setup for single frame capture, the distortion due to the twin image does not significantly affect accuracy of the reconstruction. The pump pulse breaks up into small filaments with a diameter of 4 µm to 15 µm and lengths of approximately 1 mm. After a magnification factor of 12 a filament covers only a small fraction of the recording area (the CCD sensor area is 14.8 mm x 10.2 mm).

We have performed numerical simulations to calculate the distortion induced by the presence of the twin image. The diffraction pattern due to a filament with a diameter of 8

μm and a length of 500 μm was calculated for a recording distance of 25 cm. The accumulated phase change for a beam that traverses the filament is 1 rad, caused by an index change in the material. The magnification, pixel size and number of pixels are the same as in the experimental apparatus (M = 12, 2184 x 1472 pixels, 6.8 μm pixel size). The phase change and filament size are comparable to those observed experimentally for plasma filaments generated in air, as described in the following sections (with the difference that the plasma generates a negative index change). The light propagation from the object plane to the recording plane is calculated numerically using the Fresnel convolution Kernel (equations 2.12-13). The intensity pattern at the recording plane is used to calculate the reconstruction at the object plane. Figure 2.4a shows a cross section of the phase of the input and reconstructed light field. The reconstruction agrees very well with the simulated filament at the position of the filament. The maximum phase change and width of the input and reconstructed filaments differs by less than 5%. The inset shows a close-up of the filament region. Outside the filament area the reconstruction shows the fringes characteristic of the twin image. In the experimental images two filaments may appear in close proximity, so we also simulated two filaments with 8 μm diameter separated by 16 μm (Fig. 2.4b). In this case there was also good agreement between the input and the reconstruction, with the characteristic fringes outside of the object area. The error, however, increases rapidly with object size. In the next section we present an iterative technique that can reduce the distortion when the object occupies a larger fraction of the hologram area.

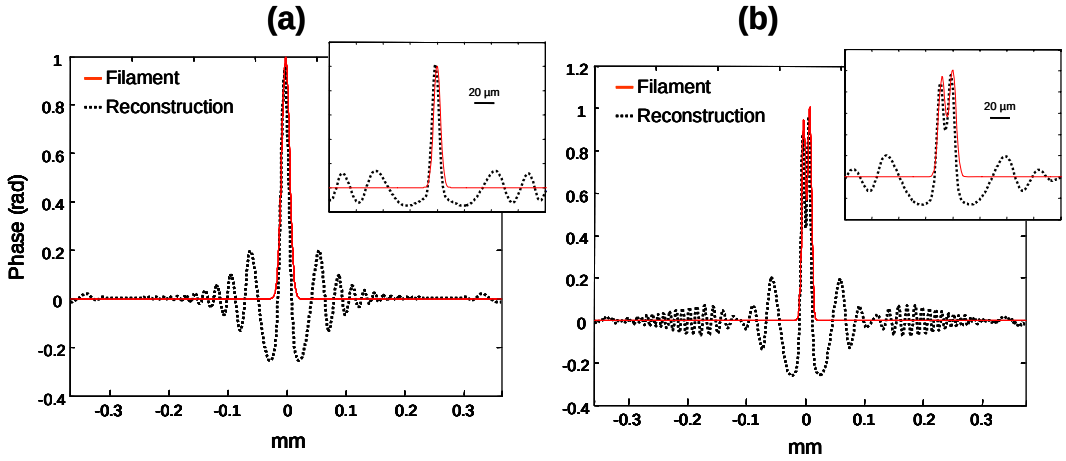

Figure 2.4. Simulation of phase reconstruction from on-axis holograms. a) Cross section of simulated (red, solid line) and reconstructed (black, dotted line) phase filament with 8 µm diameter. b) Simulation and reconstruction of double filament. The insets shows a close-up of the filament and reconstruction. In both cases the reconstruction is accurate at the position of the filament.

2.5. REMOVAL OF THE TWIN IMAGE

As the size of the object relative to the recording area increases, the distortion due to the twin image becomes more severe. In the case when multiple holograms are multiplexed on a single frame of the CCD camera, the distortion can be significant. The twin image can be removed if the phase of the light at the recording plane is recovered. Digital holograms have the advantage that this distortion can be corrected numerically. A number of algorithms have been implemented to recover the phase of the hologram. One method uses a double exposure [13] to calculate the phase from two intensity measurements, while the most common method is to use an iterative algorithm [12, 14, 15]. Iterative techniques in general assume that the object is real, that is, the object affects only the amplitude of the light field. The real part of the initial reconstruction is used as the starting point, and the

reconstruction is iterated applying the constraint that the object reconstruction be real at each step. This method works well for image reconstruction; however, it does not allow one to recover both amplitude and phase.

We have developed a variation of the iterative technique that allows us to reconstruct both amplitude and phase for objects that are small compared to the area of the hologram. The unknown that we need to recover in order to remove the twin image is the phase of the field at the hologram plane. We know that the phase and amplitude of the object reconstruction must be constant outside of the object area, given that it was originally illuminated with a plane wave. The light field that we want to recover is given by equation 2.11. After the initial reconstruction (equation 2.15) it is in general possible to estimate the size and position of the object, even though there is distortion from the presence of the twin image. The object reconstruction will be localized, while the twin image will be spread out due to diffraction. The initial reconstruction F_R is used as the starting point of the iterative reconstruction. A new field is generated by applying the constraint of a plane wave illumination. Specifically, the constraint is applied by multiplying the reconstruction with an aperture function that is unity in the estimated object area and zero outside. The zeroed area is replaced by a uniform field with the mean amplitude and phase of the original field. The initial guess for the iterative algorithm is:

$$\begin{aligned} F_{G1}(x,y) &= A(x,y)F_R(x,y) + \big(1 - A(x,y)\big) \\ &= 1 + A(x,y)O(x,y) + A(x,y)\Big(O^*(x,y) \otimes h_{-2z}(x,y)\Big), \end{aligned} \tag{2.16}$$

where *A(x,y)* is unity inside the estimated object area and zero outside. If the function *A(x,y)* is chosen properly, it will only affect the twin image:

$$F_{G1}(x,y) = 1 + O(x,y) + A(x,y)\Big(O^*(x,y) \otimes h_{-2z}(x,y)\Big). \tag{2.17}$$

The light field at the hologram plane is calculated by numerically propagating the guessed object field F_{G1} by a distance z:

$$\begin{aligned} F_{H1}(x,y) &= F_{G1}(x,y) \otimes h_z(x,y) \\ &= \big[1 + O(x,y)\big] \otimes h_z(x,y) + \Big[A(x,y)\Big(O^*(x,y) \otimes h_{-2z}(x,y)\Big)\Big] \otimes h_z(x,y), \end{aligned} \tag{2.18}$$

where the first term on the second line is what we want to recover, while the second term is due to the twin image. The effect of the aperture function *A(x,y)* is to reduce the strength of the contribution from the twin image at the recording plane. If *A(x,y)* is set to one everywhere, the sum of the contributions from the real and the virtual images results in a real field, and no phase information is recovered. For large recording distance *z*, the aperture function is effectively transmitting only the low frequency components of the twin image, thus reducing the phase modulation due to the twin image at the hologram plane. A corrected field is generated by combining the measured intensity with the reconstructed phase:

$$\overline{F}_{H1}(x,y) = \sqrt{H(x,y)}\exp\left[i * \text{Phase}\left(F_{H1}(x,y)\right)\right], \tag{2.19}$$

where *H(x,y)* is the intensity distribution of the hologram measured on the CCD camera, and Phase($F_{H1}(x,y)$) is the phase of F_{H1}. The corrected field is used to generate a new object reconstruction and start a new cycle:

$$F_{R2}(x,y) = \overline{F}_{H1}(x,y) \otimes h_{-z}(x,y) = \left[1 + O(x,y)\right] + T_1(x,y) \ , \tag{2.20}$$

where $T_1(x,y)$ is the distortion of the field due to the twin image that is left after 1 iteration. A second guess is generated using the same procedure as before:

$$F_{G2}(x,y) = A(x,y)F_{R2}(x,y) + \left(1 - A(x,y)\right) = \left[1 + O(x,y)\right] + A(x,y)T_1(x,y) \, . \tag{2.21}$$

The new guess is used for a new iteration. The function $T_n(x,y)$ will in general get weaker after each iteration. The process continues until the reconstruction no longer changes. The number of iterations depends on the amount of distortion in the initial reconstruction. A stable reconstruction is generally achieved after 4-10 iterations. The performance of the algorithm can be monitored qualitatively by the decrease in the characteristic fringes around the object with each iteration or quantitatively using numerical simulations. It is important to choose the correct size for the aperture function. If the aperture is too small it will distort the reconstruction, as the object will fill the aperture area. If the aperture size is too large then it might not have a strong enough effect on the twin image. The most

efficient method to choose the aperture was to use the phase of the reconstruction to determine the size of the object, and to fine tune the aperture by looking at the results. We have seen that the shape of the aperture is not very critical unless the object is very asymmetric. A simple rectangular aperture has given good results in most cases.

We have numerically tested the algorithm and seen a significant improvement in the accuracy of the reconstructions. The simulation is run for a detector size of 512 pixels by 512 pixels (6.8 μm pixel size), about one fourth of the size of our CCD camera, and no magnification. We simulate an object field with Gaussian shape (width = 0.11 mm, length = 0.44 mm) with a positive phase change and absorption. The peak phase change is 1 radian and the minimum amplitude transmittance is 70 %. These values are similar to those observed in several of the experiments. Figure 2.5 shows the amplitude of (a) the simulated object field, (b) the initial reconstruction and (c) the initial guess used for the iterative technique, while (d-f) shows the phase of the object, the reconstruction and the initial guess, respectively. Figure 2.6 shows the corrected amplitude and phase reconstructions after applying 2, 8 and 20 iterations of the algorithm. After 8 iterations the algorithm reaches a stable point and the reconstruction no longer changes. The minimum transmittance in the initial reconstruction is 87 %, compared to 74 % after the correction (8 iterations), which is closer to the true value of 70%. Similarly, the peak phase change of the initial reconstruction is 0.50 radians and improves to 0.83 radians. The shape of the reconstructed field also improves significantly, note that the amplitude change is much narrower before the reconstruction. Figure 2.7 shows plots of a vertical cross section along the center of the image of the amplitude (Fig. 2.6a) and the phase (Fig. 2.6b) of the simulated object, the initial reconstruction and the corrected reconstruction after 8 iterations. It is clear from these plots that the accuracy of the reconstruction improves significantly and that the ringing due to the twin image is reduced. We have run the simulation for objects of different sizes and different field strengths and seen significant improvement in most cases. Objects with sharp edges are in general easier to correct since they have well-defined boundaries. The reconstructed error depends on the object field and increases with object size. The size of the objects captured in our experiments is in general

smaller than the object used for the simulation, and the algorithm usually converges to a stable solution within 4-10 iterations.

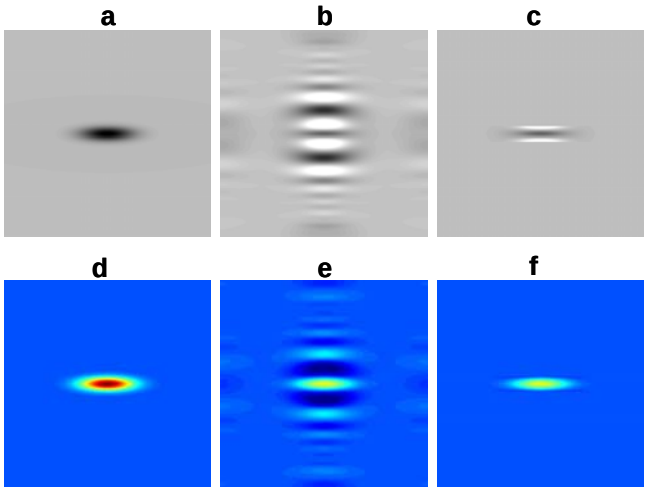

Figure 2.5. Simulation of object reconstruction. (a) Amplitude of simulated object field. (b) Initial amplitude reconstruction. (c) Intial guess for iterative reconstruction algorithm. (d-f) Phase of the light fields in (a-c), respectively. The phase is color coded such that red indicates a high value of the phase and blue corresponds to low values.

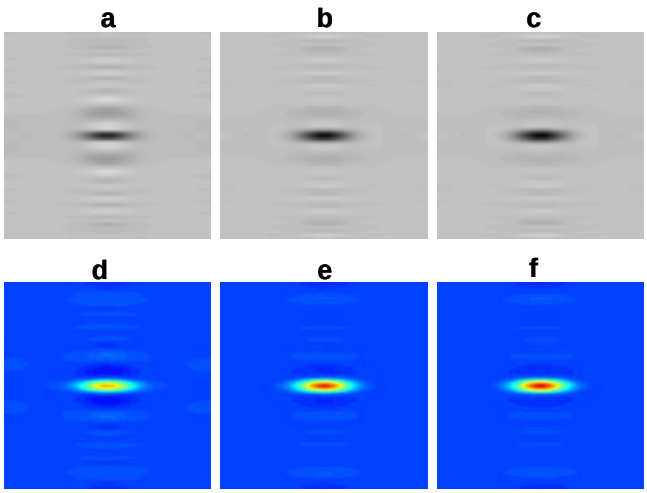

Figure 2.6. Amplitude and phase reconstructions with iterative algorithm. (a-c) Amplitude reconstructions after 2, 8 and 20 iterations. (d-f) Phase reconstruction after 2, 8 and 20 iterations.

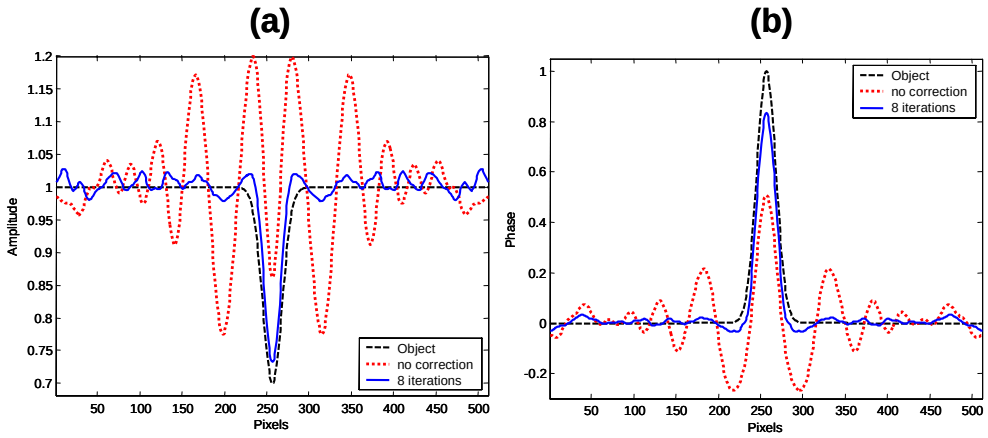

Figure 2.7. Cross sectional plots of simulated object (dashed black line), initial reconstruction (dotted red line) and the reconstruction after applying the correction algorithm (solid blue line). (a) Vertical cross section of the amplitude of the light along the center of the image. (b) Cross section of the phase.

Figure 2.8 shows the results of the correction algorithm when applied to an experimentally recorded hologram of a pulse propagating in water (the experimental results will be discussed in detail in the next chapter). Figure 2.8a shows a hologram recorded using approximately one quarter of the CCD area with the multiple-frame setup. The pump pulse generates an index change in the water, which induces a phase change in the probe pulse. Figure 2.8b-c shows the phase reconstruction before and after applying the correction algorithm (6 iterations). The fringes due to the twin image become much weaker and the detail around the object becomes sharper. Similar improvement was observed for most reconstructions. In the case of high resolution holograms with small filaments the improvement is not as significant since the initial reconstructions are already quite accurate. Finally, if a large phase change is measured it is necessary to unwrap the phase in order to calculate the index changes. Several algorithms have been developed to solve the problem of phase-unwrapping in 2-D. We have obtained good results with the algorithm developed by Volkov and Zhu [16].

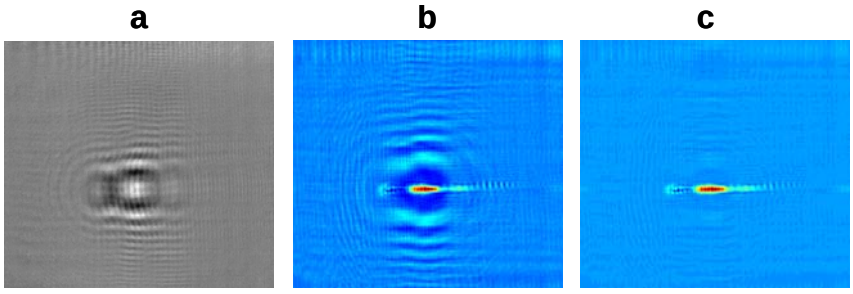

Figure 2.8. Phase reconstruction of an experimentally recorded hologram. (a) Hologram captured on the CCD camera using the movie setup. (b-c) Phase reconstruction before and after applying the correction algorithm. The light pulse propagates from left to right. The image size is 5.0 mm x 5.4 mm.

2.6 RECONSTRUCTION OF INDEX CHANGES

The nonlinear index changes in the material can be recovered from the phase information in the hologram. A probe that traverses a material with an index change will accumulate a phase change that is proportional to the index change in the material:

$$\Delta\phi(x,y) = \frac{2\pi}{\lambda}\int_0^L \Delta n(x,y,z)dz\,, \tag{2.22}$$

where we assume a probe propagating in the *z*-direction, Δn is the index change and L is the length of the index change traversed by the probe. L can be calculated from the beam size and the formulas in section 2.3. The previous formula can be used to reconstruct the index changes averaged over the *z*-direction:

$$\frac{\Delta\phi(x,y)}{2\pi} = \frac{L}{\lambda}\langle\Delta n(x,y)\rangle\,, \tag{2.23}$$

where the term in brackets is the index change averaged in the *z*-direction. This formula can be used to reconstruct the transverse profile of index change from the measured phase changes.

2.7. RESOLUTION LIMITS OF FEMTOSECOND HOLOGRAPHY

The temporal resolution of the holographic reconstruction is limited by the duration of the laser pulses. When recording with CW light or long laser pulses, the spatial resolution of on-axis holograms is determined by the numerical aperture. The minimum resolvable feature is

$$\delta_H = 0.61\frac{\lambda}{NA_H}\,, \tag{2.24}$$

where λ is the laser wavelength and NA_H is the numerical aperture of the hologram:

$$NA_H = \frac{D}{\sqrt{(2z)^2 + D^2}} \approx \frac{D}{2z}, \tag{2.25}$$

D is the detector size and z is the distance from the object to the recording plane (D is in general much smaller than z). In the case of digital holograms the resolution cannot exceed the detector pixel size unless the object is optically magnified. If magnification is used, the resolution will be determined by the smallest between the numerical aperture of the imaging system and numerical aperture of the hologram.

For very short pulses, however, the effect of the short coherence length needs to be taken into account. Consider a short pulse that illuminates a small object (Fig. 2.9a). The transmitted light (reference) is a plane wave, while the scattered light will propagate at a range of angles that depend on the spatial frequencies contained in the object. The time of arrival of the scattered light at the detector depends on the angle of propagation. Light scattered at larger angles (which corresponds to larger spatial frequencies) has to travel a longer distance to arrive at the detector. If the transmitted and scattered pulses do not temporally overlap on the detector they will not interfere, therefore limiting the effective numerical aperture. The maximum angle for which the scattered light will interfere with the transmitted plane wave is:

$$\cos\theta = 1 - \frac{c\tau}{z}, \tag{2.26}$$

where c is the speed of light and τ is the duration of the pulse. Assuming the duration of the pulse is much shorter than the travel time from the object to the detector ($c\tau << z$), the angle becomes:

$$\sin\theta = \sqrt{\frac{2c\tau}{z}} = NA_{pulsed}. \tag{2.27}$$

The effective numerical aperture will be the smaller of equations 2.25 and 2.27. For very short pulses (<100 femtoseconds) the coupling between temporal and spatial resolution can become a limiting factor, and it might require the use of optical magnification to achieve high resolution. The object can be magnified using a 4-F system (Fig. 2.9b) such that the object field is reproduced in the output plane with a magnification given by $M = f_2/f_1$. The advantage of using a 4-F system is that at the output of the system the reference will still be a plane wave. The effect of magnifying the object field is equivalent to reducing the curvature of the wavefront at the detector, thus reducing the difference in the arrival time between object and reference light fields. The maximum resolution that can be obtained for a given pulse duration is:

$$\delta_t = 0.61\frac{\lambda}{NA_{pulsed}}\frac{1}{M} = 0.61\sqrt{\frac{z}{2c\tau}}\frac{\lambda}{M}. \tag{2.28}$$

However, the requirement of having an object that is small relative to the recording area may impose a limit on the desired magnification. As a result, the object size, the magnification and the pulse duration all need to be considered in order to achieve the optimal design for a given application. We have found that for capturing the small filaments generated when the optical beam breaks up due to the nonlinear effects, a magnification of M = 12 provided good spatial resolution without compromising the accuracy of the reconstruction.

For the experiments with single frame capture, the numerical aperture of the 4-F system is NA = 0.25, the magnification is M = 12, z = 300 mm, λ = 800 nm, τ = 150 femtoseconds and the size of the hologram is 10 mm x 10 mm. The resolution limit due to the pulse duration becomes δ_t = 2.3 μm, while the resolution limit due to the numerical aperture is δ_H = 2.4 μm. We are close to an optimum point where we are at the limit of both spatial and temporal resolution. Beyond this point, we would have to sacrifice temporal resolution to improve the spatial resolution, and vice versa. With this setup we have experimentally measured features as small as 4 μm (see Chapter 2). For the experimental parameters used for the multiple frame capture (described in the next section), recording distance z = 200 mm and unit magnification (M = 1), the resolution limit imposed by the pulse duration is δ_t

= 23 μm. For the same parameters, and a hologram size of 5 mm x 5 mm (only a fraction of the CCD sensor area is used for each hologram), the resolution limit due to the *NA* of the hologram is δ_H = 39 μm; therefore in this case the pulse duration is not the limiting factor. However, for τ < 52 femtoseconds, the pulse duration would become the limiting factor. In this chapter we have covered issues specific to on-axis recording; for a general discussion of the problem of image recovery in off-axis holography with ultrashort pulses see the discussion in Leith et al. [17].

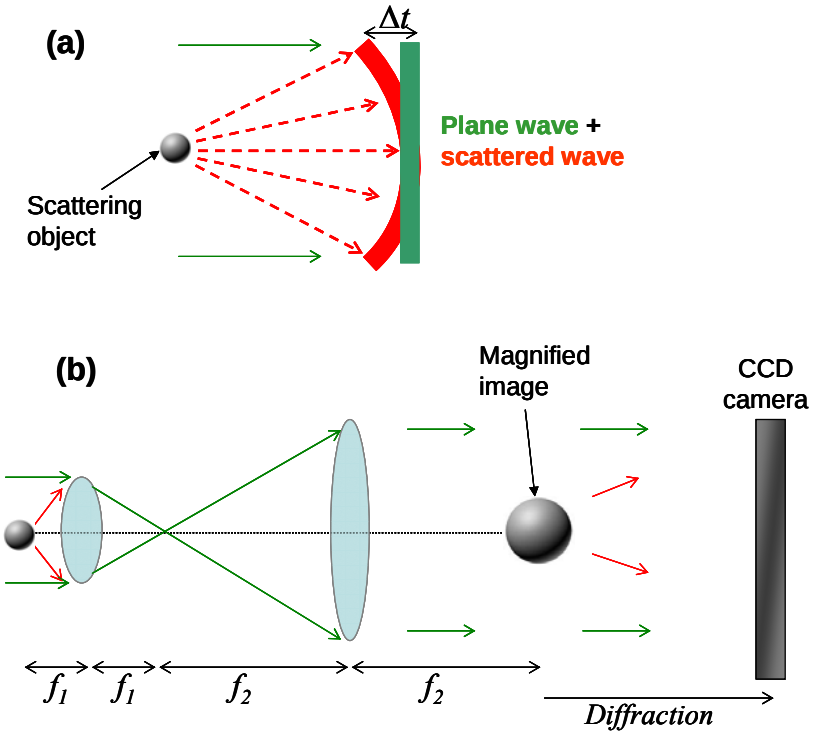

Figure 2.9. Resolution limit. (a) Coupling between temporal and spatial resolution. The time of arrival at the CCD sensor depends on the scattering angle. (b) The resolution can be improved by using a 4-F imaging system to magnify the object.

REFERENCES

[1] D. Gabor, Nature **161**, 777 (1948).

[2] H. J. Kreuzer, M. J. Jericho, I. A. Meinertzhagen, et al., Journal of Physics-Condensed Matter **13**, 10729 (2001).

[3] Z. W. Liu, G. J. Steckman, and D. Psaltis, Applied Physics Letters **80**, 731 (2002).

[4] S. Schedin, G. Pedrini, H. J. Tiziani, et al., Applied Optics **40**, 100 (2001).

[5] R. Boyd, *Nonlinear optics* (Academic Press, San Diego, 2003).

[6] G. P. Agrawal, *Nonlinear fiber optics* (Academic Press, San Diego, 1995).

[7] C. W. Dirk, W. C. Herndon, F. Cervanteslee, et al., Journal of the American Chemical Society **117**, 2214 (1995).

[8] A. Braun, G. Korn, X. Liu, et al., Optics Letters **20**, 73 (1995).

[9] A. Couairon, S. Tzortzakis, L. Berge, et al., Journal of the Optical Society of America B-Optical Physics **19**, 1117 (2002).

[10] A. Piekara, IEEE Journal of Quantum Electronics **QE 2**, 249 (1966).

[11] J. Goodman, *Fourier Optics* (McGraw-Hill, New York, 1996).

[12] G. Liu and P. D. Scott, Journal of the Optical Society of America A-Optics Image Science and Vision **4**, 159 (1987).

[13] M. H. Maleki and A. J. Devaney, Optical Engineering **33**, 3243 (1994).

[14] R. Gerchberg and W. O. Saxton, Optik **35**, 237 (1972).

[15] Y. Zhang, G. Pedrini, W. Osten, et al., Applied Optics **42**, 6452 (2003).

[16] V. V. Volkov and Y. M. Zhu, Optics Letters **28**, 2156 (2003).

[17] E. N. Leith, P. A. Lyon, and H. Chen, Journal of the Optical Society of America A-Optics Image Science and Vision **8**, 1014 (1991).

C H A P T E R 3

HOLOGRAPHIC CAPTURE OF FEMTOSECOND PULSE PROPAGATION

3.1. INTRODUCTION

We have implemented a holographic camera to capture the propagation of femtosecond pulses through different materials. The camera can record either a single hologram with high spatial resolution (4 μm) or a time-sequence of multiple holograms with reduced spatial resolution (60 μm) in a single-shot experiment. The fine spatial resolution allows us to zoom in and visualize the spatial profile of the pulses breaking up into multiple filaments, while the time sequence captures the evolution of the pulse propagation, preserving both amplitude and phase information. Laser pulses with a duration of 150 femtoseconds are used to probe the changes in the material properties and record holograms. The time resolution and the frame rate are limited only by the duration of the pulses. The holograms are recorded on a CCD camera and reconstructed numerically. The numerical reconstruction also allows us to reconstruct the light field at different axial positions, revealing 3-D information about the object. The reconstruction technique is described in the previous chapter.

We have studied the propagation of high energy femtosecond pulses in air, liquids (water and carbon disulfide (CS2)), and lithium niobate (LiNbO3), a nonlinear crystal. There are dramatic differences in the pulse propagation characteristics depending on the strength of the nonlinear coefficient of the material and its time response. The phase recovered from the holograms helps us identify the nonlinear index changes in the material. We have measured both positive and negative index changes. Positive index changes are attributed

to the Kerr nonlinearity, while negative index changes are caused by ionization of the medium (see Chapter 2). The strength and time constant of the Kerr effect can be inferred from the positive index change. The density of free electrons can be calculated from the plasma index changes.

3.2. EXPERIMENTAL SETUP

3.2.1. Single-frame capture

Figure 3.1 shows the setup used to record an on-axis hologram with a femtosecond pulse [1]. A pulse from a Ti:sapphire laser amplifier operating at 800-nm wavelength is used to generate the ultrafast event and also to record it. The laser pulses have a duration of 150 femtoseconds and a maximum energy of 2 mJ. The beam is approximately Gaussian with a diameter of 5 mm (FWHM). The pulse is split in two, with a major portion of the energy going into the pump beam. A delay line (mirrors M1 and M2) is used to synchronize the arrival of the pump and probe pulses. The pump beam is focused with an achromatic lens (L3). A lens with a focal length of 100 mm is used for the experiments with liquids, and a 50 mm focal length lens is used for the experiments in air. For the experiments with air, ambient air is used, and the propagation is observed near the focal region. For the experiments with liquids, a glass cell (4 cm in length) is filled with the liquid. The focal point of the lens lies approximately 10 mm inside the cell. The probe propagates in a direction perpendicular to the pump and captures the interaction of the pump with the material. The image is magnified by a factor of $M = f_2/f_1$ using lenses L1 and L2, with focal distances of f_1 = 16.5 mm and f_2 = 200 mm, respectively. A CCD camera (Apogee AP32ME, 2184 x 1472 pixels, 6.8 μm pixel size) is placed at a distance L = 25-35 cm from the image plane to capture an on-axis hologram. The digitized hologram is then numerically reconstructed to retrieve the phase and amplitude changes induced in the probe as it traverses the material. The time resolution of the holograms is limited by the duration

of the pulses (150 femtoseconds). The spatial resolution is limited by the numerical aperture of the hologram.

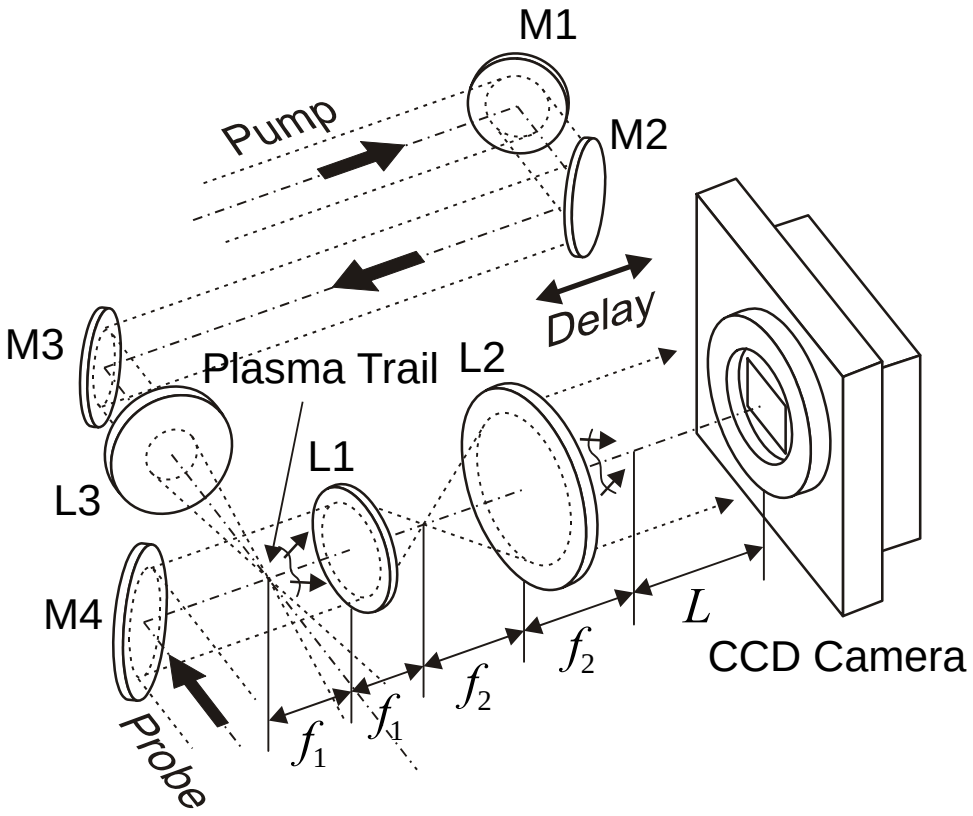

Figure 3.1. Experimental setup for single hologram recording.

3.2.2. Multiple-frame capture (holographic movie)

The setup in Figure 3.1 was modified to record a time-sequence of four holograms with a single laser pulse. Mirror M4 is replaced with a mirror array consisting of four mirror segments (Fig. 3.2), each of which has independent controls for angular and axial displacements. Each mirror is mounted on an independent translation stage and has controls for tilt in two dimensions. Four probe pulses are generated by reflecting a single pulse off the mirror array. The input beam is expanded and only the central region is used such that the intensity of the probe beams is uniform. An aperture is placed at the mirror array to

limit the probe beams to a square size with a width of 5 mm. The position of the mirrors controls the relative time delay between the probes, while the angle controls the propagation direction. The four probes are made to spatially overlap in the interaction region (and then spatially separate on the recording plane). Each probe pulse samples the event at a time set by the displacement of the mirror. The relative time delay between the probes can be adjusted to match the time window of interest, while a delay line on the pump arm synchronizes the arrival of pump and probe pulses. The angle between the pump and probe pulses is reduced to 30 degrees (outside the material) in order to increase the length of interaction of the pump and probe pulses. The four spatially multiplexed on-axis holograms are recorded on a single frame of the CCD camera. After traversing the interaction region the probe light propagates a distance of 200 mm to the CCD camera (no lenses are used). We set the separation angle between the probe pulses sufficiently small (1.4º) so that the events are captured at approximately the same angle. In order to spatially separate the four holograms in the CCD sensor, the effective angular aperture of each individual hologram is limited to the separation angle between the probe pulses. The spatial resolution of each hologram is determined by the angular aperture.

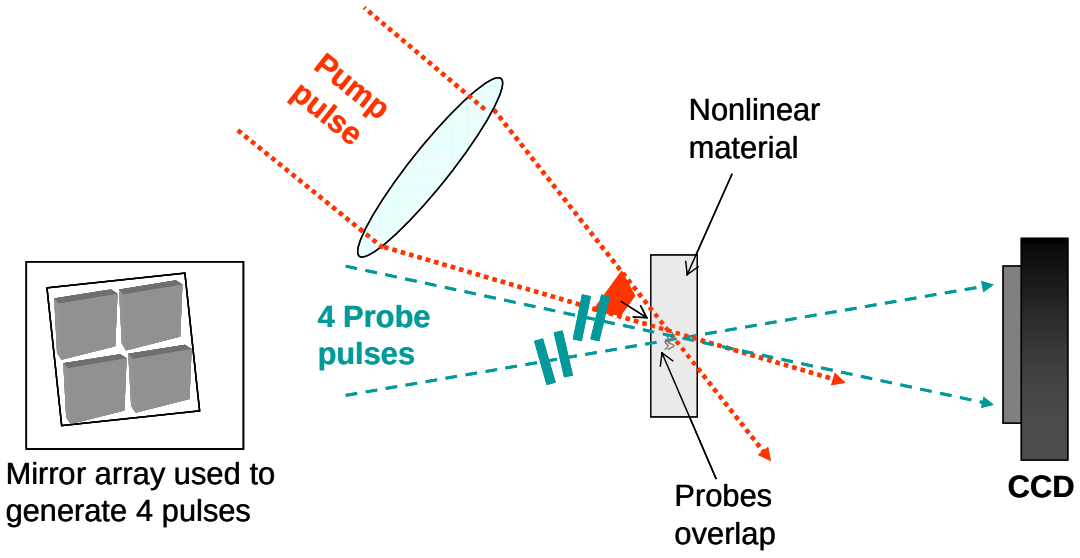

Figure 3.2. Experimental setup for holographic movie recording.

3.3. EXPERIMENTAL RESULTS WITH SINGLE-FRAME CAPTURE

3.3.1. Digital recording and background subtraction

In holographic recording the optical beams are generally spatially filtered using an objective lens and a small aperture or pinhole to produce clean uniform beams. However, it is difficult to perform spatial filtering on amplified femtosecond pulses due to strong nonlinearities in the focal region. We have to a large extent removed the effects of spatial noise on the laser beam by first recording an image of the reference light only (the pump beam is blocked) (Fig. 3.3a) and using it as a background that can be subtracted to produce a clean hologram. Fig. 3.3b and 3c show a hologram before and after background subtraction. The diffraction of the probe is caused by a region of ionized air. The image in Fig. 3a is subtracted from the image in Fig. 3.3b, and the mean level of intensity is restored to generate the hologram in Fig. 3.3c. The hologram is much cleaner and contains only the modulation due to the presence of the pump beam.

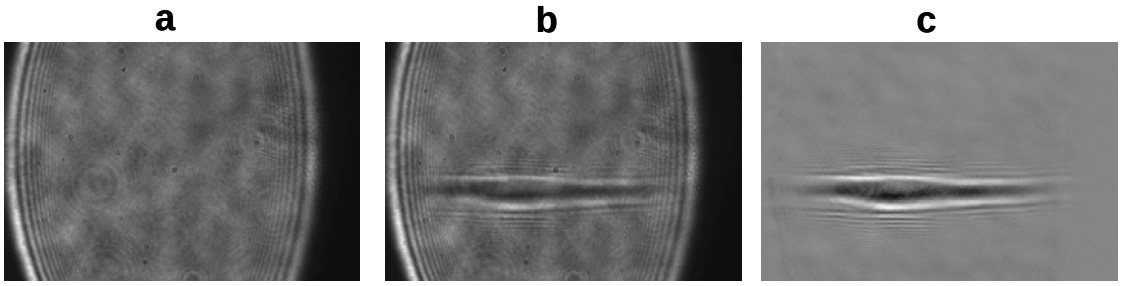

Figure 3.3. Background subtraction to remove artifacts due to spatial noise on the optical beam. (a) Image of the reference beam without the signal (the pump beam is blocked). (b) Hologram with the pump beam on. (c) The image in (a) is subtracted

from the image in (b) and the mean intensity level is restored to produce a cleaner hologram.

3.3.2. Pulse propagation in air, water and CS_2

We have used the single frame setup (Fig. 3.1) to study pulse propagation in air, water and carbon disulfide (CS_2). The amplitude and phase of the light field at the object plane is numerically reconstructed from the holograms, using the methods described in the previous chapter. The main material properties that play a role in the propagation are the strength and time response of the Kerr effect and the ionization energy. The materials studied have very little linear absorption at the wavelength of the laser, though nonlinear absorption can be significant. The Kerr coefficient will determine how fast the beam breaks up into filaments and the power contained in each filament. The ionization energy determines the intensity threshold at which plasma is generated. The plasma is generated through multiphoton absorption and creates a negative index change in the material. The interplay between these two effects determines the intensity of the filaments. If the medium is not ionized, a higher order nonlinear effect will eventually balance the Kerr self-focusing, as in the case for propagation in CS_2. The filament dynamics in CS_2 will be studied in more detail in the following chapters.

The different Kerr response of these materials gives rise to dramatically different behavior. The Kerr coefficient (Equation 2.3) for the different media are: $n_{2(\mathrm{Air})} = 3\mathrm{x}10^{-19}$ cm^2/W [2], $n_{2(\mathrm{Water})} = 4\mathrm{x}10^{-16}$ cm^2/W [3] and $n_{2(\mathrm{CS2})} = 3\mathrm{x}10^{-15}$ cm^2/W [4] for femtosecond pulses. There are two time constants associated with the nonlinear response in CS_2. The fast time response, measured with femtosecond pulses, corresponds to an instantaneous electronic response. There is also a molecular response with a time constant of about 2 picoseconds. Given the duration of the pulses used in our experiments (150 femtoseconds), the propagating pulse will be affected mainly by the fast time response, while the slower time response will grow after the pulse is gone. Each filament carries approximately the critical power; therefore we expect more filaments in materials with larger Kerr coefficient. The

critical power is calculated using equation 2.4: $P_{crit\ (air)} = 1.9 \times 10^9$ W, $P_{crit\ (Water)} = 1.8 \times 10^6$ W, $P_{crit\ (CS2)} = 1.9 \times 10^5$ W. The formation of plasma depends on the intensity level reached in the filaments. For excitation with femtosecond pulses, the dominant mechanism for ionization is multi-photon absorption[5]. The ionization energies for air, glass and CS_2 are similar (E_{CS2} = 10.1 eV, E_{water} = 12.6 eV, $E_{nitrogen}$ 15.6 eV, and E_{oxygen} 12.1 eV), leading to an intensity threshold for laser induced breakdown of approximately 2 x 10^{13} W/cm^2 for all of them. The intensity threshold can be calculated using the Keldysh method [5, 6]. The intensity thresholds for ionization were previously calculated for air (I_{th} = 2 x 10^{13} W/cm^2 [7]) and CS_2 (I_{th} = 2 x 10^{13} W/cm^2 [8]), and measured in water (I_{th} =1.2 x 10^{13} W/cm^2, [9]). The variation in the ionization energies is within the uncertainty of the calculation method, which is approximately a factor of 2 [10]. The number of photons that must be absorbed simultaneously to ionize the medium depends on the ionization energy and the photon energy (1.55 eV for a wavelength of 0.8 μm).

We first present the results for propagation in air. A pump pulse with energy of 1 mJ is focused in ambient air. Breakdown of the air is observed in the focal region. Figure 3.4a shows an image of a typical plasma discharge generated in the air. The image shows the light emitted from the discharge (without the probe light), which is strong enough to be seen by eye in a dark room. The presence of the spark is indicative of high plasma densities. Figure 3.4b-c shows the background-subtracted hologram and the phase of the probe reconstructed numerically. The hologram is captured less than 1 picosecond after the pulse traverses the focal region. A strong negative index change is observed in the focal region of the lens, where the beam splits up into multiple filaments. The negative index change is attributed to the formation of plasma in the regions of high intensity. The amplitude of the light is only weakly modulated by the presence of the plasma. The plasma region has a maximum width of 50 μm and length of 800 μm. The free electrons are generated in filaments with diameters of 5-10 μm. As the optical beam is focused, it breaks up into filaments through modulation instability. The filamentation pattern of the beam is reflected in the plasma distribution. The plasma filaments can be smaller than the optical filaments since they are generated through a multi-photon process. The minimum filament size is close to the resolution limit of the system, so it is possible that some filaments are

smaller. The index change inside the filaments varies from Δn = 2 x 10^{-3} to 2 x 10^{-2}. The electron density can be calculated from the index change using equations 2.5 and 2.6. The density of electrons in the plasma filaments varies between 7 x 10^{18} cm^{-3} and 7 x 10^{19} cm^{-3}. Most of the plasma generated is concentrated in the filaments, which are confined to the focal region. The mean plasma density over the focal volume is on the order of 10^{17} cm^{-3}. The peak plasma densities that we measured are two orders of magnitude higher than expected for long range filaments, i.e., filaments that propagate in air for several meters [11, 12]. While the plasma in long range filaments results from a balancing between Kerr self-focusing and plasma defocusing, in our experiments higher plasma densities are caused by the strong focusing geometry. The beam profile of the pulse after going through the focal region has a dark region in the center, where the beam was absorbed more strongly. A fraction of the energy in the beam is converted to visible (red) light through the process of continuum generation [13].

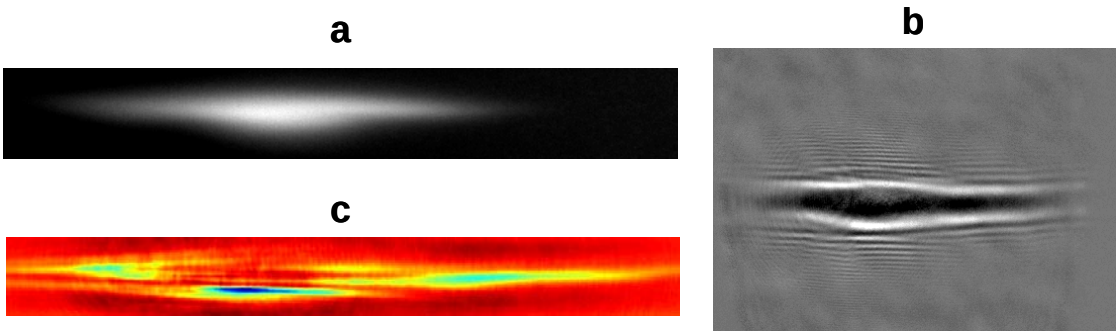

Figure 3.4. Laser induced discharge in air. (a) Image of laser discharge in air (0.09 mm x 0.80 mm). (b) Hologram of the laser induced breakdown in air (0.83 mm x 1.24 mm). (c) Reconstruction of the phase changes from the hologram in b (0.09 mm x 0.80 mm). Red indicates high values of the phase and blue low values. The pulse propagation is from left to right in the images.

We have also recorded holograms of pulses propagating in water and CS_2. Figure 3.5 shows (a) the amplitude and (b) phase reconstruction for a 700 μJ pulse propagating in water, while (c) and (d) display the amplitude and phase reconstructions for a 50 μJ pulse propagating in CS_2. Different pulse energies were used because the nonlinearities are stronger in CS_2. Higher pulse energies in CS_2 resulted in the beam breaking up into a large number of filaments very quickly, which made it difficult to capture the beam profile.

For a pulse propagating in water, the beam has an envelope that follows the linear focusing of the lens, while inside the envelope the beam breaks up into multiple filaments before reaching the focal plane (Fig. 3.5a-b). The propagation direction of the filaments is determined by the local wave-vector. More specifically, since the beam has a spherical wavefront, the filaments propagate inside a cone determined by the focusing lens. No filaments were observed after the focal plane. A trail is left after the pulse traverses the medium. In figure 3.5a-b the pulse is at the leading edge of the filaments, while the dark region to the left is the trace left in the material. The trace is characterized by a decrease in transmission of about 30 % with only small phase changes. In contrast, the filaments at the leading edge generate large negative phase changes and small amplitude changes. The size of the filaments is approximately 5 μm, and the index change is $\Delta n = -10^{-2}$. The negative index change results from the formation of plasma in the regions of highest intensity. This index change corresponds to a plasma density of 3×10^{19} cm^{-3} inside the filaments.

Vapor bubbles were formed near the focal region in the water. Fig. 3.6a shows an image of the bubbles taken with the experimental setup in Fig. 3.1 by moving the CCD camera to the image plane of the 4-F system. The bubbles, which appear as dark circles in the image, were captured by launching pulses through the water continuously (the laser has a repetition rate of 10 Hz) for a few seconds before recording an image, so that the probe pulse captures the trace of the current pump pulse and the bubbles generated by previous pump pulses. The bubbles result from localized boiling in the focal region and drift upwards. Bubbles are expected to appear for plasma densities above 10^{18} cm^{-3} [14]. In contrast to the plasma in air, we did not observe a discharge in the focal region, which is expected for plasma densities on the order of 10^{20} cm^{-3} [9]. However, we did observe light emission from multiple localized spots starting about 0.5 mm before the focal plane (Fig.

3.6b-d). The bright spots are generated in the focal region by the pump pulse. The distribution of spots changes completely from shot to shot (Fig. 3.6c-d). The strength of the emission and the number of spots were much higher when the polarization was perpendicular (vertical) to the direction of the observation plane (horizontal). Further experiments are necessary to explain the physical origin of the bright spots.

The plasma filaments appear 1-2 mm before the focal plane. The beam breaks up into filaments sooner than in air because the nonlinearity is stronger. The dark trace seems to be the result of large numbers of plasma filaments forming and scattering or absorbing light from the probe pulses. If the leading edge is observed just two picoseconds after the pulse has gone through it also becomes a dark trace. From further pump and probe experiments we were able to estimate the lifetime of the plasma trace to be 0.5 nanoseconds, much longer than the time it takes to generate it. A strong white light continuum [13, 15] was observed at the output of the glass cell containing the water. Most of the pulse energy is either absorbed or converted into white light after traversing the full length of the cell (4 cm).

In CS_2 we measured a positive phase change and an increase in intensity near the center of the pulse position (Fig. 3.5c-d). The phase change corresponds to a positive index change generated by the pump pulse through the Kerr effect. The region of nonlinear index change acts as a focusing lens for the probe light to generate the higher intensity region. As opposed to propagation in water, no plasma was measured in CS_2. The intensity of the filaments was below the breakdown threshold. In the absence of a plasma index change, the filaments will either continue to self-focus until they reach a size comparable to the wavelength and then diffract, or propagate with a stable diameter if the Kerr self-focusing is balanced by another nonlinear effect. In the case of CS_2 there is a saturation of the nonlinear index change (possibly through a fifth order nonlinearity) that causes a clamping of the intensity in the filaments [16]. The formation of stable light filaments in CS_2 is the subject of Chapter 4. The index change, and thus also the intensity of the filaments, saturates before the breakdown threshold is reached. In the reconstructed phase (Fig 3.6-d) we have observed multiple filaments with diameters of 8-15 μm and an index change of approximately $\Delta n = 7 \times 10^{-4}$. It is difficult to determine the size of the filaments accurately

because they are packed very close together, separated only by 5-10 μm. We can obtain a rough estimate of the intensity of the filaments from the index change, assuming the index change is due only to the Kerr effect, $\Delta n = n_2 I_{Filament}$, which leads to $I_{Filament}$ = 2 x 10^{11} W/cm^2. This intensity level is two orders of magnitude smaller than the breakdown threshold. Our estimated value is about 3 times smaller than measured values of the intensity of filaments in CS_2 [8] (see Chapter 4). The difference is expected since we did not account for the saturating mechanism in our calculation. The region of index change in CS_2 is shorter than the trail in water. At the leading edge of the pulse, the pump and probe pulses temporally and spatially overlap, giving rise to the region with a stronger index change in Fig. 3.6d. A trail of weaker index change is also observed behind the pulse. The stronger signal at the overlap of the two pulses is due to the instantaneous (electronic) Kerr response of the material, while the trail is due to the slower (molecular) response. The length of the trail is consistent with the expected lifetime of the index change of approximately 2 picoseconds.

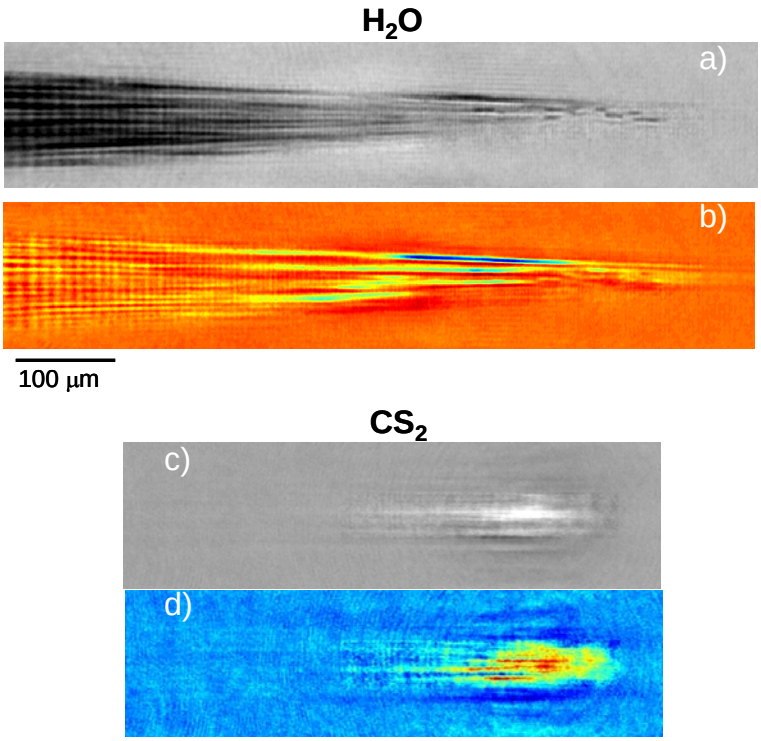

Figure 3.5. Amplitude and phase reconstructions of femtosecond pulse propagation in liquids. The light pulse propagates from left to right in the images. (a) Amplitude and (b) phase reconstructions for a 700 μJ focused pulse propagating in water. (c) Amplitude and (d) phase reconstructions for a 50 μJ focused pulse propagating in CS_2. Red corresponds to high values of the phase and blue to low values. The size of the images is 0.15 mm x 0.76 mm for a-b and 0.15 mm x 0.54 mm for c-d.

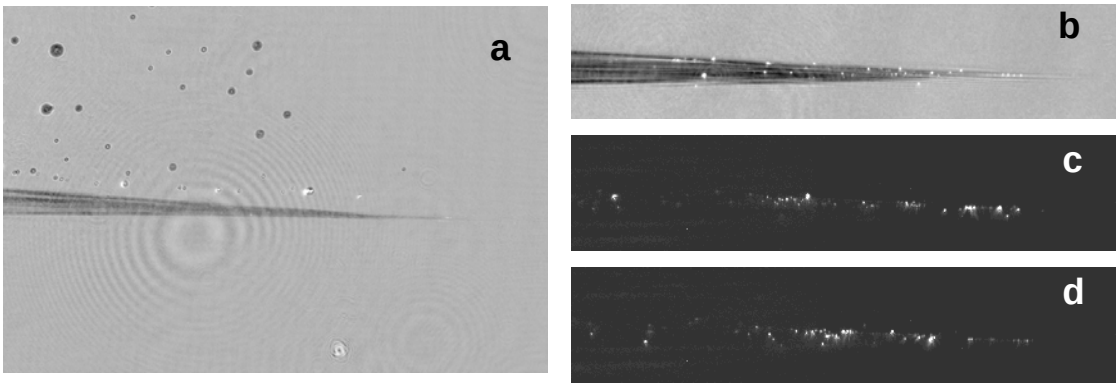

Figure 3.6. Formation of bubbles and hot spots in water. (a) Bubbles are formed in the focal region and drift upwards. The diameter of the bubbles ranges from 4 μm to 30 μm. (b) Light emission from localized spots, observed when the laser polarization is perpendicular to the direction of observation. (c-d) Images of the bright spots with the probe beam blocked for two different laser shots. A completely different pattern of bright spots appears with each laser shot. The image size is 0.83 mm x 1.24 mm in (a) and 0.24 mm x 1.13 mm in (b-d). The light pulse propagates from left to right in the images.

3.3.3. Comparison of the holographic phase reconstruction with an interferometric phase measurement

The accuracy of the holographic reconstruction was verified by comparing the results with an interferometric measurement of the phase changes (Fig. 3.7). A hologram of an air discharge was recorded using the setup described in section 3.2.1, with a recording distance of L = 25 cm. Several plasma filaments are generated in the focal region, which induces a negative phase change in the probe pulse. Multiple experiments with the same conditions resulted in similar patterns of plasma filaments. For the interferometric measurement, the

CCD camera is moved to the image plane (L = 0 cm), and the probe pulse is made to interfere with a uniform reference pulse. The reference pulse is brought from the side at a small angle using a beam splitter and is synchronized to the arrival of the probe pulse. Figure 3.7b shows the bending of the interference fringes due to the index change of the plasma, and Fig. 3.7c shows the phase reconstructed digitally from the on-axis hologram. The regions of high phase change in the holographic reconstruction correspond to the regions where the interference fringes bend more sharply on the interferogram. The maximum phase change is approximately -1.5 radians, which correspond to approximately a $\pi/2$ phase shift in the interference fringes. The phase reconstructed from the interferometric measurement is in good agreement with the holographic reconstruction. Small differences between the two phase reconstructions are attributable to shot-to-shot fluctuations in the plasma distribution.

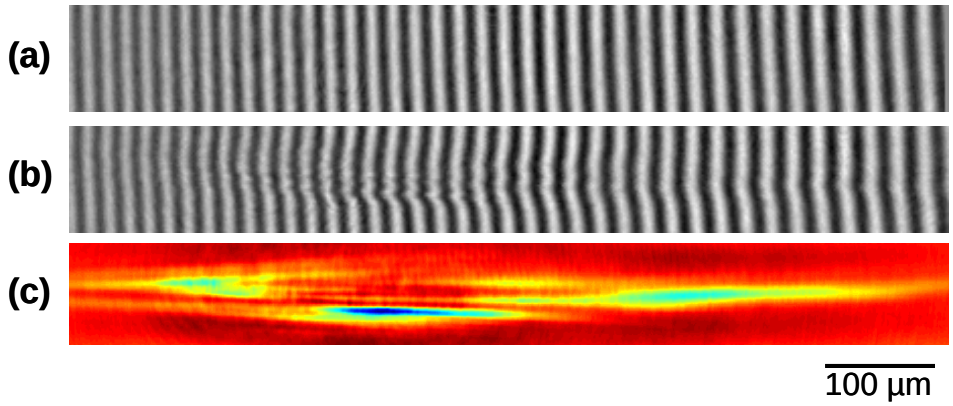

Figure 3.7. Comparison of on-axis reconstruction with interferometric phase measurement. a) Interferogram without phase change (the pump is blocked). b) Interferometric measurement of the the phase change due to the plasma filaments. c) Holographic reconstruction of the phase change. Red indicates high values and blue low values of the phase. The blue region is the region with the maximum absolute value of phase change. The images are 0.09 mm (vertical) x 0.80 mm (horizontal).

3.3.4. Reconstruction of 3-D information

A hologram of pulse propagation in CS_2 was digitally re-focused at different planes to reveal the three-dimensional structure of the beam profile. The estimated axial resolution of the reconstruction is 20 μm and is limited by the numerical aperture of the hologram. In the case of beam propagation through CS_2 the diameter of the filaments is 8-15 μm, but the diameter of the beam is close to 50 μm. Due to the limited depth resolution the filaments will appear elongated in the axial direction. We have numerically reconstructed the hologram at three different planes, separated by a distance of 40 μm between each plane, to obtain three depth slices (cross sections) of the beam profile. Figure 3.8 shows the phase of the light field at the three different planes. Each reconstruction reveals a different filamentation pattern as different filaments come to focus. A single filament near the bottom of the image is in focus in Fig. 3.8a, while the rest of the filaments are out of focus. In Fig. 3.8b-c the filament at the bottom is out of focus, and different filaments come to focus in the central region for the two different re-focusing distances. A higher numerical aperture could be used for a full 3-D reconstruction of the filamentation pattern.

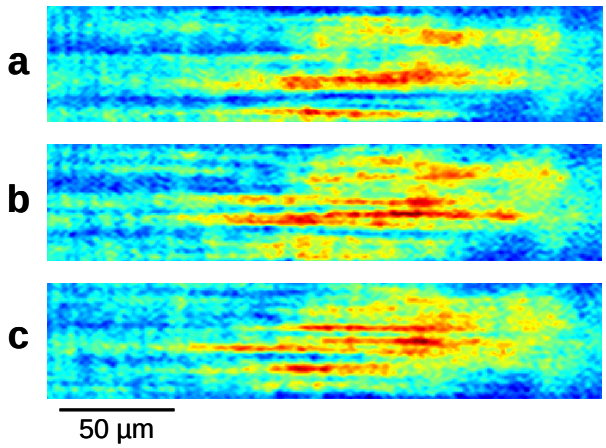

Figure 3.8. Three depth slices of the object reconstructed from a single hologram. The images show the phase of the light at 3 different planes by changing the reconstruction distance in steps of 40 μm. The cross sections reveal the 3-D structure of the filamentation pattern. (a) A filament in the lower part of the image comes to

focus while the rest of the structure is out of focus. (b) A pattern of filaments appears in the center region, and the filament in the lower part of the images is now out of focus. (c) A different set of filaments comes to focus in the central region of the image. The size of the images 0.05 mm x 0.24 mm.

3.4 EXPERIMENTAL RESULTS WITH MULTIPLE-FRAME (MOVIE) SETUP

3.4.1. Recording spatially multiplexed holograms.

A time sequence of four spatially multiplexed holograms was captured with the single-shot setup (Fig. 3.2). We compare the propagation dynamics in water, CS_2 and a $LiNbO_3$ crystal. The Kerr coefficient of $LiNbO_3$, measured with femtosecond pulses at a wavelength of 776 nm, is $n_2 = 1.0 \times 10^{-14}$ W/cm^2 [17], stronger than both water and CS_2. The probes propagate in a direction perpendicular to the CCD camera, while the pump traverses the material at an angle. The angle between the pump and probe pulses is set to 30 degrees outside the medium. The angle inside the material varies depending on the index of refraction ($n = 1.33$ in water, $n = 1.63$ in CS_2 and $n = 2.2$ in $LiNbO_3$). The angle difference is in the horizontal direction, as observed on the camera. Smaller angles lead to longer interaction lengths and increased signal strength as the phase change accumulates over a longer distance. If the pump pulse leaves a trail in the material that lasts longer than the time window of the experiment (a few picoseconds), then a probe pulse arriving after the pump will capture the entire trail. An instantaneous effect, however, can only be captured when the pulses overlap temporally and spatially. The overlap of pump and probe pulses is described in Section 2.3.

Figure 3.9 shows a time sequence of four holograms of pulse propagation in water captured in a single frame of the CCD camera. A 150 femtosecond pump pulse with 300-μJ energy is focused inside a glass cuvette filled with water. A background image is captured with only the probe beams (Fig. 3.9a) and used to remove artifacts in the hologram caused by modulation of the probes. The diffraction fringes in the probes are caused by reflection from the square segments in the mirror array. The four beams are spatially separated in the CCD sensor and temporally separated by a relative time delay of 0, 0.7, 1.3 and 2.3 picoseconds for sub-frames 1, 2, 3 and 4, respectively. A second image is captured with the pump beam overlapping with the probes inside the medium (Fig. 3.9b). There is some weak modulation of the probe beams due to the pump, but it is difficult to visualize it due to the spatial noise in the probe beams. The holograms are corrected by subtracting the image in Fig. 3.9a from the image in Fig. 3.9b and restoring the background light intensity to the mean intensity in Fig. 3.9b. Fig. 3.9c shows the resulting background subtracted holograms, after cutting the four sub-frames from the single CCD frame. The modulation that is left is due only to the interaction of pump and probe beams and can be used to reconstruct the amplitude and phase of the probe pulses.

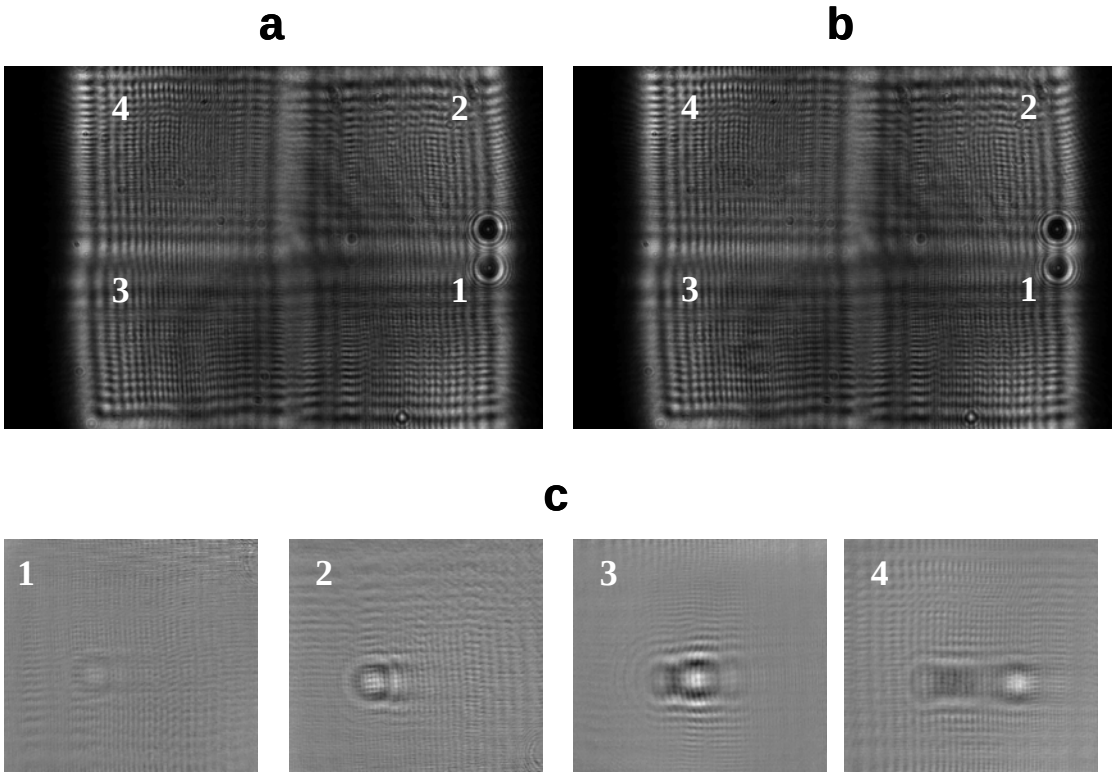

Figure 3.9. Time sequence of pulse propagation in water on a single frame of the CCD camera. a) Four plane-wave probe beams on the CCD camera (the pump beam is blocked). The fringes result from an aperture used to shape the beams. b) Four on-axis holograms with relative time delays of 0 ps, 0.7 ps, 1.3 ps and 2.3 ps. A weak modulation can be seen near the center of each frame. c) The individual holograms (sub-frames) after the background is subtracted.

3.4.2. Propagation dynamics in liquids: water and CS_2.

Figure 3.10 shows the amplitude and phase reconstructed from the holograms in Fig. 3.9c. The amplitude and phase are numerically reconstructed using the algorithm described in Section 2.5. We compare the pulse propagation in water with propagation in CS_2. The

nonlinearity is stronger in CS_2, so the pulse energy is reduced to 50 μJ. Figure 3.11 shows the reconstructed amplitude and phase for probe pulses with a relative time delay of t = 0 ps , 1.0 ps, 2.0 ps and 3.0 ps. In the first frame (Fig. 3.10a and 3.11a) the probe pulse interacts only with the leading edge of the pump, and a weak signal is captured. The second and third holograms (Fig. 3.10b-c and 3.11 b-c) capture the pulse before the focal point, while the fourth frame (Fig. 9d and 10d) captures the pulse after the focal point. The diameter of the beam in the focal region is approximately 150 μm in water (Fig. 3.10c) and 60 μm in CS_2 (Fig. 3.11c). The weak amplitude changes in Fig. 3.11a, 3.11c-d are the result of the long depth of focus of the system and possibly numerical errors. Since the object cannot be reconstructed exactly at the image plane the phase changes will generate some modulation of the amplitude. The dark region in the amplitude reconstruction in Fig. 3.11b is due to a strong phase change experienced by the probe. The index change acts like a lens that focuses the light in a short distance so that it defocuses quickly and some of the light misses the detector. The amplitude of the light in the dark region is approximately 55% of the background light level. The Kerr effect in CS_2 has both instantaneous and non-instantaneous contributions, so as the pulse traverses the liquid it leaves a trace of positive index change. The trace shows the pulse entering the medium, focusing to a small spot and defocusing. Using longer time delays between the pump and the probes we measured a decay time constant of the non-instantaneous index change of 1.7 picoseconds, in good agreement with the values reported in the literature [3].

The nonlinear index change in water is instantaneous (on the order of a femtosecond), so instead of a trace we capture a snapshot of the intensity profile of the pulse. The measured index changes in the focal region are 6×10^{-4} in CS_2 and 1×10^{-4} in water. The index change of the trail in CS_2 increases as the beam width decreases. Note that even though the pulse energy was 6 times higher in water, the index change in CS_2 greater. The positive index change is due to the Kerr effect, in contrast to the negative index change due to plasma generation. The index change in the focal region in CS_2 is lower than expected from the Kerr effect alone for the given pulse intensity, which indicates a saturation of the index change. In the case of water, the pulse energy in the focal region is lower than at the input, since a fraction of the energy is lost to plasma generation. The phase reconstruction in

water also shows a weak trail of negative index change, which corresponds to the long-lasting plasma trail observed with the high resolution holograms. The dark regions in the amplitude reconstructions in Fig. 3.10 correspond to the plasma trail where a large number of plasma filaments are formed that scatter and absorb the probe light. When the angle between pump and probe is reduced, the long interaction region induces a higher phase change for the Kerr effect, which occurs everywhere the pump and probe pulses overlap. The negative index change is located in the small filaments that cannot be resolved with the movie setup.

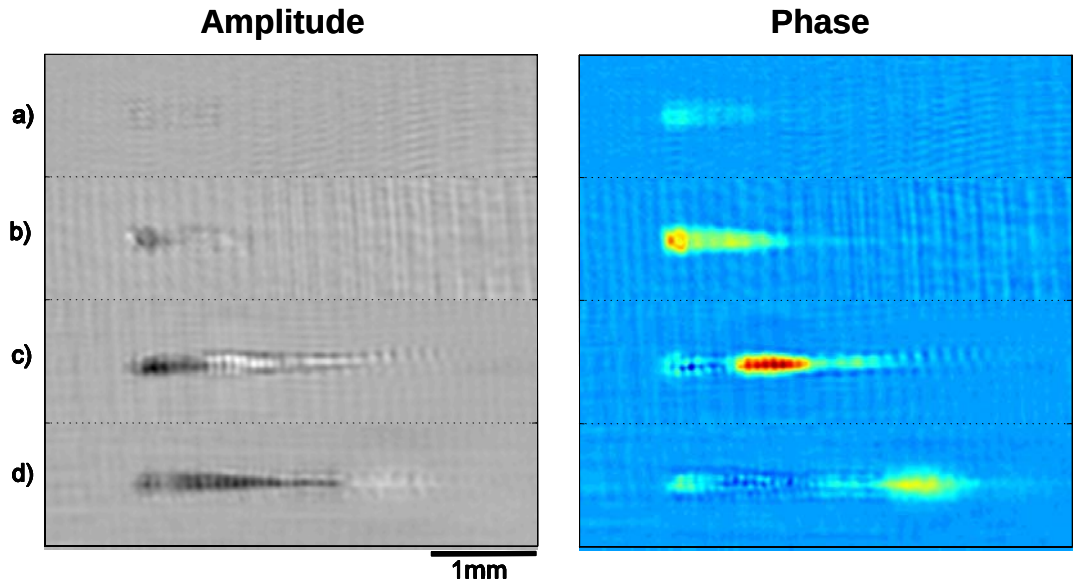

Figure 3.10. Holographic amplitude (left) and phase (right) reconstructions of femtosecond pulse propagation in water. The relative time delay is (a) 0 ps, (b) 0.7 ps, (c) 1.3 ps and (d) 2.3 ps. The maximum phase change in is 0.6 radians in (c). Each sub-frame is 4 mm (horizontal) by 1 mm (vertical).

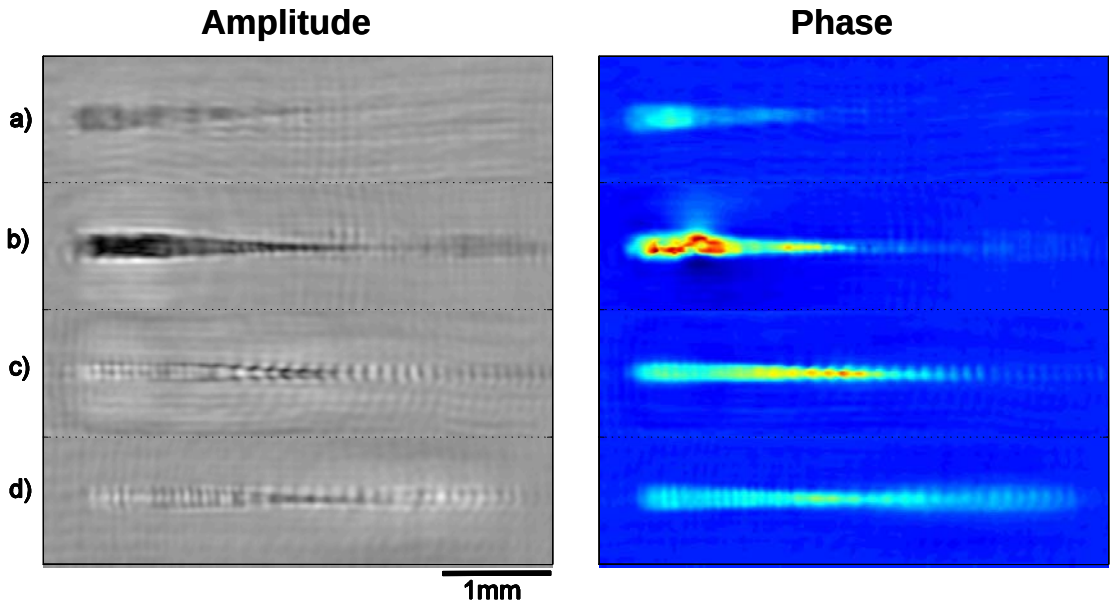

Figure 3.11. Holographic amplitude (left) and phase (right) reconstructions of femtosecond pulse propagation in CS_2. The maximum phase change in is 4 radians in (b) and 2 radians in (c). The relative time delay is (a) 0 ps, (b) 1.0 ps, (c) 2.0 ps and (d) 3.0 ps. Each sub-frame is 4 mm (horizontal) by 1 mm (vertical).

3.4.3. Pulse propagation in $LiNbO_3$

We have also studied the propagation of pulses through a $LiNbO_3$, a crystal with strong photorefractive and second order nonlinearities commonly used as a recording medium in holography, for second harmonic generation and in many other applications. Here we explore the effects of its strong Kerr nonlinearity that leads to large intensity-dependent index changes. A pulse with 300 μJ energy is focused into a 0.6 mm spot size at the entrance face of the crystal using a lens with a focal length of 200 mm. A large spot size was used to avoid damaging the crystal. The crystal thickness is 5 mm. For high pulse energy, a permanent index change is generated inside the crystal through the photorefractive effect after single pulse illumination. We have used the single shot setup to

capture the propagation, and when multiple movies were recorded the crystal was moved to insure that the photorefractive index change did not interfere with the measurements. Figure 3.12 shows the amplitude and phase reconstruction for four probe pulses with relative time delay of 0 ps, 1.0 ps, 2.0 ps and 3.0 ps. The larger beam size in this experiment means the distortion due to the twin image is stronger and in some cases cannot be removed completely. An example is the reconstruction in Fig. 3.12b where there are fairly strong fringes around the bright region in the center. We estimate the uncertainty in the reconstruction values to be around 20-30 %.

In the first frame (Fig. 3.12a) the probe overlaps only with the leading edge of the pump pulse at the entrance face of the crystal. The phase change results from an instantaneous Kerr response (positive index change) in the medium. There is a small change in the reconstructed amplitude. Amplitude changes are caused by instantaneous induced absorption of the probe light. Two photons from the pump are absorbed along with one photon from the probe [17]. However, the amplitude changes observed in the first frame are also consistent with reconstruction errors due to the depth of focus of the system. In the second frame (Fig. 3.12b) there is a maximum overlap of the pulses inside the crystal, which generates a strong amplitude and phase change in the probe. In this case we attribute the amplitude changes to induced absorption. The maximum phase change is 0.6 radians. The regions of increased intensity are attributable to a focusing effect on the probe due to the index change. There is also a weak trail of positive index change behind the pulse.

The third frame shows both the instantaneous response and the trail behind the pulse. The probe overlaps with the trailing edge of the pump near the exit face of the crystal and captures the instantaneous (Kerr) index change (the phase change near the right side in Fig 3.12c). There is a weak amplitude modulation that can be attributed to reconstruction errors. There is also a clearly visible trail of positive index change behind the pulse. The lifetime of the trail is longer than the time window of the experiment, about 3 picoseconds. A similar long-lasting index change also appeared in CS_2 through a delayed molecular Kerr response. However, it is not clear what the source of the delayed response is in $LiNbO_3$. Further experiments and theoretical modeling are necessary to resolve this issue. There is a gap between the regions of an instantaneous and long-lasting index change. This gap could

result from the pulse moving faster than it takes for the delayed response to grow, although we cannot discard the possibility that is due to reconstruction artifacts around the region of strong index change. The final frame (Fig. 3.12d) captures the trail after the pump has left the medium. The beam breaks up into multiple filaments inside the medium. The size of the filaments is 60-80 μm, which is close to the resolution limit of the system. The index change associated with the filaments is on the order of 10^{-4}, comparable to the index changes measured in water.

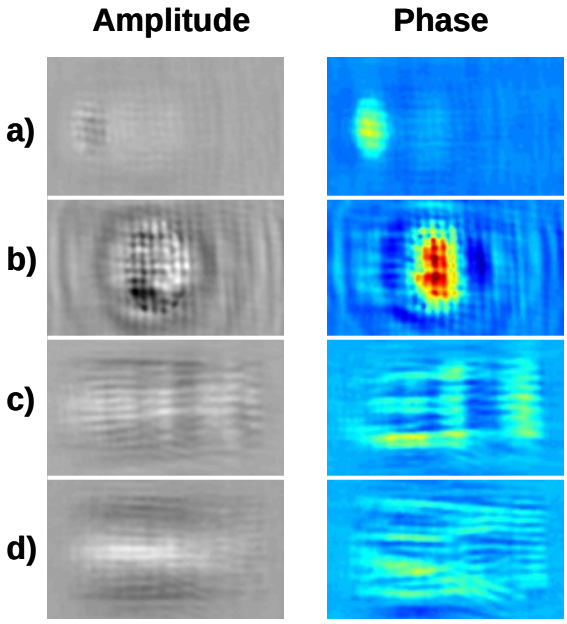

Figure 3.12. Holographic amplitude (left) and phase (right) reconstructions of femtosecond pulse propagation in a $LiNbO_3$ crystal. The maximum phase change in is 0.6 radians in (b). The relative time delay is (a) 0 ps, (b) 1.0 ps, (c) 2.0 ps and (d) 3.0 ps. Each sub-frame is 2.0 mm (horizontal) by 1.2 mm (vertical). The color scale is adjusted for the phase reconstructions in (c) and (d) to show more detail; the magnitude of the phase is increased by a factor of 1.3.

Single-shot capture is most useful when the beam profile is not repeatable. Figure 3.13 shows three different instances of pulse propagation captured with the same initial conditions. The figure shows the phase reconstructions for three laser shots. Each sequence (a,b,c) represents the propagation of a single laser pulse captured with the single-shot setup. The differences in the filamentation pattern are caused by shot-to-shot fluctuations in the laser energy and spatial profile. The qualitative behavior, however, is similar in the three experiments. The first two frames of each movie are very similar in all three instances. Some differences appear in the third and last frames where there are multiple filaments. Small changes in the initial conditions between experiments grow as the beam traverses the material and become apparent. In the previous examples of propagation in water and CS_2 we did not observe shot-to-shot differences, mainly due to the limited resolution. Changes become apparent when there is a lot of structure on the beam profile. In the case of $LiNbO_3$ the beam structure is large enough to be captured with the multiple-frame setup.

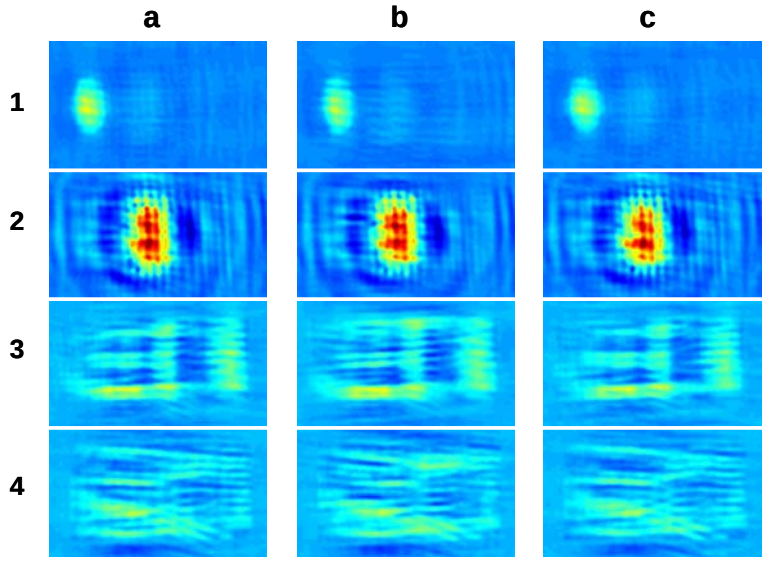

Figure 3.13. Shot-to-shot differences in the spatial pattern of a pulse in a $LiNbO_3$ crystal. Three time sequences (a-c) are captured under the same experimental conditions. Differences arise due to fluctuations in the laser pulse energy and beam profile. The frames of each sequence are labeled (1-4) and correspond to time delays of 0 ps, 1.0 ps, 2.0 ps and 3.0 ps. The color scale is adjusted for the phase

reconstructions in frames 3 and 4 to show more detail; the magnitude of the phase is increased by a factor of 1.3.

REFERENCES

[1] M. Centurion, Y. Pu, Z. W. Liu, et al., Optics Letters **29**, 772 (2004).

[2] A. Couairon, S. Tzortzakis, L. Berge, et al., Journal of the Optical Society of America B-Optical Physics **19**, 1117 (2002).

[3] R. Boyd, *Nonlinear optics* (Academic Press, San Diego, 2003).

[4] R. A. Ganeev, A. I. Ryasnyansky, M. Baba, et al., Applied Physics B-Lasers and Optics **78**, 433 (2004).

[5] P. K. Kennedy, IEEE Journal of Quantum Electronics **31**, 2241 (1995).

[6] L. V. Keldysh, Soviet Physics JETP-USSR **20**, 1307 (1965).

[7] M. Mlejnek, M. Kolesik, J. V. Moloney, et al., Physical Review Letters **83**, 2938 (1999).

[8] M. Centurion, Y. Pu, M. Tsang, et al., Physical Review A (2005).

[9] W. Liu, O. Kosareva, I. S. Golubtsov, et al., Applied Physics B-Lasers and Optics **76**, 215 (2003).

[10] P. K. Kennedy, S. A. Boppart, D. X. Hammer, et al., IEEE Journal of Quantum Electronics **31**, 2250 (1995).

[11] L. Berge and A. Couairon, Physical Review Letters **86**, 1003 (2001).

[12] S. Tzortzakis, L. Berge, A. Couairon, et al., Physical Review Letters **86**, 5470 (2001).

[13] R. L. Fork, C. V. Shank, C. Hirlimann, et al., Optics Letters **8**, 1 (1983).

[14] Q. Feng, J. V. Moloney, A. C. Newell, et al., IEEE Journal of Quantum Electronics **33**, 127 (1997).

[15] S. L. Chin, A. Brodeur, S. Petit, et al., Journal of Nonlinear Optical Physics & Materials **8**, 121 (1999).

[16] W. Liu, S. Petit, A. Becker, et al., Optics Communications **202**, 189 (2002).

[17] H. Hsieh, D. Psaltis, O. Beyer, et al., Optics Letters (2005).

Chapter 4

DYNAMICS OF FILAMENT FORMATION IN A KERR MEDIUM

4.1. INTRODUCTION

In this chapter we present a study of the large scale beam break up and filamentation of femtosecond pulses in a Kerr medium. We have experimentally monitored the formation of stable light filaments, conical emission and interactions between filaments. Three major stages lead to the formation of stable light filaments: First the beam breaks up into a pattern of connected lines (constellation), then filaments form on the constellations and finally the filaments release a fraction of their energy through conical emission. We observed a phase transition to a faster filamentation rate at the onset of conical emission. We attribute this to the interaction of conical emissions with the constellation, which creates additional filaments. Numerical simulations show good agreement with the experimental results.

The formation of optical filaments when high power laser pulses propagate in Kerr media has generated widespread interest since the phenomena was first observed [1-3]. When the laser power is much higher than the critical power for self focusing, an initially uniform beam breaks up into small filaments [4, 5]. Recently, the break up of high power femtosecond pulses in air into multiple filaments was reported [6]. The formation of small scale filaments has also been observed in glass [7]. Here we present an extensive study of large scale beam filamentation of femtosecond pulses in carbon disulfide (CS_2). The spatial evolution of the beam was studied as a function of propagation distance and energy. We have observed three phases leading to the formation of steady state filaments (solitary waves [8, 9]). The three stages are constellation formation, filamentation and conical

emission. The mechanism for beam breakup is modulation instability of spatial modes [10, 11]. It has been shown that for multiple filamentation, the power trapped in each filament is constant and does not depend on the power of the input beam [4, 10]. Thus, the number of filaments is expected to increase linearly with input power.

We have observed a phase transition in the rate of filament formation with input power that we attribute to the observed conical emissions from individual filaments. We have observed such conical emissions from individual filaments in CS_2 lasting less than 2 ps typically when the filaments first approach their minimum diameter. The result is that a fraction of the energy trapped in the filament is released, while the central component continues to propagate with a broadened spectrum. Conical emissions similar to the ones we have observed were theoretically predicted by Luther et al. [12]. It is believed that conical emissions are also tied to temporal pulse splitting and spectral broadening [13-15] since they occur shortly after the filament nears collapse to a very small area. Conical emissions from individual filaments of a different physical origin were experimentally measured for nanosecond pulses propagating through atomic vapors [16] and femtosecond pulses propagating in air [17, 18]. In the experiment we describe in this paper, we were able to generate and track a large number of filaments (>100). This allowed us to measure the statistics of conical emissions and capture filament interactions such as spatial splitting and fusion [19-22]. Our experimental results are complemented with computer simulations of the spatial evolution of the beam and the propagation of single self-trapped filaments.

4.2. EXPERIMENTAL SETUP

A schematic diagram of the experimental setup is shown in Figure 4.1. The Ti:Sapphire amplified laser system generates 150-femtosecond pulses with a central wavelength of 800 nm at a repetition rate of 10 Hz. The maximum pulse energy was 2 mJ, with a shot-to-shot variation of 3%. The duration of the pulses is kept constant throughout the experiments, while the energy is adjusted as indicated. The beam profile was approximately Gaussian with a 5 mm full width at half maximum. CS_2 was chosen as the nonlinear material because

of its strong Kerr nonlinearity. A value of $n_2 = 3 \times 10^{-15}$ cm^2/W has previously been measured in CS_2 using femtosecond pulses [23]. A glass cuvette with a 10 mm path length is filled with CS_2. The nonlinear pulse propagation was monitored by imaging the beam profile for different input pulse energies and different propagation lengths.

The laser beam is redirected so that it propagates downward and into the glass cell. The liquid level in the cuvette determines the propagation length. A pair of magnets is used to adjust the liquid level in situ. One of the magnets lies inside the cell and can be controlled by moving the second magnet outside. The liquid level was adjusted from 5.5 mm to 8 mm by submerging or lifting the inside magnet, with a minimum step size of 0.25mm. It is very important to change the propagation length in situ as any changes in the beam profile or position of the cell can lead to different filamentation patterns. With our setup we are able to repeatedly generate the same patterns and identify and follow the propagation of individual filaments. The beam profile that forms at the bottom of the cell is imaged onto a high resolution CCD camera (Apogee AP32ME, 2184x1472 pixels, pixel size 6.8 µm). The image is magnified by a factor of 5 using a 5x microscope objective (NA = 0.1, focal length = 25.4 mm). The light is attenuated by a factor of 4×10^{-5} using a neutral density filter in front of the camera. The camera is triggered by the laser, and each image is obtained with a single laser pulse.

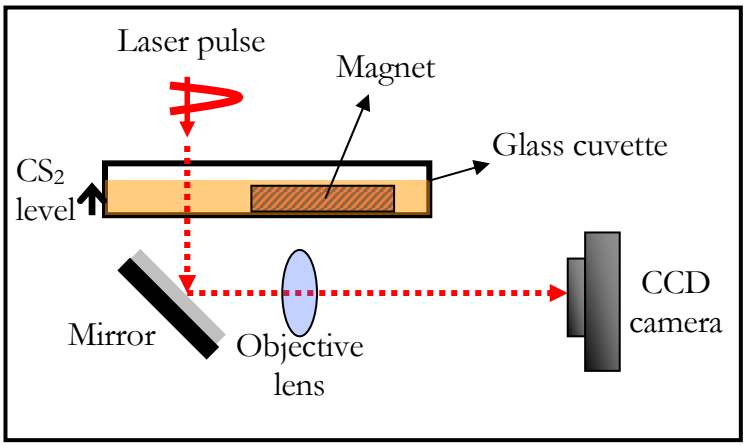

Figure 4.1: Experimental setup. A femtosecond pulse traverses a glass cell filled with carbon disulfide. The beam profile at the output of the cell is imaged on a CCD

camera. A magnet inside the cell is moved to adjust the liquid level, which determines the propagation distance.

4.3. CONSTELLATION FORMATION AND FILAMENTATION

4.3.1. Experimental results

As the beam propagates in the nonlinear medium we observed an initial formation of a pattern of connected lines (constellation). As the pulse propagates further, filaments form on the constellation. Figure 4.2 (a) shows a picture of the input beam profile. Figure 4.2 (b) shows the beam profile for a 0.78 mJ pulse after traversing 10 mm of CS_2. Figure 4.2 (c-d) shows the 2D Fourier transforms of the beam profile before and after the nonlinear interaction (the central component was blocked for visual clarity). The ring observed in the Fourier plane is due to the self-phase modulation of an extended beam propagating in a $\chi^{(3)}$ medium. The light is redirected preferentially in a particular direction, due to the phase matching condition necessary for efficient scattering. We will discuss this in detail in the following section.

Once the constellation is formed it remains stable as the beam continues to propagate (within our observation range), except for the appearance of an increasing number of bright spots (filaments). The width of the stripes in the constellation decreases until it reaches a minimum size of 15-20 μm, after which the width remains constant and the constellation continues to break up into filaments. The constellation remains unchanged as the pulse energy is increased from 0.5 mJ to 1.1 mJ. The only change we observed with increased pulse energy is the formation of additional filaments. The constellation pattern is very sensitive to the input beam profile. For example, the beam can be induced to form a constellation in a specified pattern. Figure 4.2 (e-f) shows the beam profile before and after the nonlinear propagation for a beam that was passed through a circular aperture to

generate diffraction rings. After traversing the CS_2 cell the beam breaks up in a circular pattern resembling that of the input beam.

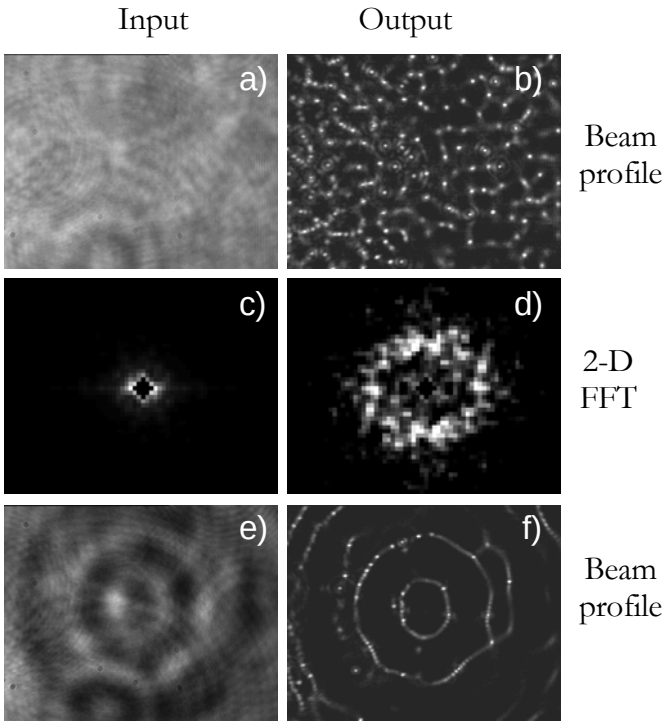

Figure 4.2. Beam profile and 2-D FFT before and after traversing 10 mm of CS_2. (a) Input beam profile. (b) Beam profile after traversing 10mm of CS2. (c) and (d) are the 2-D FFT of (a) and (b), respectively. (e) and (f) are the input and output beam profiles for a modulated beam.

Figure 4.3 shows the evolution of the beam with propagation distance for four different energy levels (0.70 mJ (a), 0.86 mJ (b), 1.0 mJ (c) and 1.1 mJ (d)). A fraction of the output beam profile (0.5 mm x 0.5 mm) is shown for propagation distances of 5.5 mm, 6.3 mm, 7.2 mm and 8.0 mm. The input beam profile (Fig. 4.3 (a)) is kept constant throughout the experiment. The number of filaments is seen to increase both with energy and propagation distance, while the constellation remains fixed. Most of the filaments are stable, and once they are formed they survive as the propagation length or energy is increased (within the limits of the experiment). The filaments propagate with a stable diameter of 11.8 ± 2.6 μm (FWHM) for at least 3 mm. When the density of filaments becomes high, interactions

between the filaments cause the whole pattern to become unstable (it changes drastically from shot-to-shot even if input parameters are the same).

For an input energy of 0.70 mJ (Fig. 4.3 (a)), at a propagation distance of 5.5 mm the constellation has already formed but no filaments are observed. As the pulse continues to propagate filaments start to appear in increasing number within the constellation. After the filaments reach a minimum size, conical emissions can be observed as a ring around the filaments (Fig. 4.3 (c-d), z = 8 mm). We have also observed spatial splitting and fusion of filaments (see section 4.5). It is interesting to note that the effects of increasing the energy or the propagation length are similar. It is possible to find images across Fig. 4.3 with different energy and propagation distance with roughly the same number of filaments, for example E = 0.70 mJ, d =7.2 mm and E = 0.86 mJ , d = 6.3 mm . The similarity is due to the fact that increasing the energy speeds up the self focusing process that generates the filaments. This is only expected to hold for some range of energies and distances. For longer propagation distance we have observed the number of filaments to reach saturation and eventually start to decrease.

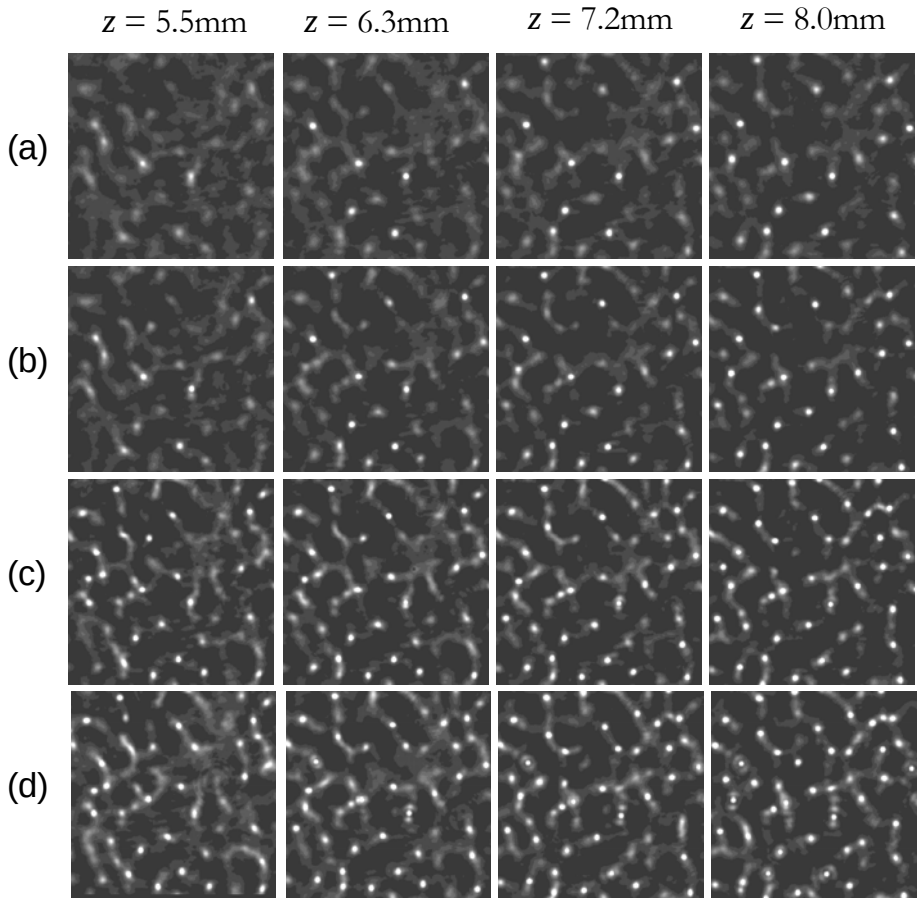

Figure 4.3. Beam breakup and filamentation as a function of propagation distance (left to right) and energy (top to bottom). (a) E = 0.70 mJ, (b) E = 0.86 mJ, (c) E = 1.0mJ and (d) E = 1.1 mJ. The size of each image is 0.5mm x 0.5mm.

The Kerr effect (n_2) and diffraction alone cannot generate stable light filaments. Another nonlinearity must act to stop the self focusing. The size of the filaments is an indication of the strength of this nonlinearity. It is known that the addition of a saturation mechanism in the third order nonlinearity such as fifth order nonlinearity will generate stable filaments [24]. We have included a negative n_4 (fifth order nonlinearity) in our simulations and seen good agreement between simulations and experiments.

4.3.2. Numerical results and discussion

We will first discuss the formation of the constellations. The dominant spatial frequency of the constellations (the diameter of the ring in Fig. 4.2 (d)) is determined by a nonlinear phase matching condition [10] and the input beam profile. As a way to illustrate the phase matching condition, assume we start with a uniform pump beam propagating through a Kerr medium, with a small fraction of the beam energy being scattered in all directions. The presence of the nonlinear index change will cause the strong pump beam to be phase matched to waves scattered at a specific angle. Assuming the pump beam remains undepleted, one can derive a simple relation for the transverse wave-vector with the maximum nonlinear gain [10]:

$$q = k\sqrt{\frac{2n_2 I}{n_0}} \tag{4.1}$$

where q is the transverse wave-vector, I is the intensity of the beam, n_0 the index of refraction of the material and n_2 the Kerr coefficient.

The phase matching condition depends on the intensity of the beam. However, in our experiments the constellations did not change as the energy was increased. We believe there are two reasons for this discrepancy. First, in the experiments the input beam was not entirely smooth. Therefore, a spatial frequency initially dominant in the beam will be amplified the most, and a small change in the gain spectrum (through a small change in the intensity) will not necessarily result in a different constellation. A similar result was reported by Abbi et al. [25] where they showed that for a small number of filaments, the position of the filaments at the output was correlated to weak modulation of an approximately uniform input beam. The second reason is that the phase matching condition exists only when there is a well-defined (undepleted) pump beam. For higher intensity levels the beam quickly breaks up and the phase matching condition no longer holds.

After the constellations are formed, the self-focusing process acts locally to break up the constellation lines into self-trapped light filaments (hot spots). Filaments form at the local

maxima of the intensity distribution in the constellation. The formation and propagation of the filaments are discussed in detail in the following sections. We now compare the experimental results with a numerical simulation.

A complete simulation of the spatial and temporal profile of the nonlinear pulse propagation requires very fine sampling in three spatial dimensions and time. The light propagation is calculated assuming a scalar envelope for the electric field, which is slowly varying in time and along the propagation direction z. The evolution of the scalar envelope is given by the equation (the derivation of this equation is shown in Appendix A):

$$\frac{\partial A}{\partial z} = \frac{i}{2kn_0}\left(\frac{\partial^2}{\partial x^2} + \frac{\partial^2}{\partial y^2}\right)A + ik\left(n_2|A|^2\right)A + ik\left(n_4|A|^4\right)A - \frac{i\beta_2}{2}\frac{\partial^2 A}{\partial T^2} \tag{4.2}$$

$A(x,y,z,T)$ is the complex envelope of the electric field, $k = 2\pi/\lambda$, $\lambda = 800\text{nm}$, $n_0 = 1.6$, $n_2 = 3 \times 10^{-15}$ cm^2/W [23], $n_4 = -2 \times 10^{-27}$cm^4/W^2, $\beta_2 = 200$ps^2/km [26], and T is the time measured in the reference frame moving at the group velocity of the pulse. The first term on the right-hand side accounts for diffraction, the second is Kerr self focusing (third order nonlinearity), the third term accounts for the fifth order nonlinearity and the last term accounts for dispersion. A linear absorption term was not included because CS2 is highly transparent at 800 nm, no intensity changes were measured for a propagation distance of 10 mm. Two-photon absorption has been measured in CS2 with a value of (4.5 ± 1) x 10-13 cm/W [27]. We have tried including this term in the simulation and did not see any significant changes in the output.

Previous simulations of femtosecond pulse propagation through different materials have included plasma generation as a mechanism to arrest the collapse of the optical filaments [17, 28-30]. The high intensity of the pulses causes ionization of the material and the generated electron plasma contributes a negative index change that balances the positive index change due to the Kerr effect. In our experiments the intensity of the filaments is not sufficient to ionize the material. To verify this we have calculated, following the Keldysh method [31, 32], the intensity threshold for breakdown in CS_2 to be 2×10^{13} W/cm^2 (the ionization energy of CS_2 is 10.08 eV [33]). This calculation method has been previously

compared with experimental results for a wide range of parameters, and it was shown to be accurate within a factor of two [34, 35]. Using the CCD camera, we have measured the energy trapped in the filaments to be (0.1 ± 0.04) μJ. For the measured energy, the measured filament size, and a pulse duration of 150 femtoseconds, the intensity of the filaments is (5.9 ± 2.4) x 10^{11} W/cm^2, which is more than 30 times smaller than the calculated breakdown threshold. This justifies our conclusion that plasma generation does not play a significant role in the propagation through CS_2. It has been shown that including non-paraxial effects in the simulation can also prevent the collapse of the filaments [36]. However, non-paraxiality becomes significant only when the diameter of the filaments approaches the wavelength and we have measured a minimum filament diameter of approximately 12 μm, 15 times larger than the wavelength. We have included the fifth order term in the nonlinear polarization (n_4) as the only logical remaining mechanism to balance the self-focusing and generate stable light filaments. We were not able to find published measurements of the value of n_4, and therefore we used in the simulations the value that gave us the best match with experiment.

Instead of calculating the full temporal and spatial evolution of the light field, we have used a simpler model that captures the spatial evolution of the beam, where we assume that the temporal profile of the pulse remains constant:

$$\frac{dA}{dz} = \frac{i}{2kn_0}\left(\frac{\partial^2}{\partial x^2} + \frac{\partial^2}{\partial y^2}\right)A + ik\left(n_2|A|^2\right)A - ik\left(n_4|A|^4\right)A \tag{4.3}$$

In this case A(x,y,z) is a function of the spatial coordinates only. The fifth order nonlinearity is introduced to generate stable light filaments, as observed in the experiments. The equation is solved using the Split-step Fourier method [37]. In these experiments the changes in the temporal profile of the pulse do not play a major role in the spatial evolution of the beam. We have simulated the propagation of a single filament including the temporal profile and seen that the pulse duration does not change significantly for the experimental propagation distance (see Section 4.5.2).

The intensity distribution of the beam before traversing the nonlinear material was captured using a CCD camera (Fig. 4.4(a)). The square root of the laser beam profile captured on the CCD camera was used as the amplitude of the input light field for the simulation. The phase of the input light was assumed to be spatially uniform. In the experiment, a pulse (0.8mJ, 150 femtoseconds, 5 mm FWHM) propagates in CS_2 for a distance of 8 mm. The simulation is run for the same intensity and propagation length as in the experiment. Figure 4.4 shows a comparison of the experimental and numerical results. The simulated beam also breaks up into constellations and filaments similar to those observed in the experiment. The simulation does not reproduce the experimental results exactly, i.e., the positions of the filaments are different. This is due to the lack of phase information of the input beam profile and possibly due to other nonlinearities not included in the simulation. However, the simulation clearly captures the main features of the propagation phenomena.

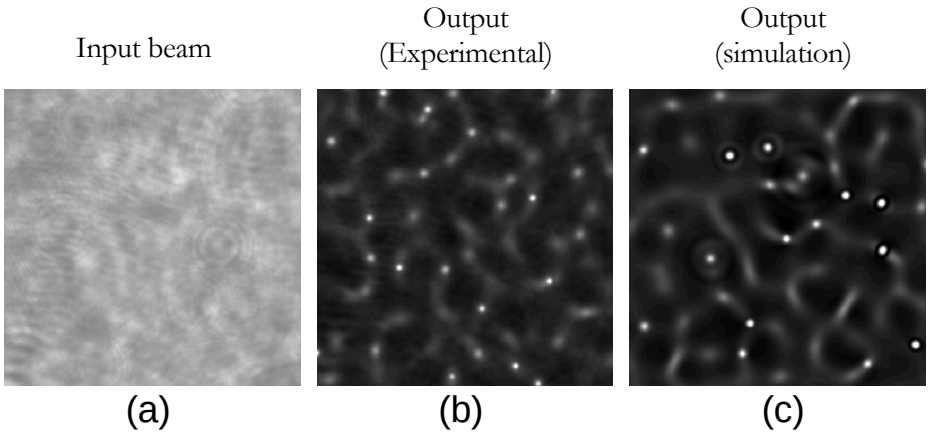

Figure 4.4. Comparison of experimental and numerical results. The amplitude of the input beam (a) was measured and used as the input of the numerical simulation. There is good agreement between the experimental (b) and simulated output beam profile (c). The images are 0.5 mm x 0.5 mm.

Even though the constellation pattern depends on the input beam profile, the formation of a constellation does not require a specific spatial modulation of the input. It has been shown theoretically that any amplitude perturbation of the input light will cause the beam to break up [4]. In order to demonstrate this and study the dependence of the constellation pattern on

the intensity of the input beam, we have simulated the propagation of a Gaussian beam with random noise in its amplitude. Spatially random noise is generated on the computer and superimposed on the amplitude of the input beam. The standard deviation of the noise pattern is 3% of the beam amplitude. Fig. 4.5 shows the simulation results for a beam with an initial intensity of 3.1 x 10^{10} W/cm^2 and a beam diameter of 1.6 mm. After propagating for 6 mm some weak amplitude modulation is observed as the constellations start to form (Fig. 5 (b)). From 6 mm to 10 mm (Fig. 4.5 (c-d)) more light is focused in the constellation, and the background level is reduced. Only at a propagation distance of 12 mm (Fig. 4.5 (e)) do filaments start to appear, as opposed to 8 mm when the experimental beam profile is used as the input. This simulation shows that the constellation can grow out of an input with only random noise. We repeated this simulation for different values of the input intensity and saw an increase in the spatial frequency of the constellations with input beam intensity for intensities below 2 x 10^{10} W/cm^2. In this case the constellations grew out of random noise, so the dominant spatial frequency was determined only by the nonlinear phase matching condition. However, as the power was increased above this value the beam was rapidly depleted, leading to a breakdown of the phase matching condition and an earlier transition to the filament formation process.

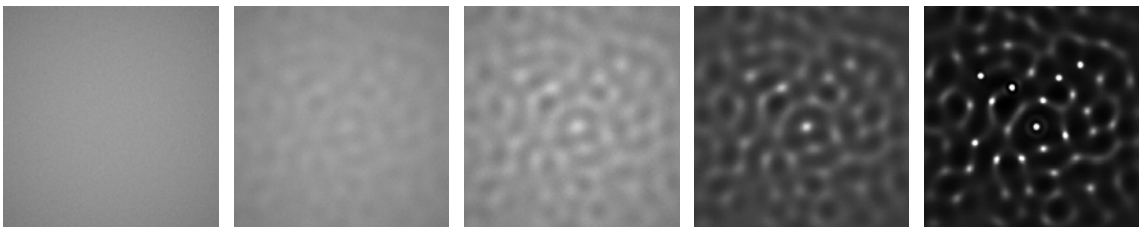

Figure 4.5: Numerical simulation of beam propagation. A constellation and filaments are generated from an input beam with random amplitude noise. The images show the beam profile for propagation distances of 0 mm, 6 mm, 8 mm, 10 mm and 12 mm.

4.4. PHASE TRANSITION IN THE RATE OF FILAMENTATION AS A FUNCTION OF INPUT ENERGY

Figure 4.6 (a) shows a plot of the number of filaments as a function of input power for a propagation distance of 10mm. There are two transition points in the rate of filament formation. For low energies no filaments are observed. As the energy increases at some point filaments begin to appear. The filamentation length depends on both the energy and the beam profile. A beam with strong modulation will break up into filaments faster, while a higher intensity will also cause the beam to break up in a shorter propagation distance. For the given beam profile, the first transition occurs when the energy is high enough for filamentation to occur in less than 10 mm.

In the second transition we see a change in the filamentation rate (a change in the slope in Fig. 4.6 (a)) when the input pulse energy reaches 0.5 mJ. We carried out multiple experiments with different random input profiles. The transition to a faster filamentation rate was observed in all cases. The filamentation rate increased by a factor between 2 to 3, and the transition pulse energy was approximately the same in all cases. The transition happens when most of the filaments have reached their minimum diameter and maximum intensity. The mean filament size (Fig. 4.6 (b)) reaches a minimum diameter of about 12 μm at the transition point, while the intensity reaches a maximum near the transition (Fig. 6 (c)). The energy trapped in each filament is (0.1 ± 0.04) μJ. Figure 4.6 (a) also shows the number of conical waves we observed as a function of pulse energy, and it clearly shows that the onset of the conical emissions coincides with the phase transition in the filamentation rate. We conclude that the conical emissions are at least partially responsible for the phase transition. During the first stage of filamentation, most of the filaments are still focusing. As the input intensity is increased, filaments release their excess energy through conical emissions before they can propagate as stable solitary waves. The radiated conical waves interfere with the background constellation and seed the generation of new filaments that appear at the intersection of the conical waves with the constellation (Figure 4.7).

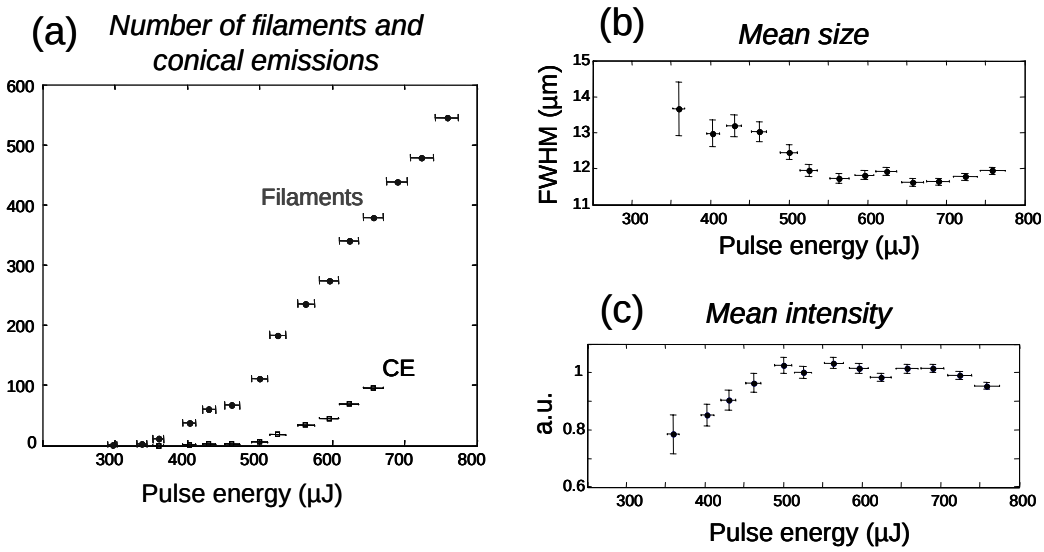

Figure 4.6. Filament statistics as a function of input pulse energy. (a) Number of filaments and conical emissions (CE). (b) Mean size. (c) Mean intensity. A transition in the filamentation rate is observed at 0.5mJ.

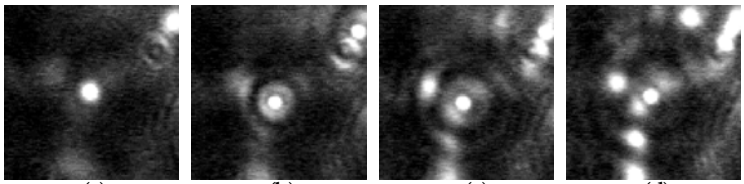

Figure 4.7. Conical emission and seeding of new filaments. (a) For an input energy of 0.54 mJ a single filament is observed. (b) When the energy is increased to 0.64 mJ the filament emits conical waves before reaching the output face of the nonlinear material. (c-d) For higher pulse energies of 0.74 mJ (c) and 0.86 mJ (d), new filaments are formed at the intersection of the conical emission.

4.5. CONICAL EMISSION, FILAMENT SPATIAL SPLITTING AND FUSION

4.5.1. Experimental results

Figure 4.8 (a) shows an example of conical emission for four different propagation distances at a fixed pulse energy. The filament survives and continues to propagate after the conical emission. The peak intensity is reduced by 30-50%. The emission is not a continuous process. From our observations we estimate the duration of the emission to be less than 1.5 picoseconds. Multiple conical emission was also observed in the form of a pair of rings around the filaments.

We have also measured the spectral bandwidth of the filaments before and after the conical emission. The Kerr nonlinearity causes the spectrum of the filaments to broaden as they traverse the material. We did not observe spectral broadening of the light in the constellation that is not trapped in a filament. The intensity level of the constellation is not sufficiently high to significantly broaden the spectrum of the pulse. The collapse leading to conical emission causes a sudden change in the spectrum of the filament. We deduced this by measuring the spectral content of the filaments before and after conical emissions. Specifically, the filaments were imaged onto the CCD using a bandpass filter with peak transmission of 60% at 805 nm and 34 nm FWHM. The spectrum of the pulses coming out of the laser is approximately Gaussian centered at 800 nm with a FWHM of 7 nm. Before the conical emission, the filter transmits 45% of the light trapped in the filaments. After the conical emission, the spectrum of the filament broadens and only 15% of the light is transmitted by the filter. In contrast, the spectrum of the conical waves did not broaden and was similar to that of the filaments before the conical emission. We will offer an explanation to this phenomenon in the following section.

We have observed interactions between the filaments in the form of fusion of two filaments (Fig. 4.8 (b)) and the splitting of a single filament in two (Fig. 4.8 (c)). We believe the fusion is due to an attractive force, which exists if the two filaments are in phase. We

attribute the splitting to filaments having excess energy and an asymmetric spatial profile. We have also observed two filaments merging and then immediately radiating (Fig. 4.8 (d)) and filaments splitting into more than two new filaments.

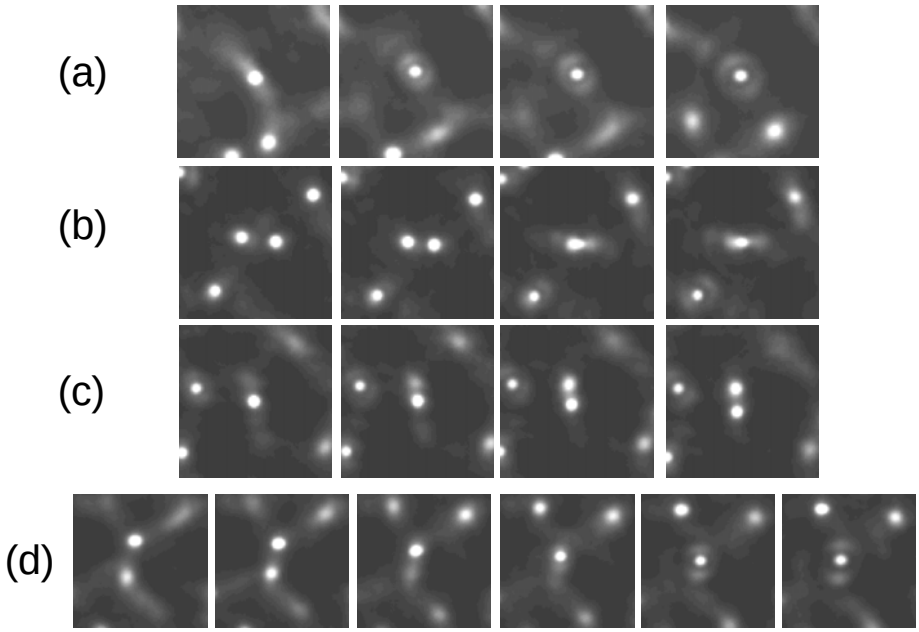

Figure 4.8. Behavior of individual filaments. (a) Experimental observation of conical emission. (b) Fusion of two filaments. (c) Splitting. (d) Fusion followed by conical emission. The step in propagation distance is 0.50 mm for (a) and 0.25 mm for (b), (c) and (d).

4.5.2. Numerical results and discussion

We have numerically calculated the propagation of a single filament including both the spatial and temporal profile of the pulse. We use a model that assumes the spatial profile of the filament is circularly symmetric:

$$\frac{\partial A}{\partial z} = \frac{i}{2kn_0}\frac{1}{r}\frac{\partial}{\partial r}\left(r\frac{\partial A}{\partial r}\right) + ik\left(n_2|A|^2\right)A + ik\left(n_4|A|^4\right)A - \frac{j\beta_2}{2}\frac{\partial^2 A}{\partial T^2} \tag{4.4}$$

where *A(r,z,T)* is a function of r, z and time and r is measured from the center of the filament (in cylindrical coordinates).

We have simulated the propagation of a transform-limited pulse with a pulse width of 150 femtoseconds (FWHM) for a distance of 4 mm. The initial spatial profile is Gaussian with a FWHM of 30 um and power P = 8 P_{cr}. The input pulse is of the form:

$$A(z=0,r,T)=\sqrt{I_0}\,Exp\left(\frac{-r^2}{w_0^2}\right)\mathrm{sech}\left(\frac{\mathrm{T}}{\mathrm{T}_0}\right) \tag{4.5}$$

The critical power is given by:

$$P_{cr}=\frac{\pi(0.61)^2\lambda^2}{8n_0n_2}=1.9\times10^5 W \tag{4.6}$$

A large input power was necessary to observe the conical emission. The pulse self-focuses into a filament and emits conical radiation after propagating for 1.5 mm. The duration of the pulse does not change significantly during the propagation. The simulation shows that the pulse width at the center of the filament varies between 100 femtoseconds and 200 femtoseconds over a propagation distance of 4 mm, while the spatially averaged pulse width increases monotonically from 150 femtoseconds to 190 femtoseconds. The spectrum of the pulse, however, is observed to broaden significantly. The spectral bandwidth of the filament (the central part of the beam) increases from 2 THz to 10 THz after 2 mm (right after the conical emission) and to 15 THz after propagating for a total distance of 4 mm. The spectral bandwidth of the conical emission does not broaden and remains similar to the initial filament spectrum, in agreement with the experimental results obtained with the bandpass filter. The observed conical emission was, however, weaker than that observed experimentally. We believe this difference can be accounted for by the presence of the constellation and background light around the filaments. The fact that the temporal profile of the pulse does not change significantly allows us to study the conical emission in more detail, ignoring spectral broadening and dispersion using the beam propagation model to numerically evaluate Equation 4.3.

Before the filaments reach a steady state, the focusing is stronger for the central (brighter) part of the filament. As the filament nears its minimum radius, the outer part of the light distribution cannot keep up with the focusing and starts to diffract. We believe this is the mechanism that generates the observed conical emission rather than modulation instability. This explanation is consistent with the observed spectral composition of the beam following a conical emission. The outer part of the beam was less intense since it was not tightly focused, and the spectrum was not broadened.

We have also observed in our numerical simulations an increase in the strength of the conical emission in the presence of background light. When the filament is surrounded by a uniform light distribution, the conical emission is amplified and multiple rings can be observed. We attribute this to the filaments taking in energy from the background during the self focusing stages. This increases the amount of energy in the tails of the filament spatial distribution, which is then released through the conical emission. If the filament contains enough energy multiple rings can be generated from different parts of the spatial profile.

Simulations for a single filament show a periodic re-focusing (soliton breathing [38]). We have numerically solved equation 4.3 to simulate the periodic focusing of a single filament (Fig. 4.9). The input beam has a Gaussian spatial profile with a 64 μm diameter and power equal to 5 times the critical power. Figure 9 shows the filament reaching a minimum size, defocusing and then focusing again. We did not observe this breathing behavior experimentally. In order to explain this we carried out a simulation in which the filament is surrounded by a constellation. As the input to the simulation we used a uniform beam with an intensity of 3×10^{10} W/cm^2 and 3% random amplitude noise. The noise is added to induce the beam to break up into a constellation. A Gaussian peak with a diameter of 64 μm and an intensity 10% higher than the background was added to induce the formation of a filament at the center. Figure 10 shows the output beam profile for propagation distances from 7.5 mm to 11 mm. A filament appears at the center after 8 mm (Fig. 4.10 (b)) surrounded by a constellation. The filament then emits conical waves that interfere with the constellation to seed new filaments (Fig. 4.10 (c-e)). Finally the original filament fuses with one of the new filaments (Fig. 4.10 (d-h)). In this case the periodic re-focusing is not

observed since the presence of the constellation breaks the symmetry. The breathing behavior can be thought of as a periodic failed attempt at a conical emission. The presence of the background constellation modifies this behavior when the emitted light constructively interferes with the constellation and induces the generation of new filaments. The new filaments also affect the propagation of the original filament.

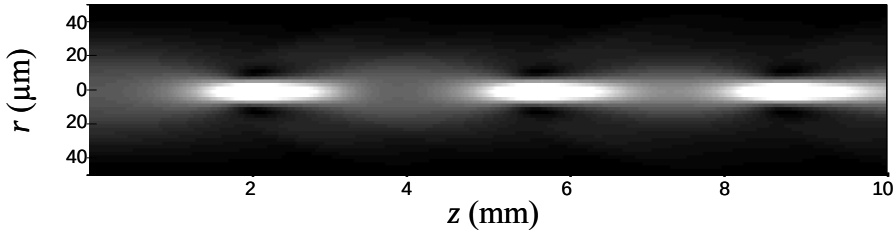

Figure 4.9. Simulation of the propagation of a single filament over 10 mm. The intensity of the filament is plotted as a function of radius (vertical scale) and propagation distance (horizontal scale). The filament is observed to periodically re-focus.

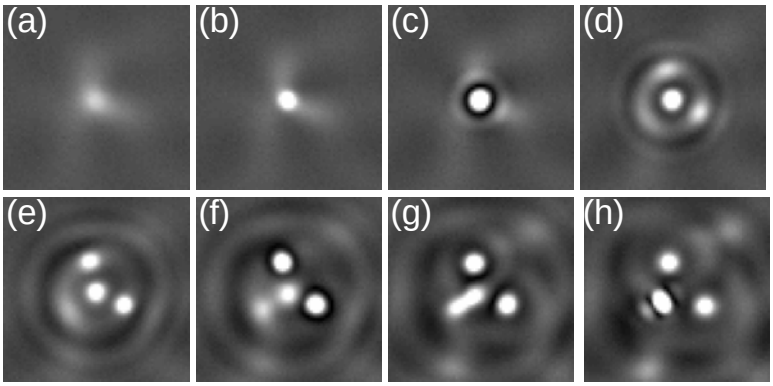

Figure 4.10. Simulated filament propagation in the presence of a noisy background. (a-c) The filament focuses and emits conical waves. (d-e) The conical waves seed the formation of new filaments on the constellation. (f-h) The original filament is

attracted and fuses with a new filament. The propagation distance from (a) through (h) is from 7.5 mm to 11 mm in steps of 0.5 mm.

4.6. SUMMARY

We have studied in detail the filamentation process in CS_2, and we have identified a number of interesting behaviors. The formation of a constellation precedes the filamentation stage. We have observed a unique form of conical emission that appears to be the dominant mechanism for filaments with excess energy to relax to their steady state level. We have also observed a phase transition in the filamentation rate at the onset of conical emission from the filaments. We attribute the change in the filamentation rate to interactions between the constellation and the conical emissions. The spectral bandwidth of the filaments was observed to increase after conical emission, while the spectrum of the conical waves did not broaden. Finally we observed fusing and splitting of filaments both experimentally and numerically.

REFERENCES

[1] F. Shimizu, Physical Review Letters 19, 1097 (1967).

[2] R. R. Alfano and S. L. Shapiro, Physical Review Letters 24, 592 (1970).

[3] A. J. Campillo, S. L. Shapiro, and B. R. Suydam, Applied Physics Letters 23, 628 (1973).

[4] V. I. Bespalov and V. I. Talanov, Jetp Letters-Ussr 3, 307 (1966).

[5] A. J. Campillo, S. L. Shapiro, and B. R. Suydam, Applied Physics Letters 24, 178 (1974).

[6] L. Berge, S. Skupin, F. Lederer, et al., Physical Review Letters 92 (2004).

[7] X. H. Ni, C. Wang, X. C. Liang, et al., IEEE Journal of Selected Topics in Quantum Electronics 10, 1229 (2004).

[8] A. Barthelemy, S. Maneuf, and C. Froehly, Optics Communications 55, 201 (1985).

[9] M. Segev, B. Crosignani, A. Yariv, et al., Physical Review Letters 68, 923 (1992).

[10] R. Boyd, Nonlinear optics (Academic Press, San Diego, 2003).

[11] M. Saffman, G. McCarthy, and W. Krolikowski, Journal of Optics B-Quantum and Semiclassical Optics 6, S397 (2004).

[12] G. G. Luther, A. C. Newell, J. V. Moloney, et al., Optics Letters 19, 789 (1994).

[13] G. G. Luther, J. V. Moloney, A. C. Newell, et al., Optics Letters 19, 862 (1994).

[14] J. K. Ranka, R. W. Schirmer, and A. L. Gaeta, Physical Review Letters 77, 3783 (1996).

[15] A. Brodeur and S. L. Chin, Journal of the Optical Society of America B-Optical Physics 16, 637 (1999).

[16] B. D. Paul, M. L. Dowell, A. Gallagher, et al., Physical Review A 59, 4784 (1999).

[17] E. T. J. Nibbering, P. F. Curley, G. Grillon, et al., Optics Letters 21, 62 (1996).

[18] O. G. Kosareva, V. P. Kandidov, A. Brodeur, et al., Optics Letters 22, 1332 (1997).

[19] J. P. Gordon, Optics Letters 8, 596 (1983).

[20] G. I. Stegeman and M. Segev, Science 286, 1518 (1999).

[21] M. Shalaby, F. Reynaud, and A. Barthelemy, Optics Letters 17, 778 (1992).

[22] H. Schroeder and S. L. Chin, Optics Communications 234, 399 (2004).

[23] R. A. Ganeev, A. I. Ryasnyansky, M. Baba, et al., Applied Physics B-Lasers and Optics 78, 433 (2004).

[24] A. Piekara, IEEE Journal of Quantum Electronics QE 2, 249 (1966).

[25] S. C. Abbi and H. Mahr, Physical Review Letters 26, 604 (1971).

[26] A. Samoc, Journal of Applied Physics 94, 6167 (2003).

[27] M. Falconieri and G. Salvetti, Applied Physics B-Lasers and Optics 69, 133 (1999).

[28] K. Ishikawa, H. Kumagai, and K. Midorikawa, Physical Review E 66 (2002).

[29] C. Courtois, A. Couairon, B. Cros, et al., Physics of Plasmas 8, 3445 (2001).

[30] N. Akozbek, C. M. Bowden, A. Talebpour, et al., Physical Review E 61, 4540 (2000).

[31] L. V. Keldysh, Soviet Physics JETP-USSR 20, 1307 (1965).

[32] P. K. Kennedy, IEEE Journal of Quantum Electronics 31, 2241 (1995).

[33] C. P. Safvan, V. R. Bhardwaj, G. R. Kumar, et al., Journal of Physics B-Atomic Molecular and Optical Physics 29, 3135 (1996).

[34] P. K. Kennedy, S. A. Boppart, D. X. Hammer, et al., IEEE Journal of Quantum Electronics 31, 2250 (1995).

[35] Q. Feng, J. V. Moloney, A. C. Newell, et al., IEEE Journal of Quantum Electronics 33, 127 (1997).

[36] G. Fibich, Physical Review Letters 76, 4356 (1996).

[37] G. P. Agrawal, Nonlinear fiber optics (Academic Press, San Diego, 1995).

[38] D. E. Pelinovsky, V. V. Afanasjev, and Y. S. Kivshar, Physical Review E 53, 1940 (1996).

Chapter 5

SELF-ORGANIZATION OF SPATIAL SOLITONS

5.1. INTRODUCTION

In this chapter we present experimental results on the self-organization of spatial solitons in a self-focusing nonlinear medium. We have observed the emergence of order, self organization and a transition to a chaotic state. Nonlinear interactions between light and matter can lead to the formation of spatial patterns and self-trapped optical beams. Modulation instability is responsible for the spontaneous formation of optical patterns, which have been observed both with coherent and incoherent light [1,2]. Under certain conditions, self-trapped optical beams (spatial solitons) can be generated through the interplay between diffraction and nonlinear effects [3-5]. Self-trapped light filaments have been observed in materials with quadratic [6] and cubic [7] (Kerr) optical nonlinearities. Spatial solitons can interact through collisions [8,9], which opens the possibility of using them to perform computations [10]. Optical filaments can also act as waveguides, and it was recently shown that in liquid crystals they can be steered using an applied voltage [11]. Applications involving the use of spatial solitons will most likely require large numbers of them; however, the effects of the interactions between large numbers of filaments remain largely unexplored. Here we report the observation of self-organization of spatial solitons into a periodic array and the later breakdown of the periodicity. The array initially forms with a period that depends on the intensity of the illuminating beam. If the filaments are formed too closely they rearrange themselves into an array with a larger more stable period. This result has implications for the density with which solitons can be packed both for information processing and communication applications.

A light pulse propagating in a nonlinear Kerr medium will come to a focus if its power is above a critical value. If the pulse power is much higher than the critical power then the optical beam will break up into multiple filaments [12-14]. Each filament will contain approximately the critical power, defined as [15]:

$$P_{cr} = \frac{\pi(0.61)^2 \lambda^2}{8 n_0 n_2}. \tag{5.1}$$

where λ is the laser wavelength in vacuum, n_0 is the linear refractive index of the material and n_2 is the material constant that gives the strength of the Kerr nonlinearity in units of inverse light intensity. We have used carbon disulfide as the nonlinear material (n_0 = 1.6, n_2 = $3 \times 10^{-15} cm^2/W$ [16]), which has a critical power of 190 kW for our laser wavelength of 800 nm.

5.2 EXPERIMENTAL SETUP

The experimental setup is shown in Figure 5.1. A Ti:Sapphire laser amplifier system is used to generate 150-femtosecond pulses with a maximum energy of 2 mJ. The standard deviation in laser pulse energy from shot-to-shot is 3%. The laser is run at the maximum energy level to achieve maximum stability, and neutral density filters are used to adjust the pulse energy in the experiment. Each pulse from the laser is split into pump and probe pulses. The pump pulse propagates through a 10 mm glass cell filled with carbon disulfide (CS_2). The beam profile of the pump at the exit of the glass cell is imaged onto a CCD camera (CCD 1) with a magnification factor of 5. A cylindrical lens (focal length = 10 cm) focuses the pump beam into a line approximately 3 mm inside the medium. The line focus generates a single column of filaments. We studied the filamentation process using Femtosecond Time-resolved Optical Polarigraphy (FTOP) [17]. This technique uses the transient birefringence induced in the material through the Kerr effect to capture the beam profile. The probe pulse propagates in a direction perpendicular to the pump. The presence of the pump induces a transient birefringence proportional to the intensity of the pulse. The

trajectory of the pump pulse can be captured with high temporal resolution by monitoring the probe pulse through cross polarizers. In our experimental setup (Fig. 5.1), the pump is polarized in the vertical direction and the probe is polarized at 45 degrees with respect to the pump's polarization. After the probe traverses the nonlinear medium it goes through an analyzer (polarizer at -45 degrees) and is imaged on a second CCD camera (CCD 2) with a magnification factor of 6. Light from the probe reaches the detector only if the probe temporally and spatially overlaps with the pump inside the nonlinear material. A delay line is used to synchronize the arrival of pump and probe pulses, and allows us to observe the pump at different positions along the direction of propagation.

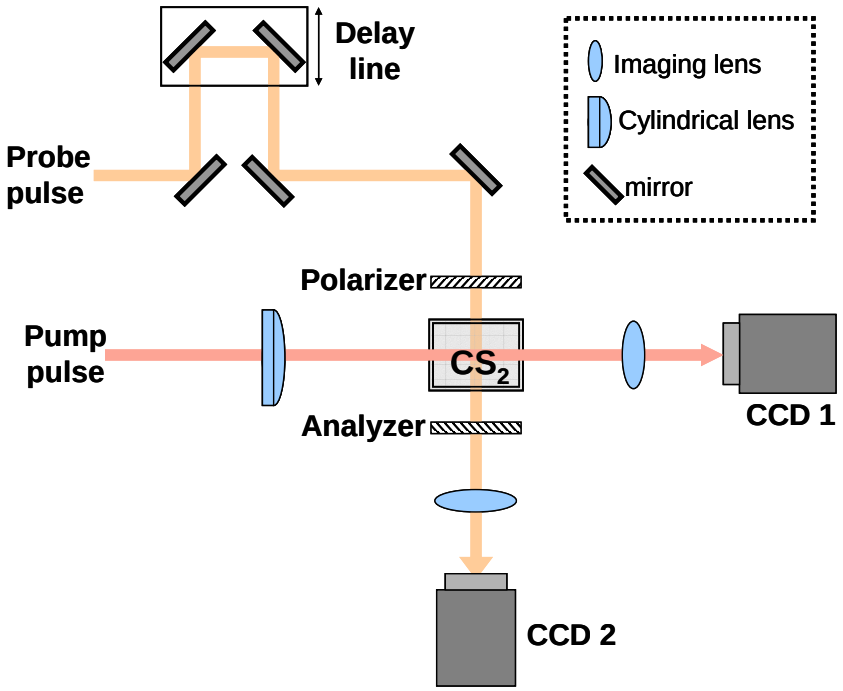

Figure 5.1. FTOP setup. The pump pulse is focused in the material with a cylindrical lens to generate a single column of filaments. The beam profile at the output is imaged on CCD 1. The probe pulse goes through a variable delay line, a polarizer and analyzer and is imaged on CCD.

5.3. EXPERIMENTAL RESULTS

5.3.1. Beam profile and instabilities as a function of pulse energy

Figure 5.2 shows the beam profile of the pump beam at the output of the CS_2 cell (CCD 1 in Fig. 1) as a function of pump pulse power. In the absence of nonlinearity the incident cylindrical beam would diverge to a width of 200 μm as it propagates to the output surface. For a pulse power equal to 12 times the critical power ($P = 12\ P_{cr}$, Fig. 5.2a), self focusing and diffraction nearly balance each other, and the output beam width is approximately the same as for the input. For higher pulse power the beam self focuses into an increasingly thinner line (Figs. 5.2b and 5.2c) with a minimum width equal to 16 μm for $P = 80\ P_{cr}$. It is clearly evident in Fig. 5.2c that modulation instability has generated self focusing in the orthogonal direction as well. For $P > 100\ P_{cr}$, the beam breaks up into individual filaments (Fig. 5.2d-e). The filaments are seeded by small variations in the input beam and are stable in location and size to small variations in the input energy. In other words, the pattern of filaments is repeatable from shot to shot as long as the illuminating beam profile is kept constant. The diameter of the filaments is approximately 12 μm and does not change when the energy is increased, while the number of filaments increases with power. When $P > 250\ P_{cr}$, the output beam profile becomes unrepeatable and the filaments start to fuse into a continuous line (Fig 2f-h). We will explain the origin of this instability later on. Part of the energy is scattered out of the central maximum into side lobes. The mechanism responsible for the formation of the side lobes is the emission of conical waves [18,19] during the formation of the filaments. The diameter of the filaments initially decreases until it reaches a stable condition; at this point some of the energy is released through conical emission while the rest of the energy is trapped in the filament [20].

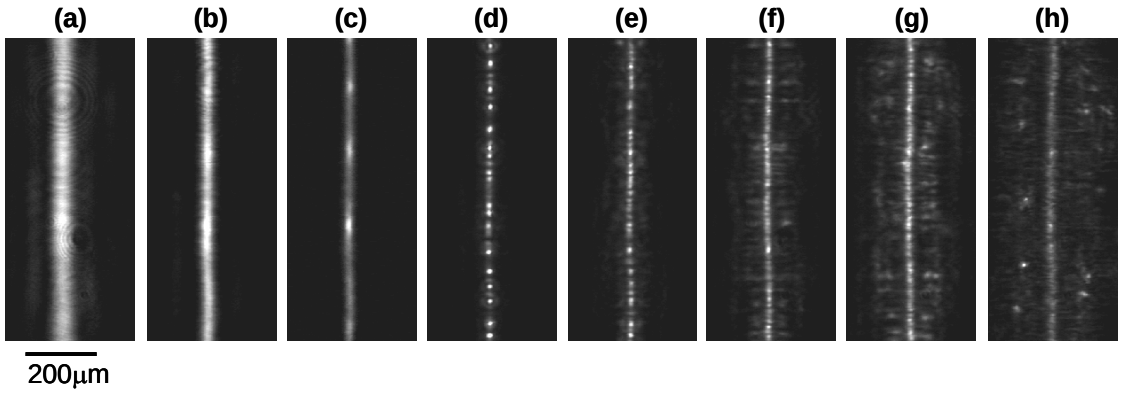

Figure 5.2. Beam profile of the pump pulse at the output of the CS_2 cell. The power increases from left to right: a) $P = 12P_{cr}$, b) $40P_{cr}$, c) $80P_{cr}$, d) $170P_{cr}$, e) $250P_{cr}$, f) $390P_{cr}$, g) $530P_{cr}$, h) $1200P_{cr}$. The size of each image is 0.36 mm (h) x 0.89 mm (v).

Video 5.1 and Video 5.2 show how the shot-to-shot fluctuations in the pulse energy affect the beam profile at the output of the cell. For each video, ten images were captured with the same experimental conditions and compiled into a movie clip, the only variable being the fluctuations in the laser pulse energy. For a pulse with a power of 170 P_{cr} the output beam profile is stable (Video 5.1). There are only small changes in the position of the filaments while the overall pattern of filaments remains constant. Filaments that appear close to each other seem to be the most sensitive to the energy fluctuations. If the power is increased to 390 P_{cr} the beam profile at the output becomes unrepeatable (Video 5.2). The position of the filaments varies greatly from shot to shot and the central line bends differently for each shot.

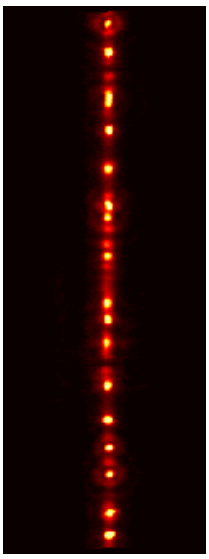

Video 5.1. Movie of changes in the beam profile as a result of fluctuations in the pulse energy for $P = 170\ P_{cr}$ (78.5 KB). The image area is 0.36 mm (h) x 0.89 mm (v).

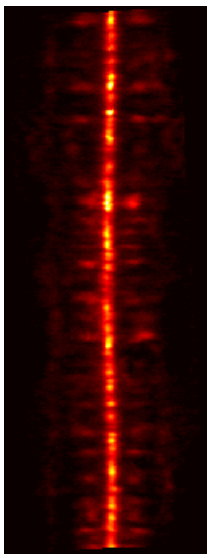

Video 5.2. Movie of changes in the beam profile as a result of fluctuations in the pulse energy for $P = 390\ P_{cr}$ (113 KB). The image area is 0.36 mm (h) x 0.89 mm (v).

Increasing the pulse energy causes the beam to self-focus faster and break up into filaments earlier. As shown above, further increasing the energy causes the beam to become unstable. For low energy levels the beam profile remains uniform, but as the energy is increased the beam breaks up into a periodic array of filaments. We have measured the beam profile at a fixed distance from the cell entrance for eight different pulse energies. The beam profile is captured using the FTOP setup with a fixed delay. Figure 5.3a shows a cross section of the beam profile at a distance of 2.5 mm inside the cell for pulse power of P = 250 P_{cr}, 390 P_{cr}, 530 P_{cr}, 790 P_{cr}, 1200 P_{cr}, 1700 P_{cr}, 2700 P_{cr}, 3800 P_{cr}. Higher power levels are necessary to observe filaments after a distance of 2.5 mm, as opposed to 10 mm in Figure 5.2. Figure 5.3b shows the Fourier transform of the beam cross sections in Figure 5.3a. The central peak (DC component) in the Fourier transform is blocked to visualize the secondary peaks. For P = 250 P_{cr}, no filaments are observed as the beam remains uniform after 2.5 mm. Note that for this power the beam completely breaks up into filaments after 10 mm (Fig. 5.2e). As the power is increased between 390 P_{cr} and 790 P_{cr} an increasing number of filaments appears in a periodic array. The periodicity is clearly visible in the Fourier transform; a peak appears that corresponds to the spacing between the filaments (~ 20 μm). The emergence of periodicity in the beam pattern is discussed in the following section. When the power is increased above 1200 P_{cr} the periodicity starts to disappear. The beam is no longer uniform but there is no clear indication of the formation of filaments. This state corresponds to the patterns in Figure 2f-h, where the beam profile becomes unstable.

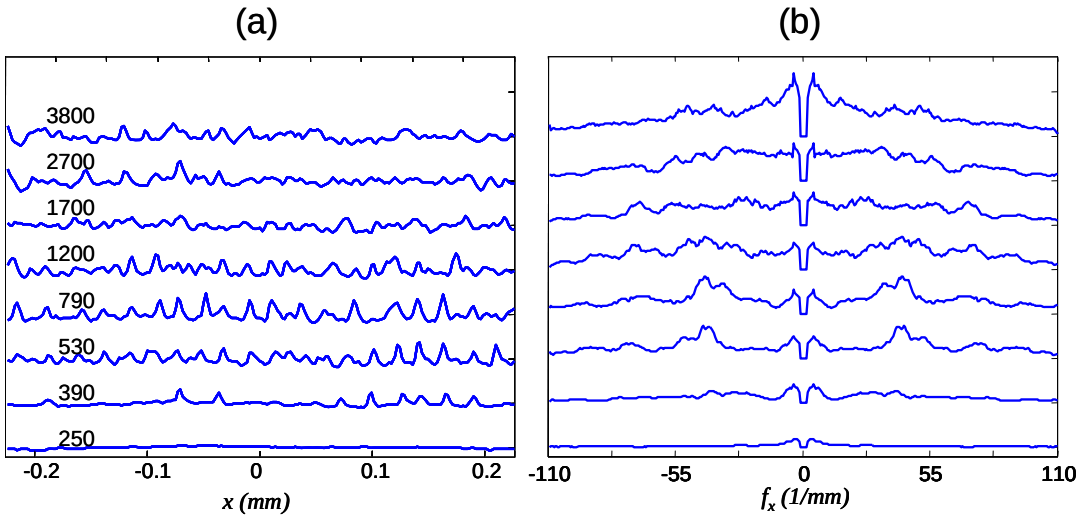

Figure 5.3. Beam profile inside the cell as a function of power. (a) Cross sections of the beam profile at 2.5 mm inside the cell for pulse power P/P_{cr} = 250, 390, 530, 790, 1200, 1700, 2700, 3800. The cross sectional plots for different powers are displaced vertically for visual clarity. The lowest power is displaced at the bottom. The peaks correspond to regions of higher intensity (filaments). (b) Fourier transform of the plots in (a). The peaks represent the periodicity of the arrays of filaments. A strong central peak (DC component) is zeroed to display the secondary peaks.

5.3.2. Spatial evolution of the beam and self-organization

Video 5.3 shows the filamentation process for a pulse with P = 390 P_{cr}. The pulse propagation inside the material is captured from 2 mm to 4 mm from the cell entrance using the FTOP setup. The width of the image of the pulse on the CCD camera (CCD 2 in Fig. 5.1) depends on the pulse duration and the time response of the material. CS_2 has both a very fast (femtosecond) electronic time response and a slower (picosecond) molecular response. In our experiments, the time response at the leading edge of the signal is essentially instantaneous, and the resolution is determined by the pulse duration (150

femtoseconds). On the trailing edge of the signal a slower decay time of approximately 1.5 picoseconds is observed, which is consistent with the time constant for the molecular response of the material. The movie clip in Video 3 shows the propagation of a pulse with a spatial profile that is initially uniform. The movie is compiled from multiple pump-probe experiments by varying the delay of the probe pulse. As the beam propagates the intensity modulation increases until the beam breaks up into filaments. The light is trapped in the filaments, which continue to propagate with a constant diameter for several millimeters.

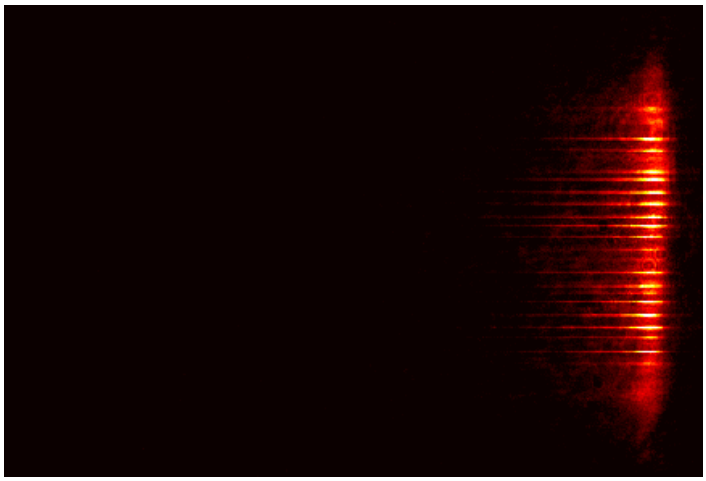

Video 5.3. Pulse propagation inside CS_2 from 2 mm to 4 mm from the cell entrance for a pulse power of 390 P_{cr}. An initially uniform beam breaks up into stable filaments (258 KB). The image size is 2.4 mm (h) x 1.6 mm (v).

Figure 5.4 shows the trajectory of the beam obtained in the FTOP setup for pulses with P = 390 P_{cr} (a) and 1200 P_{cr} (c), from a distance of 0.5 cm to 5 cm from the cell entrance. The trajectory is obtained by numerically combining multiple pump-probe images of the pulse at different positions as it traverses the material. The 1-D Fourier transforms of the beam profile are calculated and displayed in Figure 5.4b and 5.4d for each position along the propagation direction. The peaks in the Fourier transform correspond to the periodicity in the positions of the filaments. The central peak (DC component) in the Fourier transform is

blocked to improve the contrast in the image. Periodic changes in the amplitude of the peaks along the propagation direction are artifacts due to the sampling of the beam profile in the experiments.

The pulse with lower power (Fig. 5.4a) breaks up into filaments at a distance of 2.9 mm into the material, while the pulse with higher power (Fig. 5.4c) breaks up at 1.5 mm from the cell entrance. The Fourier transform in Fig. 4b clearly shows how a periodicity emerges during the filamentation process. The filaments are created in a regular array and propagate undisturbed for several millimetres. The spacing between the filaments is approximately 40 μm, about four times the diameter of the filaments. If the pulse energy is higher (Fig. 5.4d) the array of filaments initially forms with a higher spatial frequency. The period then increases from 22 μm to 33 μm as the filaments propagate. After 5 mm the sharp peaks visible in the Fourier transform start to fan out. The gradual loss of the periodicity after 5 mm corresponds to a decline in the number of filaments. We attribute the change in the period of the soliton array primarily to the interactions between nearby filaments. These interactions cause filament fusion and conical emission, redirecting some of the energy away from the main line of solitons. The filaments then continuously rearrange themselves in a sparser grid. The interactions depend on the relative phase of the filaments. Filaments of the same phase will attract while out-of-phase neighboring filaments will repel. The phase of individual filaments is determined by the initial condition (the illuminating beam) but also by the accumulated phase along the propagation path with linear and nonlinear contributions. Slight intensity or angle changes can lead to large accumulated phase differences. We believe that this effect is responsible for the onset of the chaotic behaviour we observe.

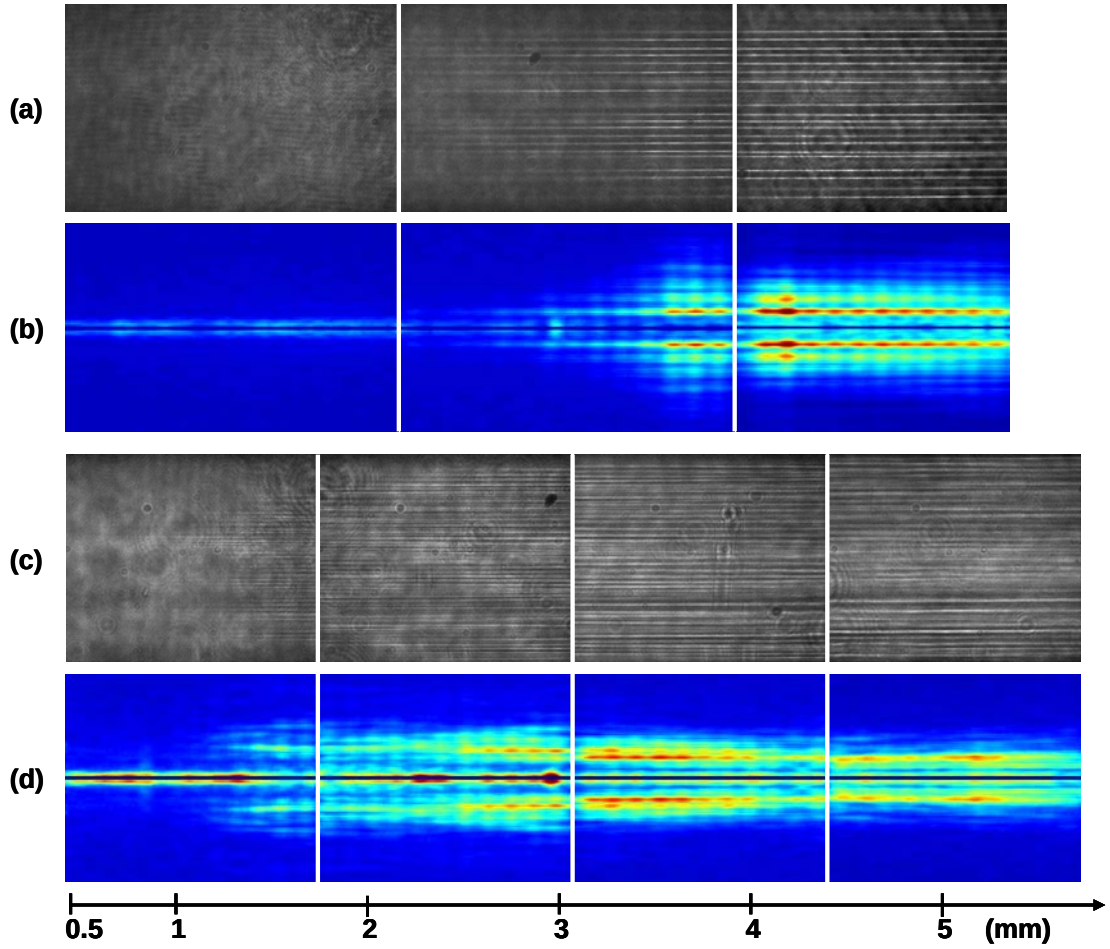

Figure 5.4. Pulse trajectories and 1-D Fourier transforms. (a,c) The trajectory of the pulse is reconstructed by digitally adding up the FTOP frames for different positions of the pulse. Each separate image corresponds to frames taken for a fixed position of CCD camera. The camera was moved laterally to capture the beam profile farther along inside the cell. The pulse power is $390P_{cr}$ in (a) and $1200P_{cr}$ in (c). (b,d) Show the 1-D Fourier transforms of the filamentation patterns in (a) and (c), respectively. The central component is blocked to visualize higher frequencies.

Figure 5.5 shows the cross sectional plots of the filament formation for the pulse with P = 390 P_{cr}. The figure shows the beam profile for 6 different positions inside the material during the filament formation phase. The propagation distance increases from bottom to top (the plots are separated for visual clarity) with an increment of 250 μm for each plot. The first cross section (Fig. 5.5a) shows a uniform beam profile, at a distance of 2.4 mm from the entrance of the cell. In the second there is some redistribution of the intensity into local maxima, with peaks of approximately 30 μm in diameter (Fig. 5.5b). The peaks continue to grow until they reach a diameter of about 10 μm and become stable. The whole process of filamentation happens in just over 1 mm of propagation (Fig. 5.5b-f).

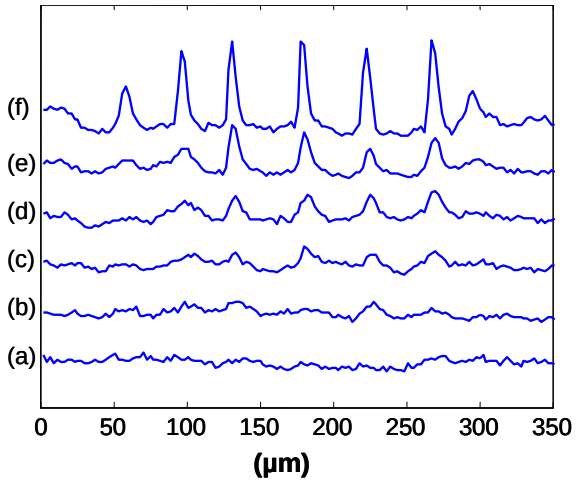

Figure 5.5. Cross sectional plots of filament formation for P = 390 P_{cr}. Each plot represents a fraction of the beam profile (0.35 mm) at a specific distance from the cell entrance: 2.40 mm (a), 2.65 mm (b), 2.90 mm (c), 3.15 mm (d), 3.40mm (e) and 3.65 mm (f).

Figure 5.6 shows a close-up of filament interactions from 3.5 mm to 4.2 mm inside the material for P = 1200 P_{cr}. Regions (a) and (c) show stable filaments that propagate through undisturbed. Region (b) of Fig. 5.6 shows two filaments merging. This interaction is similar to the attraction force experienced by solitons in close proximity. The filaments start out

separated by 20 μm, and only one filament is seen to survive after the interaction. Region (d) shows a filament that starts out with a small diameter and diverges. The filament size continues to increase until it overlaps with a neighbor, after which a single filament continues to propagate (not shown in the picture). In region (e) a new filament is formed well inside the material. It is not clear wether the new filament is generated by the background light or if it splits from an existing filament. As the pulse continues to propagate the number of filaments continues to decrease, until the output at 10 mm where we see almost a continuous line at the center with only a few distinguishable filaments (Fig. 5.2h).

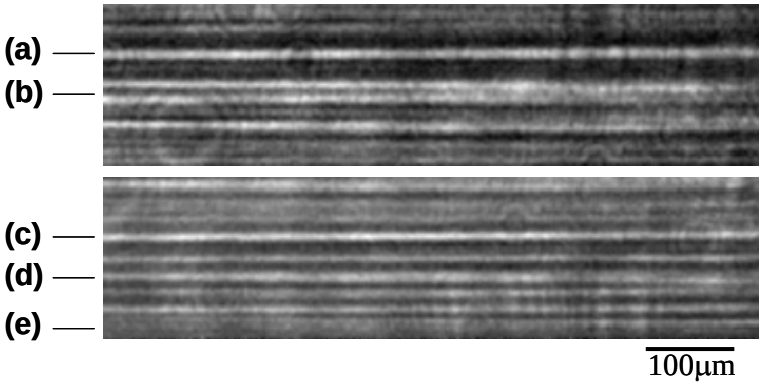

Figure 5.6. Interactions between filaments from 3.5 mm to 4.2 mm from the cell entrance for an input pulse power of 1200 P_{cr}. Some filaments propagate undisturbed (a-c). We have observed fusion of two filaments (b), divergence of a filament (d) and the generation of a new filament (e).

5.3.3. Periodic arrays of filaments

A stable array of filaments can be launched by modulating the input beam. If the separation between the filaments is large enough the filaments will not interact. Figure 5.7 shows the propagation of filaments generated by placing an amplitude grating (40μm period) before

the entrance of the cell. The input power is $P = 200\ P_{cr}$. Filaments form very quickly and propagate undisturbed (Fig. 5.7a). The 1-D Fourier transform in Fig. 5.7b shows that the period induced by the grating does not change with propagation. Figure 5.7c shows the array of filaments at the output face of the cell (10mm propagation). The propagation distance of the filaments in this case is limited by the cell length. The modulation of the beam amplitude speeds up the formation of the filaments, while the input energy ensures the stability. Most of the available energy is trapped in the filaments; no light was detected outside of the filaments. The energy in each filament can be estimated from the total energy and the number of filaments. Each filament carries approximately four times the critical power ($4\ P_{cr}$).

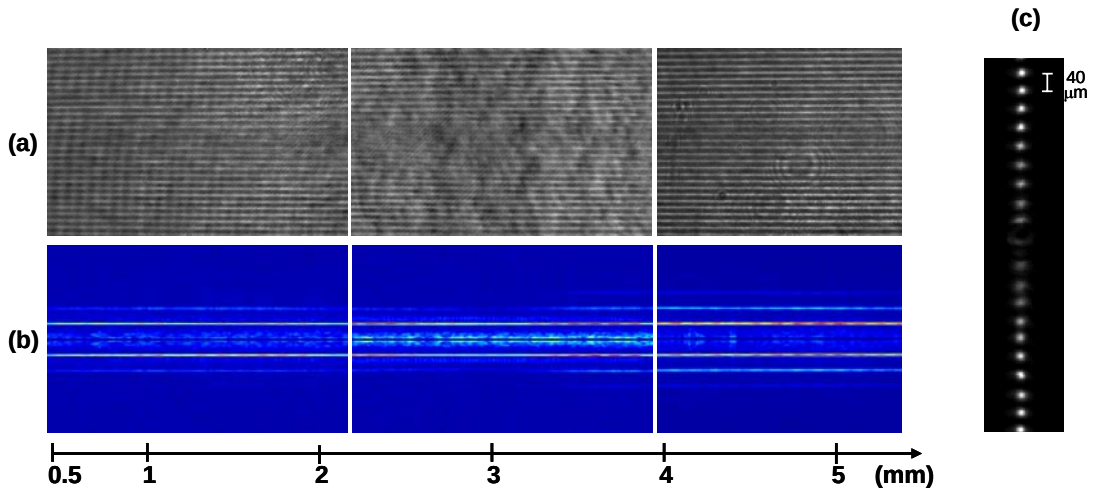

Figure 5.7. Propagation of a pulse with a periodic beam profile (a) The trajectory of the pulse is reconstructed by digitally adding up the FTOP frames for different positions of the pulse. (b) 1-D Fourier transforms of the filamentation patterns in (a). The central component is blocked to visualize higher frequencies. (c) Image of the beam profile at the output of the cell after 10 mm of nonlinear propagation.

We have also generated 2-D arrays of filaments. The cylindrical lens is removed from the setup for this experiment, so the input intensity is decreased. The input beam (5 mm

FWHM) is modulated using an amplitude mask at a distance of 10 cm from the cell. The mask is a chessboard pattern with a period of 128 μm. The diffraction pattern incident on the cell has a periodic modulation that seeds the formation of filaments in a periodic 2-D array. Figure 5.8 shows the beam at the output of the cell for different pulse energies. The pictures show only a fraction of the beam profile (0.96 mm x 1.28 mm). Figure 8a shows the beam profile for a low energy where the nonlinearities are weak. The periodic modulation is due to the mask. As the power is increased filaments start to form at the local maxima of the intensity profile. For the maximum power all of the local maxima self-focus into filaments, thus creating a 2-D array of filaments.

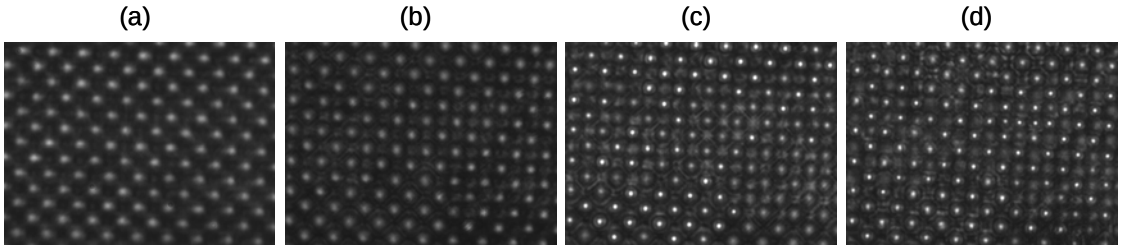

Figure 5.8. Formation of a 2-D array of filaments. More filaments appear as the pulse energy is increased: (a) 0.01 mJ, (b) 0.46 mJ, (c) 0.71 mJ, (d) 1.0 mJ. The area of each image is 1.28 mm x 0.96 mm.

5.4. NUMERICAL SIMULATIONS

The experimental results were verified using a numerical simulation. The propagation model is a time-averaged nonlinear Schrodinger equation that includes the effects of diffraction, third order nonlinearity (Kerr effect) and two-photon absorption [21]. A fifth order nonlinearity was also included to account for the stability of the filaments observed experimentally. The negative index change generated through the fifth order nonlinearity

balances the positive Kerr index change. A complete simulation of the spatial and temporal profile of the nonlinear pulse propagation requires very fine sampling in three spatial dimensions and time. We assume in our model that the temporal profile of the pulse is constant, which allows us to calculate the beam evolution with good spatial resolution. We have shown in Chapter 4 that this model provides a good approximation to the propagation of femtosecond pulses in CS_2. The light propagation is calculated assuming a scalar envelope for the electric field, which is slowly varying along the propagation direction *z*. The evolution of the scalar envelope is given by the equation:

$$\frac{dA}{dz} = \frac{i}{2kn_0}\left(\frac{\partial^2}{\partial x^2} + \frac{\partial^2}{\partial y^2}\right)A + ik\left(n_2|A|^2\right)A - ik\left(n_4|A|^4\right)A - \beta|A|^2 A \qquad (5.2)$$

$A(x,y,z,T)$ is the complex envelope of the electric field, $k = \frac{2\pi}{\lambda}$, λ = 800nm, n_0 = 1.6, n_2 = $3\text{x}10^{-15}\text{cm}^2/\text{W}$ [16], n_4 = $-2\text{x}10^{-27}\text{cm}^4/\text{W}^2$, β = $4.5\text{x}10^{-13}$ cm/W [21]. The first term on the right-hand side accounts for diffraction, the second is Kerr self-focusing (third-order nonlinearity), the third term accounts for the fifth-order nonlinearity and the last term represents for two-photon absorption. Linear absorption is negligible at the wavelength used in the experiments. The equation is solved numerically using the Split-step Fourier method.

The two-photon absorption term affects the propagation only for the highest intensity levels and does not significantly change the qualitative behaviour observed in the simulations. The fifth-order nolinearity (n_4) is the mechanism responsible for the generation of stable light filaments. Since we could not find experimentally measured values of n_4, in the simulation we have assigned it the value that gave the best match with the experimental results. The stabilization of the filaments can also be caused by a negative index change due to the plasma generation. If the light intensity is high enough a plasma can be created through multiphoton absorption. However, the intensity of the filaments is well below the threshold for plasma generation [20]; therefore multiphoton ionization does not play a significant role in the filament dynamics and does not need to be included in the simulations.

The input beam for the simulation is generated using the image of the beam in Fig. 5.2a. The square root of the measured intensity profile is used as the amplitude of the input light field, and a phase profile is added to simulate the phase of the focused beam at the entrance of the cell. The simulated field is a good approximation to the experimental input beam and has a similar noise profile.

The model in equation 5.2 was used to numerically calculate the output beam profile after propagating through 10 mm of CS_2. Figure 5.9 shows a comparison of the numerical and experimental results. The simulation follows the experimental results very closely during the self-focusing stage (Fig. 5.9a-c). The beam self-focuses into a line of decreasing width as the power is increased. There is also good agreement between simulation and experiment when the beam breaks up into filaments (Fig. 5.9d-e). The number of filaments is similar, and in both cases the filaments release some energy through conical emissions. The difference in the spacing of the filaments is discussed below. Up to this point the behaviour observed in the simulation is very similar to the experiments; however, the simulation does not capture the behaviour of the beam in the chaotic stage (Fig. 5.9f-h). In the experiments some energy is lost and the filaments disappear. A central bright line remains and is surrounded by side-lobes that propagate away from the center. For the highest power level new filaments appear in the side-lobes. The simulation shows different behaviour, as more filaments appear in the central line and then start moving away. In the numerical results the array becomes unstable as the density of the filaments increases and some of the filaments get deflected through their mutual interactions; however, only some of the filaments disappear while a lot of them survive. In fact, in the simulations most of the energy is trapped in the filaments, even for the highest power levels.

The loss seems to be a key element in the discrepancy between experiment and simulation. The only source of loss in the simulation is two-photon absorption, which does not dissipate enough energy when compared to the experiment. It is not clear what causes the energy loss in the experiments. Another source of error is in the temporal domain that is neglected in the simulations. The spectral content of the solitons increases as they propagate, which is ignored in the simulation. It is possible that the energy that is

transformed to higher frequencies is no longer trapped in the soliton. A full 3-D simulation might help in resolving some of these issues.

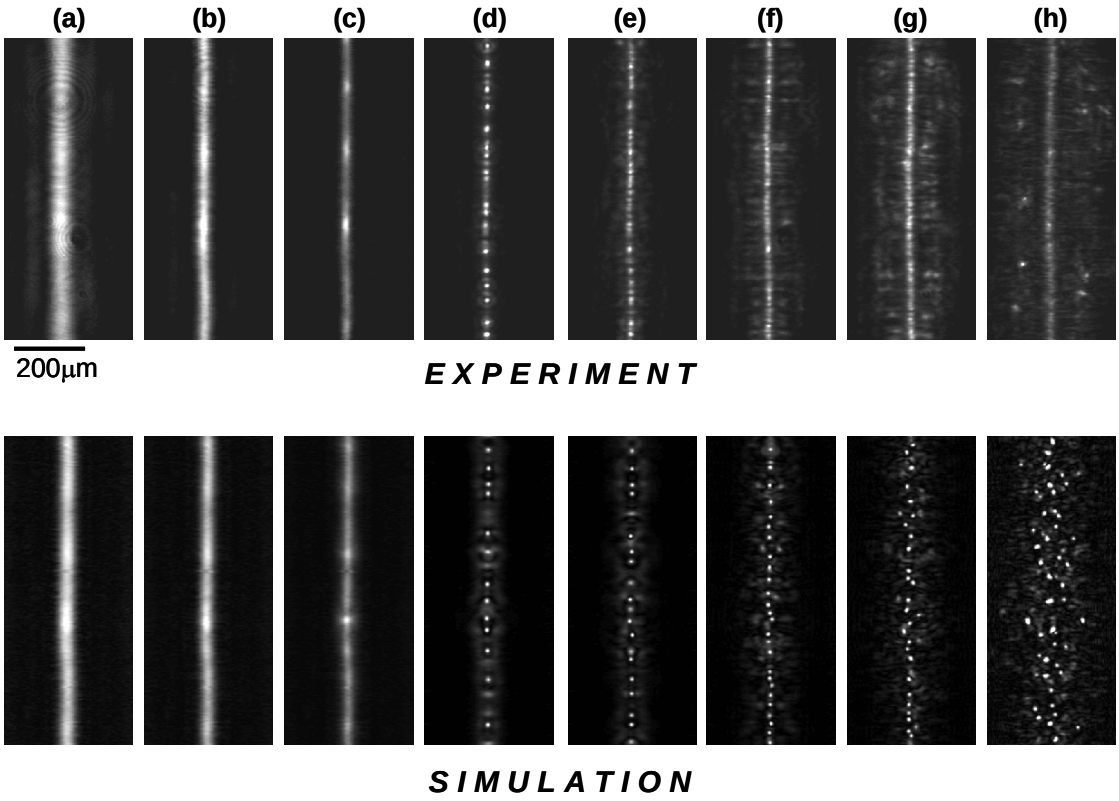

Figure 5.9. Comparison of experimental and numerical results of beam profile as a function of pulse energy. The power increases form left to righ: a) P = 12 P_{cr}, b) 40 P_{cr}, c) 80 P_{cr}, d) 170 P_{cr}, e) 250 P_{cr}, f) 390 P_{cr}, g) 530 P_{cr}, h) 1200 P_{cr}.

The beam profile as viewed from the side was also calculated for a propagation distance of 10 mm. Figure 10 shows the 1-D Fourier transforms of the beam profile for four different power levels, 250 P_{cr}, 390 P_{cr}, 530 P_{cr} and 1200 P_{cr}. In Fig. 5.10a we can clearly see that after a propagation distance of 6 mm the filaments form a periodic array (with a period of approximately 30 μm), which remains constant for several millimeters and starts to break down only towards the end of the cell. Fig. 5.10b shows a periodic arrangement that starts

with a slightly smaller period before settling to a period of 30 μm. For the input power in Fig. 5.10c the filaments initially form with a period of 16 μm after a propagation distance of 3 mm. As the light propagates to a distance of 6 mm the period increases to 25 μm, and after this point the period seems to continue to increase but the peaks in the Fourier transform start to fan out as the array of filament loses its periodicity. For the highest energy level (Fig. 5.10d) multiple peaks appear in the Fourier transform, with a trend towards smaller spatial frequencies with increasing propagation distance. At this level no clear periodicity is observed in the simulations. The behavior observed in the simulations is very similar to that of the experimental results. In both cases order (periodicity) emerges, evolves and eventually dissipates. In the simulations the filaments form with a smaller period and the filamentation distance is longer. We attribute these differences to the lack of knowledge of the exact initial conditions (beam intensity and phase), approximations made in the numerical model and uncertainties in the constants used for the simulation.

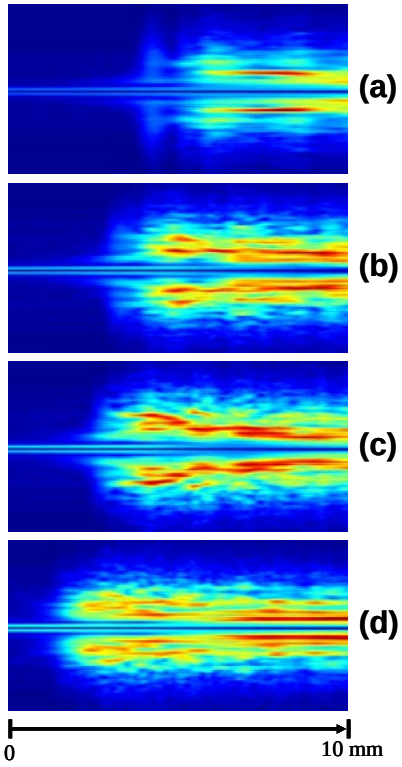

Figure 5.10. 1-D Fourier transforms for numerically calculated beam propagation. The beam propagation is numerically calculated for four different power levels a) P =

250 Pcr, b) 390 Pcr, c) 530 Pcr, d) 1200 Pcr. A 1-D Fourier transform on the side view of the beam profile is calculated for each along the propagation direction. The total distance is 10 mm. The central peak (DC component) in the Fourier transform is blocked to improve the contrast in the image.

5.5. SUMMARY

We have observed the emergence of order, self organization and a transition to a chaotic state in an optical self-focusing nonlinear medium. Order emerges through the formation of spatial solitons in a periodic array. If the initial period of the array is unstable the solitons will tend to self-organize into a larger (more stable) period. These results provide new insight into the collective behaviour of solitons in nonlinear systems and will impact potential applications using arrays of solitons for computation or communications. A time-averaged nonlinear Schrodinger equation was used to model the propagation numerically. The numerical simulations were in good agreement with the experiments and captured the formation of filaments and self-organization, but did not reproduce the beam instabilities for the highest power levels observed experimentally.

REFERENCES

[1] M. Saffman, G. McCarthy, W. Krolikowski, J. Opt. B. **6**, 387-403 (2004).

[2] D. Kip, M. Soljacic, M. Segev, E. Eugenieva, D. N. Christodoulides, Science **290**, 495-498 (2000).

[3] G. I. Stegeman, M. Segev, Science **286**, 1518-1523 (1999).

[4] A. Barthelemy, S. Maneuf, C. Froehly, Opt. Comm. **55**, 201-206 (1985).

[5] M. Segev, B. Crosignani, A. Yariv and B. Fischer, Phys. Rev. Lett. **68,** 923-926 (1992).

[6] W. E. Torruelas, Z. Wang, D. J. Hagan, E. W. Vanstryland, G. I. Stegeman, L. Torner, C. R. Menyuk, Phys. Rev. Lett. **74**, 5036-5039 (1995).

[7] A. J. Campillo, S. L. Shapiro, and B. R. Suydam, Appl. Phys. Lett. **23**, 628-630 (1973).

[8] J. P. Gordon, Opt. Lett. **8**, 596-598 (1983).

[9] M. Shalaby, F. Reynaud, and A. Barthelemy, Opt. Lett. **17**, 778-780 (1992).

[10]. R. Mcleod, K. Wagner, and S. Blair, Phys. Rev. A **52**, 3254-3278 (1995).

[11] M. Peccianti, C. Conti, G. Assanto, A. De Luca, C. Umeton, Nature **432**, 733 (2004).

[12] M. Mlejnek, M. Kolesik, J. V. Moloney, and E. M. Wright, Phys. Rev. Lett. **83**, 2938-2941 (1999).

[13] L. Berge, S. Skupin, F. Lederer, G. Mejean, J. Yu, J. Kasparian, E. Salmon, J. P. Wolf, M. Rodriguez, L. Woste, R. Bourayou, R. Sauerbrey, Phys. Rev. Lett. **92**, 225002 (2004).

[14] H. Schroeder and S. L. Chin, Opt. Comm. **234**, 399-406 (2004).

[15] R Boyd, *Nonlinear Optics*, Academic Press, 2003.

[16] R. A. Ganeev, A. I. Ryasnyansky, M. Baba, M. Suzuki, N. Ishizawa, M. Turu, S. Sakakibara, H. Kuroda, Appl. Phys. B **78**, 433-438 (2004).

[17] M. Fujimoto, S. Aoshima, M. Hosoda, and Y. Tsuchiya, Opt. Lett. **24**, 850-852 (1999).

[18] G. G. Luther, A. C. Newell, and J. V. Moloney, E. M. Wright, Opt. Lett. **19**, 789-791 (1994).

[19] E. T. J. Nibbering, P. F. Curley, G. Grillon, B. S. Prade, M. A. Franco, F. Salin, and A. Mysyrowicz, Opt. Lett. **21**, 62-64 (1996).

[20] M. Centurion, Y. Pu, M. Tsang, D. Psaltis, submitted to Phys. Rev. A (2005).

[21] M. Falconieri, G. Salvetti, Appl. Phys. B. **69**, 133-136 (1999).

Appendix A

DERIVATION OF THE NONLINEAR SCHRODINGER EQUATION FOR PULSE PROPAGATION

Here we show the derivation of the nonlinear Schrodinger equation (NLSE) for pulse propagation through nonlinear media. We start from Maxwell's equations and separate the linear and nonlinear response of the material. The approach is similar to that used by Agrawal [1] and Boyd [2]. We assume an isotropic medium and no free charges (no plasma). If there is plasma generation, additional terms can be added to the NLSE to account for multiphoton absorption (which leads to ionization) and the plasma index change. In the case we are most interested in, pulse propagation in CS_2, we did not observe ionization so the main contributions are from the third- and fifth-order nonlinear terms in the polarization.

We start from Maxwell's equations in Gaussian units, assuming no free charges:

$$\nabla \bullet \vec{D} = 0 . \qquad \text{A.1}$$

$$\nabla \bullet \vec{B} = 0 . \qquad \text{A.2}$$

$$\nabla \times \vec{E} = \frac{-1}{c}\frac{\partial \vec{B}}{\partial t} . \qquad \text{A.3}$$

$$\nabla \times \vec{H} = \frac{1}{c}\frac{\partial \vec{D}}{\partial t} \qquad \text{.A.4}$$

Where *D, B, E, H* are vectors that depend on 3 spatial coordinates and time. The spatial and time dependence of the vector fields is not shown explicitly in order to simplify the notation.

We separate *D* into a linear and a nonlinear part:

$$\vec{D} = \varepsilon\vec{E} + \vec{P}^{NL}, \qquad \text{A.5}$$

where the second term contains the nonlinear polarization of the material and the first term accounts for the linear response:

$$\varepsilon = 1 + 4\pi\chi^{(1)}. \qquad \text{A.6}$$

The nonlinear polarization accounts for all higher order effects, frequency generation, nonlinear absorption, nonlinear index changes, etc. We now proceed to derive the wave equation in the usual way, taking the curl of A.3:

$$\nabla \times \nabla \times \vec{E} = \frac{-1}{c^2}\frac{\partial^2 \vec{D}}{\partial t^2}. \qquad \text{A.7}$$

We can simplify the expression by taking advantage of the fact that we are assuming no free charges, so the divergence of *E* vanishes:

$$\nabla \times \nabla \times \vec{E} = \nabla\left(\nabla \bullet \vec{E}\right) - \nabla^2\vec{E} = -\nabla^2\vec{E}. \qquad \text{A.8}$$

We can now re-write A.7 using A.8 and A.5:

$$-\nabla^2\vec{E} + \frac{\varepsilon}{c^2}\frac{\partial^2\vec{E}}{\partial t^2} = \frac{-1}{c^2}\frac{\partial^2\vec{P}^{NL}}{\partial t^2}. \qquad \text{A.9}$$

This is the nonlinear wave equation in the time domain. We assume that the polarization does not change during the propagation, so scalars can be used instead of vectors. The coupling between orthogonal polarization states is in general very small and can be neglected. We apply the scalar field approximation and Fourier-transform the variables to the frequency domain:

$$D(t) = \frac{1}{2\pi}\int D(\omega)e^{-i\omega t}d\omega, \qquad \text{A.10}$$

$$P(t) = \frac{1}{2\pi}\int P(\omega)e^{-i\omega t}d\omega, \qquad \text{A.11}$$

$$D(\omega) = \varepsilon(\omega)E(\omega) + P^{NL}(\omega). \qquad \text{A.12}$$

The transformation is only in time; the spatial dependence of the fields is implicit. We can now re-write the wave equation A.9 in frequency domain:

$$-\nabla^2 E(\omega) + \varepsilon(\omega)\frac{\omega^2}{c^2}E(\omega) = \frac{-\omega^2}{c^2}P^{NL}(\omega). \qquad \text{A.13}$$

If the laser pulse contains many optical cycles, we can rewrite the electric field *E* as the product of a complex envelope *A* and a carrier wave:

$$E(t) = A(t)\exp[i(k_0 z - \omega_0 t)]. \qquad \text{A.14}$$

Here we have assumed a pulse propagating in the *z* direction. ω_0 is the center frequency in the spectrum of the pulse, and $k_0 = \sqrt{\varepsilon(\omega_0)}\frac{\omega_0}{c} = n_0\frac{\omega_0}{c}$. Both ω_0 and k_0 are constants. The Fourier transform of A.14 is:

$$E(\omega) = A(\omega - \omega_0)\exp[ik_0 z] = \tilde{A}\exp[ik_0 z]. \qquad \text{A.15}$$

We can now use A.15 to re-write the wave equation A.13 in terms of the complex envelope *A*:

$$\nabla_T^2\tilde{A} + \frac{\partial^2\tilde{A}}{\partial z^2} + 2ik_0\frac{\partial\tilde{A}}{\partial z} + [k^2 - k_0^2]\tilde{A} = \frac{-\omega^2}{c^2}P^{NL}(\omega)\exp[-ik_0 z], \qquad \text{A.16}$$

where $\nabla_T^2 = \frac{\partial^2}{\partial x^2} + \frac{\partial^2}{\partial y^2}$ and k is a function of ω such that $k^2 = \varepsilon(\omega)\frac{\omega^2}{c^2}$. We have separated the transverse derivatives and the derivatives along the direction of propagation (*z*). The extra terms on the left-hand side come from applying the chain rule when taking the derivative in *z*. We now apply the slowly varying envelope approximation (SVEA):

$$\frac{\partial^2 \tilde{A}}{\partial z^2} << 2ik_0 \frac{\partial \tilde{A}}{\partial z}. \qquad \text{A.17}$$

This approximation means that the complex envelope does not change very rapidly in z, i.e. the derivative of the complex envelope is smooth on a scale comparable to the wavelength. This approximation breaks down for very short pulses (few optical cycles) or very strong nonlinearities. For most cases, however, using this approximation does not significantly affect the simulation results. If we drop the second order derivative we are left with:

$$\nabla_T^2 \tilde{A} + 2ik_0 \frac{\partial \tilde{A}}{\partial z} + \left[k^2 - k_0^2\right]\tilde{A} = \frac{-\omega^2}{c^2} P^{NL}(\omega)\exp\left[-ik_0 z\right]. \qquad \text{A.18}$$

In practice, k is usually very close to k_0, so the following approximation applies:

$$k^2 - k_0^2 = 2k_0(k - k_0), \qquad \text{A.19}$$

and we can re-write A.18 as:

$$\begin{aligned} &\nabla_T^2 \tilde{A} + 2ik_0 \frac{\partial \tilde{A}}{\partial z} + 2k_0(k - k_0)\tilde{A} + \frac{\omega^2}{c^2} P^{NL}(\omega)\exp\left[-ik_0 z\right] = 0 \\ &= \frac{\partial \tilde{A}}{\partial z} - i(k - k_0)\tilde{A} + \frac{1}{2ik_0}\left(\nabla_T^2 \tilde{A} + \frac{\omega^2}{c^2} P^{NL}(\omega)\exp\left[-ik_0 z\right]\right) \end{aligned} \qquad .\text{A.20}$$

Now we Taylor expand k around k_0:

$$k = k_0 + k_1(\omega - \omega_0) + \frac{1}{2}k_2(\omega - \omega_0)^2, \qquad \text{A.21}$$

where the new variables are:

$$k_1 = \left(\frac{dk}{d\omega}\right)_{\omega=\omega_0} = \frac{1}{v_g}, \qquad \text{A.22}$$

$$k_2 = \left(\frac{d^2k}{d\omega^2}\right)_{\omega=\omega_0} = \left(\frac{-1}{v_g^2}\frac{dv_g}{d\omega}\right)_{\omega=\omega_0}, \qquad \text{A.23}$$

where v_g is the group velocity of the pulse in the material. k_1 is the inverse of the group velocity, and k_2 is a measure of the group velocity dispersion. Higher order dispersion can be included by adding the subsequent terms in the Taylor expansion in A.21. We now use A.19-23 to re-write A.18:

$$\begin{aligned}&\frac{\partial\tilde{A}}{\partial z} - i\left(k_1(\omega-\omega_0) + \frac{1}{2}k_2(\omega-\omega_0)^2\right)\tilde{A} \\ &= \frac{-1}{2ik_0}\left(\nabla_T^2\tilde{A} + \frac{\omega^2}{c^2}P^{NL}(\omega)\exp[-ik_0z]\right)\end{aligned}. \qquad \text{A.24}$$

This equation is now Fourier transformed back to the time domain using $(\omega\text{-}\omega_0)$ as the frequency variable:

$$\frac{\partial A}{\partial z} + k_1\frac{\partial A}{\partial t} + i\frac{k_2}{2}\frac{\partial^2 A}{\partial t^2} = \frac{-1}{2ik_0}\left(\nabla_T^2 A + \frac{1}{c^2}\frac{\partial^2 P^{NL}}{\partial t^2}\exp[-i(k_0z-\omega_0t)]\right). \qquad \text{A.25}$$

We can simplify the result by applying the envelope approximation also to the nonlinear polarization term:

$$P^{NL}(t) = 2\overline{P}^{NL}(t)\exp\left[i(k_0z - \omega_0t)\right], \qquad \text{A.26}$$

and the time derivative becomes:

$$\frac{\partial^2 P^{NL}}{\partial t^2} = -2\omega_0^2\left[\left(1+\frac{i}{\omega_0}\frac{\partial}{\partial t}\right)^2\overline{P}^{NL}\right]\exp[i(k_0z-\omega_0t)], \qquad \text{A.27}$$

which leads to:

$$\frac{\partial A}{\partial z} + k_1\frac{\partial A}{\partial t} = -i\frac{k_2}{2}\frac{\partial^2 A}{\partial t^2} + \frac{i}{2k_0}\nabla_T^2 A + i\frac{k_0}{n_0}\left(1+\frac{i}{\omega_0}\frac{\partial}{\partial t}\right)^2\overline{P}^{NL}. \qquad \text{A.28}$$

This equation can be further simplified by doing a coordinate transformation to a reference frame moving at the group velocity of the pulse:

$$u = t - \frac{z}{v_g} = t - k_1 z\,, \tag{A.29}$$

and $\overline{A}(u) = A(t)$. (A.30)

The derivatives can be replaced as follows:

$$\frac{\partial A}{\partial z} = \frac{\partial \overline{A}}{\partial z} - k_1 \frac{\partial \overline{A}}{\partial u}\,, \tag{A.31}$$

$$\frac{\partial A}{\partial t} = \frac{\partial \overline{A}}{\partial u}\,, \tag{A.32}$$

which leads to

$$\frac{\partial \overline{A}}{\partial z} = -i\frac{k_2}{2}\frac{\partial^2 \overline{A}}{\partial u^2} + \frac{i}{2k_0}\nabla_T^2 \overline{A} + i\frac{k_0}{n_0}\left(1 + \frac{i}{\omega_0}\frac{\partial}{\partial u}\right)^2 \overline{P}^{NL}\,. \tag{A.33}$$

This equation describes the propagation of a pulse through a nonlinear dispersive material. The first term on the right-hand side accounts for group velocity dispersion, the second term is diffraction and the last term includes the nonlinear effects. The differential operator accounts for self steepening, which can cause the temporal profile of the pulse to develop a sharp temporal profile.

If we assume that the temporal profile of the envelope of the nonlinear polarization varies much slower than the optical frequency, the differential operator can be ignored and we can use the approximation for the nonlinear polarization:

$$\frac{\partial^2 P^{NL}}{\partial t^2} \approx -2\omega_0^2 \overline{P}^{NL} \exp\left[i(k_0 z - \omega_0 t)\right]. \tag{A.34}$$

The simplified propagation equation is then:

$$\frac{\partial \overline{A}}{\partial z} = -i\frac{k_2}{2}\frac{\partial^2 \overline{A}}{\partial u^2} + \frac{i}{2k_0}\nabla_T^2 \overline{A} + i\frac{k_0}{n_0}\overline{P}^{NL}. \qquad \text{A.35}$$

Which terms are included in the nonlinear polarization will depend on the parameters of the pulse and material properties. For example, for CS_2 we have included the third- and fifth-order nonlinearities:

$$P^{NL} = \chi^{(3)}\left|E\right|^2 E + \chi^{(5)}\left|E\right|^4 E, \qquad \text{A.36}$$

or in terms of the envelop of the field we can write

$$\overline{P}^{NL} = n_2\left|\overline{A}\right|^2 \overline{A} + n_4\left|\overline{A}\right|^4 \overline{A}, \qquad \text{A.37}$$

where n_2 is the Kerr coefficient and n_4 is the coefficient for the fifth-order nonlinearity.

Including the nonlinear polarization terms in the propagation equation A.35 we get:

$$\frac{\partial \overline{A}}{\partial z} = -i\frac{k_2}{2}\frac{\partial^2 \overline{A}}{\partial u^2} + \frac{i}{2k_0}\nabla_T^2 \overline{A} + i\frac{k_0}{n_0}\left(n_2\left|\overline{A}\right|^2 + n_4\left|\overline{A}\right|^4\right)\overline{A}. \qquad \text{A.38}$$

This equation includes the effects of dispersion, diffraction and third- and fifth-order nonlinearities. If n_2 is positive and n_4 is negative this equation can lead to the formation of optical solitons. A simplified time-averaged equation can be derived by assuming that the temporal profile of the pulse does not change, i.e., the dispersion and any changes of the temporal profile due to the nonlinearities are ignorable. The time-averaged equation can be solved with considerably fewer computational resources. For this approximation we use a field A_s, which depends only on spatial coordinates and does not have a time dependence. The simplified propagation equation is:

$$\frac{\partial A_s}{\partial z} = \frac{i}{2k_0}\nabla_T^2 A_s + ik_0\left(n_2\left|A_s\right|^2 + n_4\left|A_s\right|^4\right)A_s. \qquad \text{A.39}$$

This equation accounts for the effects of diffraction and the effects of third- and fifth-order nonlinearities on the spatial profile of the beam. The disadvantage of using this equation is that the temporal-spectral information is lost. The advantage is that it reduces the dimensionality of the equation and allows one to calculate the beam evolution with high spatial resolution.

REFERENCES

[1] G. P. Agrawal, *Nonlinear fiber optics* (Academic Press, San Diego, 1995).

[2] R. Boyd, Nonlinear optics (Academic Press, San Diego, 2003).